2013-04-30

A Hybrid Multi-Objective Evolutionary Algorithm for Wind-Turbine Blade Optimization

Sessarego, Matias

UNIVERSITY OF CALGARY

A Hybrid Multi-Objective Evolutionary Algorithm for Wind-Turbine Blade Optimization

by

Matias Sessarego

A THESIS

SUBMITTED TO THE FACULTY OF GRADUATE STUDIES

IN PARTIAL FULFILLMENT OF THE REQUIREMENTS FOR THE

DEGREE OF MASTER OF SCIENCE

DEPARTMENT OF MECHANICAL AND MANUFACTURING ENGINEERING

CALGARY, ALBERTA

APRIL, 2013

Abstract

A concurrent-hybrid non-dominated sorting genetic algorithm II (hybrid NSGA-II) has been developed and applied to the simultaneous optimization of the annual energy production, flapwise root-bending moment and mass of the National Renewable Energy Laboratory's (NREL) 5 MW wind-turbine blade. To estimate the aerodynamic and structural performance, blade element momentum (BEM) and beam models were developed and validated. By hybridizing a multi-objective evolutionary algorithm (MOEA) with gradient-based local search, it is believed that the optimal set of blade designs could be achieved at lower computational cost than for a conventional MOEA. To compare the rate of convergence between the hybrid and non-hybrid NSGA-II on the NREL 5 MW blade optimization, a computationally intensive case requiring 110,000 objective-function evaluations was performed using the non-hybrid NSGA-II. From this particular case, a 1.8% increase in the annual energy production and 4.7% decrease in the flapwise root-bending moment with the same mass as the NREL 5 MW blade was achieved. The inclusion of local gradients in the blade optimization, however, shows no improvement in the convergence for this three-objective problem. A study on the gradient quality shows that the numerical instability of BEM and beam models hinders suitable gradient calculations.

Preface

This thesis is an extended version of a multi-authored work that has been submitted for publication to the journal of *Wind Energy*, John Wiley & Sons, Ltd. Its full citation reads:

Sessarego M, Dixon KR, Rival DE, Wood DH. A hybrid multi-objective evolutionary algorithm for wind-turbine blade optimization. *Wind Energy*; (under review).

The code development for the aerodynamic and structural models, and optimization algorithm, as well as the writing involved in the preparation of the journal article was performed by the author of the current thesis. The secondary authors advised the primary author throughout the code development, and edited the journal article prior to its submission.

This thesis also includes work that was presented at the International Symposium on Materials for Wind Energy Applications: Development, Modelling and Future Directions in Beijing, China on September 17, 2012. The presentation was prepared and given by the author of the current thesis. The presentation title reads:

"Multi-objective optimization of large wind turbine blades."

Acknowledgements

The successful completion of this thesis project has been facilitated by my two academic supervisors Drs. David Rival and David Wood as well as my industrial supervisor Mr. Kristian Dixon. All three have given me support and advice from the beginning to the end. I would like to thank Drs. Rival and Wood for helping me with scholarship applications, teaching me the fundamentals of wind-turbine aerodynamics, and the general guidance throughout my Master's.

I would like to thank Kristian Dixon and Kevin Standish for providing me the opportunity to work on my thesis project at the Siemens Wind R&D office in Boulder, Colorado, USA and the chance to visit the National Wind Technology Center located nearby. The experience that I have gained from meeting professionals who actively design Siemens wind-turbine blades is invaluable.

This project was funded by the Natural Sciences and Engineering Research Council of Canada's Industrial Postgraduate Scholarship (NSERC-IPS) program. For this reason, I gratefully acknowledge NSERC and Siemens Energy Inc. for their financial contributions.

Dedication

I dedicate this thesis to my family for all their love and support.

Table of Contents

Abstract . . . i
Preface . . . ii
Acknowledgements . . . iii
Dedication . . . iv
Table of Contents . . . v
List of Tables . . . vii
List of Figures . . . viii
List of Symbols . . . xii
1 **INTRODUCTION** . . . 1
1.1 Need for Wind Energy . . . 1
1.2 Wind Turbine Types . . . 3
1.3 Power from the Wind . . . 4
1.4 Scope of Thesis . . . 6
2 **LITERATURE REVIEW** . . . 8
2.1 Introduction . . . 8
2.2 Objective Space: Exploitation versus Exploration . . . 9
2.3 Gradient-Based Methods . . . 10
2.4 Evolutionary Algorithms . . . 13
2.4.1 Genetic Algorithm . . . 14
2.4.2 Evolution Strategies . . . 17
2.4.3 Differential Evolution . . . 19
2.5 Other Non-Gradient Based Methods . . . 19
2.5.1 Particle Swarm Optimization . . . 19
2.5.2 Complex Method . . . 20
2.6 Hybrid Evolutionary and Memetic Algorithms . . . 21
2.7 Summary . . . 22
3 **AERODYNAMIC MODEL** . . . 24
3.1 Introduction . . . 24
3.2 Actuator Disk Concept . . . 25
3.3 Blade Element Momentum Method . . . 28
3.3.1 Blade Element Theory . . . 28
3.3.2 Momentum Theory . . . 32
3.3.2.1 Tip-Loss Factor . . . 33
3.3.2.2 High-Thrust Correction . . . 35
3.3.3 BEM Algorithm . . . 35
3.4 Control and Regulation Strategy . . . 38
3.4.1 Pitch Regulation . . . 39
3.4.2 Variable Speed . . . 40
3.4.3 Pitch-Regulated and Variable-Speed HAWT Control Regions . . . 42
3.5 Verification and Experimental Validation . . . 43
3.5.1 Verification with WT_Perf . . . 43
3.5.2 Validation with NREL UAE Measurements . . . 47

3.5.2.1 Three-Dimensional and Rotational Effects . . . 47
3.5.2.2 NREL UAE Measurements . . . 50
4 **STRUCTURAL MODEL** . . . 53
4.1 Introduction . . . 53
4.2 Cross-Sectional Model . . . 55
4.2.1 Cross-Sectional Layup . . . 55
4.2.2 Laminate Coordinates Calculation . . . 57
4.2.3 Green's Theorem . . . 57
4.2.4 Calculation of Cross-Sectional Properties . . . 58
4.2.5 Verification with Analytical Model . . . 61
4.2.6 Verification for Realistic Blade Cross-Section . . . 67
4.3 Beam Model . . . 71
4.3.1 Bending Moments and Deflections . . . 71
4.3.2 Verification of Bending Moment and Deflection Calculations . . . 74
4.4 Structural Optimization and Constraints . . . 76
5 **HYBRID MULTI-OBJECTIVE EVOLUTIONARY ALGORITHM** 80
5.1 Multi-Objective Optimization Concepts . . . 80
5.2 Concurrent-Hybrid NSGA-II . . . 83
5.3 Non-dominated Sorting . . . 85
5.4 Constraint Handling . . . 87
5.5 Crowding-Distance Measurement . . . 89
5.6 Crowded-Comparison Operator . . . 89
5.7 Crossover . . . 91
5.7.1 Intermediate Crossover . . . 91
5.7.2 Scattered Crossover . . . 92
5.8 Mutation . . . 92
5.9 Verification using Analytical Test Function . . . 93
6 **MULTI-OBJECTIVE OPTIMIZATION OF NREL 5 MW TURBINE** 98
6.1 Variables . . . 98
6.2 Objective Functions . . . 100
6.3 Constraints . . . 101
6.4 Wind-Turbine Blade Optimization . . . 103
6.4.1 Optimization Problem . . . 103
6.4.2 Results and Discussion . . . 103
7 **CONCLUSIONS** . . . 120
7.1 Conclusions . . . 120
7.2 Recommendations . . . 122
7.3 Future Work . . . 124
Bibliography . . . 126
A Assumptions in Aerodynamic and Structural Models . . . 135
A.1 Aerodynamic Model . . . 135
A.2 Structural Model . . . 135
B Generational Distance for DTLZ2 Test Function . . . 137
C NREL 5 MW Blade Master-Airfoil Data . . . 139

List of Tables

3.1 S809 airfoil data table for Reynolds number of 1.0 million [1] 30

4.1 Material properties used in cross-sectional model [2]. 56

5.1 Summary of algorithms and parameter settings for DTLZ2 test function. Retrieved from [3]. 96

6.1 Basic NREL 5 MW wind-turbine properties. Retrieved from [4]. 104
6.2 Summary of constraint values used in NREL 5 MW blade optimization. . . . 104
6.3 Summary of algorithms and parameter settings for the three-objective NREL 5 MW blade optimization. Retrieved from [3]. 117

List of Figures and Illustrations

1.1 Global annual installed wind capacity between 1996 and 2011. Retrieved from [5]. 2
1.2 Upwind, three-bladed HAWT. Modified from [6]. ©2001 John Wiley & Sons Ltd. 3
1.3 Turbine size growth. Retrieved from EWEA [7]. 5

3.1 Actuator disk concept for a wind turbine. Reproduced from [8]. 26
3.2 The power (C_P) and thrust (C_T) coefficients as a function of the axial induction factor (a). 28
3.3 Blade discretization (left) and the velocity vectors seen by a blade element (top-right) in terms of the induction factors (bottom-right) where θ_t is a combination of the pitch angle (θ) and twist (β), as $\theta_t = \theta + \beta$. Reproduced from [8]. 29
3.4 Lift and drag coefficients as a function of the angle of attack for the S809 airfoil. Retrieved from [9]. 31
3.5 Aerodynamic forces occurring at a local blade element. Reproduced from [8]. 31
3.6 Streamtubes used in BEM. Reproduced from [8]. 33
3.7 C_T as a function of a showing momentum theory and Glauert's empirical relationship when tip-loss effect is ignored. Modified from [10]. 36
3.8 Fixed-speed HAWT with and without pitching to feather. Modified from [6]. ©2001 John Wiley & Sons Ltd. 40
3.9 Fixed (thin vertical line) vs. variable (thick curved line) speed operation. Reproduced from [8]. 41
3.10 Power (a) and thrust (b) curves for a typical pitch-regulated (c) and variable-speed (d) HAWT. 43
3.11 Power coefficient C_P, as a function of λ and θ for a typical HAWT. 44
3.12 2D plot of power coefficient $C_P(+)$, as a function of λ and θ for a typical HAWT. 44
3.13 Thrust coefficient C_T, as a function of λ and θ for a typical HAWT. 45
3.14 2D plot of thrust coefficient $C_T(+)$, as a function of λ and θ for a typical HAWT. 45
3.15 Relative change Δ, for C_P of AWT-27. 46
3.16 2D plots of the computed power coefficient C_P, as a function of λ and θ vs. from WT_Perf for AWT-27. 48
3.17 2D- versus 3D-corrected S809 airfoil data at 33% of the blade span. 50
3.18 Comparison of torque versus wind speed between measurements and BEM with (Replicated) and without (BEM) 3D corrections, for upwind, 0° yaw NREL turbine. Measured data, and Chaviaropoulos and Hansen results digitized from [11]. 52

4.1 Photo of an actual wind-turbine blade cross-section taken at NREL in Golden, CO, USA. Credit: Green Career Central (http://www.greencareercentral.com). 54
4.2 Typical box-type layup at a wind-turbine blade cross-section. 56

4.3 Cross-section showing laminate thickness calculation (left) using upper and lower airfoil profile slopes (right). 57
4.4 A multi-laminated cross-section scaled in proportion to the blade element chord. 58
4.5 Cross-section showing relevant structural properties (ξ enlarged for clarity). . 61
4.6 Double-ellipse cross-section at blade root (left) and tip (right) of an arbitrary wind-turbine blade. 62
4.7 Comparison of computed, PreComp, and analytical linear mass m, of an arbitrary blade using double-ellipse model. 63
4.8 Comparison of computed, PreComp, and analytical stiffness $EI_{x,\mathrm{SC}}$ and $EI_{y,\mathrm{SC}}$, of an arbitrary blade using double-ellipse model. 63
4.9 Comparison of computed, PreComp, and analytical PE coordinates x_{PE} and y_{PE}, of an arbitrary blade using double-ellipse model. 64
4.10 Comparison of computed, PreComp, and analytical orientation of principal inertia axes ξ_{CM}, of an arbitrary blade using double-ellipse model. 64
4.11 Relative change Δ, for linear mass m, and stiffness $EI_{x,\mathrm{SC}}$ and $EI_{y,\mathrm{SC}}$, of an arbitrary blade using double-ellipse model. 66
4.12 Relative change Δ, for PE coordinates x_{PE} and y_{PE}, and orientation of the principal inertia axes ξ_{CM}, of an arbitrary blade using double-ellipse model. . 66
4.13 Relative change in slope Δ_{slope}, between outer and inner contours (bottom) for double-ellipse model at varying relative thickness (t/c) (top). 68
4.14 Comparison between inner contours from computed results and analytical solution. An outer ellipse with 20% relative thickness ($t/c = 0.2$) and $0.09c$ laminate thickness is shown. 69
4.15 Comparison of computed and PreComp linear mass m, of an arbitrary blade for box-type layup. 69
4.16 Comparison of computed and PreComp stiffness $EI_{x,\mathrm{SC}}$ and $EI_{y,\mathrm{SC}}$, of an arbitrary blade for box-type layup. 70
4.17 Comparison of computed and PreComp PE coordinates x_{PE} and y_{PE}, of an arbitrary blade for box-type layup. 70
4.18 Comparison of computed and PreComp orientation of the principal inertia axes ξ_{CM}, of an arbitrary blade for box-type layup. 71
4.19 A wind-turbine blade modelled as a beam. Reproduced from [8]. 72
4.20 Free body diagram for an infinitesimal piece of the beam. Reproduced from [8]. 73
4.21 Computed aerodynamic load about the first principal axis vs. from Hansen [8] for 2 MW Tjæreborg turbine at $V_o = 10\,\mathrm{m/s}$. 75
4.22 Computed bending moment about the first principal axis vs. from Hansen [8] for 2 MW Tjæreborg turbine at $V_o = 10\,\mathrm{m/s}$. 75
4.23 Simple distributed loads on a cantilever beam gives an analytical solution for the deflections. 76
4.24 Computed normal (δ_z) and tangential (δ_y) deflections vs. analytical results. . 76
4.25 Blade element spar-cap thickness (SCT) (a), bending stiffness (b), bending moment (c), and flapwise deflection (d) distributions for an arbitrary blade. Retrieved from [3]. 77
4.26 Cross-section showing structural properties and strain measurement locations (ξ enlarged for clarity). Retrieved from [3]. 78

5.1 Illustrating the projection of a feasible (A) and infeasible (B) reference point onto the Pareto front (thick lines). Reproduced from [12]. ©2009 Massachusetts Institute of Technology. 82
5.2 A set of individuals and the first non-dominated front are shown. Reproduced from [13]. ©2001 John Wiley & Sons Ltd. 86
5.3 A set of individuals classified into different non-dominated levels (or fronts). Reproduced from [13]. ©2001 John Wiley & Sons Ltd. 86
5.4 Constraint handling through selection in a bi-objective problem, where the shaded area represents the feasible region. Reproduced from [13]. ©2001 John Wiley & Sons Ltd. 88
5.5 Crowding-distance calculation. Individuals marked in filled circles are on the same front. Reproduced from [14]. ©2002 IEEE. 90
5.6 Intermediate crossover for two arbitrary parents $\mathbf{x}^{(1)}_{Parent}$ and $\mathbf{x}^{(2)}_{Parent}$, where $u_o = 0.9$ and $u_o = 0.3$ produces two children $\mathbf{x}^{(1)}_{Child}$ and $\mathbf{x}^{(2)}_{Child}$, respectively. . 91
5.7 Scattered crossover for two arbitrary parents $\mathbf{x}^{(1)}_{Parent}$ and $\mathbf{x}^{(2)}_{Parent}$, producing two distinct children $\mathbf{x}^{(1)}_{Child}$ and $\mathbf{x}^{(2)}_{Child}$. 92
5.8 Three-objective DTLZ2 Pareto front ($|PF_{true}| = 441$ shown for clarity). Retrieved from [3]. 94
5.9 Algorithm convergence for the three-objective DTLZ2 test function using $|PF_{true}| = 10,000$ and 10 runs for GD calculation. Retrieved from [3]. 97
5.10 Comparison of computed results between hybrid (left) and non-hybrid (right) NSGA-II at 10,000 objective-function evaluations ($|PF_{true}| = 441$ shown for clarity). Retrieved from [3]. 97

6.1 Control points (CPs) and $\gamma_{airfoil}$ determine the blade element (BE) values for twist (a), chord (b), and thickness distributions (c)–(d). Retrieved from [3]. . 99
6.2 Rotated views of the Pareto front for the NREL 5 MW blade optimization including NREL 5 MW blade (circle) and a Pareto-optimal solution (PO–star). Retrieved from [3]. 105
6.3 2D slice in AEP/AEP$^{\text{NREL}}$–$M_{flap,root}/M^{\text{NREL}}_{flap,root}$ plane where $m_{blade}/m^{\text{NREL}}_{blade} = 1$ for NREL 5 MW blade optimization including NREL 5 MW blade (circle) and a Pareto-optimal solution (PO–star). 106
6.4 2D slice in $M_{flap,root}/M^{\text{NREL}}_{flap,root}$–$m_{blade}/m^{\text{NREL}}_{blade}$ plane where AEP/AEP$^{\text{NREL}} = 1$ for NREL 5 MW blade optimization including NREL 5 MW blade (circle). . 107
6.5 Blade element twist (a), chord (b), and thickness (c)–(d) distributions for the NREL 5 MW blade and a Pareto-optimal (PO) solution. Retrieved from [3]. 108
6.6 Blade geometry views of NREL 5 MW. 109
6.7 Blade geometry views of a Pareto-optimal solution. 110
6.8 Power (a) and thrust (b) curves, and pitch (c) and RPM (d) schedules for the NREL 5 MW blade and a Pareto-optimal (PO) solution. 111
6.9 Blade element tangential aerodynamic force p_t, at the wind speed where $M_{flap,root}$ is a maximum for the NREL 5 MW blade and a Pareto-optimal (PO) solution. 112

6.10 Blade element normal aerodynamic force p_n, at the wind speed where $M_{flap,root}$ is a maximum for the NREL 5 MW blade and a Pareto-optimal (PO) solution. 113
6.11 Differential power coefficient dC_P, for the NREL 5 MW blade and a Pareto-optimal (PO) solution at the variable-speed region. 113
6.12 Blade element spar-cap thickness (SCT) (a), bending stiffness (b), bending moment (c), and flapwise deflection (d) distributions for the NREL 5 MW blade and a Pareto-optimal (PO) solution. 115
6.13 Algorithm convergence for the three-objective NREL 5 MW blade optimization. Retrieved from [3]. 117
6.14 Value of the achievement scalarizing function (ASF) for DTLZ2 and blade optimization problems. Regular y-axis scale (left) and magnified (right). Retrieved from [3]. 119

B.1 Maximum, minimum, and mean GD for the three-objective DTLZ2 test function using $|PF_{true}| = 10,000$ and 10 runs for GD calculation. Hybrid NSGA-II versus NSGA-II. 137
B.2 Maximum, minimum, and mean GD for the three-objective DTLZ2 test function using $|PF_{true}| = 10,000$ and 10 runs for GD calculation. Hybrid NSGA-II versus *gamultiobj*. 138

C.1 NREL 5 MW airfoil profiles. Retrieved from [15]. 139
C.2 NREL 5 MW airfoil lift coefficients for Reynolds number of 6-7 million. Retrieved from [15]. 140
C.3 NREL 5 MW airfoil drag coefficients for Reynolds number of 6-7 million. Retrieved from [15]. 140

List of Abbreviations and Symbols

Abbreviation	Definition
2D	two dimensional
3D	three dimensional
AEP	annual energy production
ASF	achievement scalarizing function
AWT-27	advanced wind turbine - 27 m
BE	blade element
BEM	blade element momentum
BET	blade element theory
CFD	computational fluid dynamics
CM	centre of mass
COE	cost of energy
CP	control point
DCD	dynamic crowding distance
DE	differential evolution
DTLZ	Deb, Thiele, Laumanns, and Zitzler
EA	evolutionary algorithm
ES	evolution strategies
EWEA	European Wind Energy Association
FAST	fatigue, aerodynamics, structures, and turbulence
GA	genetic algorithm
GD	generational distance
GeDEM	genetic diversity evaluation method
GWEC	Global Wind Energy Council
HAWT	horizontal-axis wind turbine
MFD	method of feasible directions
MMFD	modified method of feasible directions
MOEA	multi-objective evolutionary algorithm
MOO	multi-objective optimization
NREL	National Renewable Energy Laboratory
NSGA	non-dominated sorting genetic algorithm
NWTC	National Wind Technology Center
PE	point of elasticity
PO	Pareto-optimal solution
PreComp	pre-processor for computing composite blade structural properties
PSO	particle swarm optimization
RPM	revolutions per minute
SBX	simulated binary crossover
SC	shear centre
SCT	spar-cap thickness
SMS-EMOA	$\mathcal{S}$ metric selection evolutionary

	multi-objective optimization algorithm
SOO	single-objective optimization
SPEA	strength pareto evolutionary algorithm
SQP	sequential quadratic programming
UAE	unsteady aerodynamics experiment
VABS	variational asymptotic beam sectional analysis
VAWT	vertical-axis wind turbine
WT_Perf	wind turbine performance
ZDT	Zitzler, Deb, and Thiele

Latin Symbol	Definition
A	area
A_o	planform area of original blade design
a	axial induction factor
a'	tangential induction factor
$\bar{a}$	average induced velocity from the streamtube
a_b	induced velocity at the blade
B	number of blades
C_d	drag coefficient
$C_{d,\mathrm{3D}}$	3D-corrected drag coefficient
C_F	capacity factor
C_l	lift coefficient
$C_{l,\mathrm{3D}}$	3D-corrected lift coefficient
C_n	normal force coefficient
C_P	power coefficient
$C_{P,opt}$	power coefficient at optimum
$C_P^{\mathrm{WT\_Perf}}$	power coefficient computed by WT_Perf
$C_P^{\mathrm{Betz\text{-}Jouk.}}$	power coefficient at Betz-Joukowksky limit (16/27)
C_T	thrust coefficient
C_t	tangential force coefficient
c	chord length
CD	crowding distance
CP	control point
$\mathrm{CP}_{u,twist}$	control point for twist, where $u = 1, 2, \ldots, N_u$
$\mathrm{CP}^L_{u,twist}$, $\mathrm{CP}^U_{u,twist}$	lower- and upper-bound control point for twist respectively
$\mathrm{CP}_{v,chord}$	control point for chord, where $v = 1, 2, \ldots, N_v$
$\mathrm{CP}^L_{v,chord}$, $\mathrm{CP}^U_{v,chord}$	lower- and upper-bound control point for chord respectively
E	elastic modulus
E^{Shell}	equivalent elastic modulus of shell
EI	bending stiffness (a.k.a. moment of stiffness inertia)
EI_1	bending stiffness about the first principal axis
EI_2	bending stiffness about the second principal axis
$EI_{1,\mathrm{NREL}}$	bending stiffness about the first principal axis for NREL 5 MW
$EI_{1,\mathrm{PO}}$	bending stiffness about the first principal axis for PO
$EI_{2,\mathrm{NREL}}$	bending stiffness about the second principal axis for NREL 5 MW

$EI_{2,\mathrm{PO}}$	bending stiffness about the second principal axis for PO
EI_x, EI_y	bending stiffness about the x- and y-axis respectively
EI_{xy}	moment of centrifugal stiffness
EA_{total}	effective longitudinal stiffness
$ES_{x,total}$	effective moment of stiffness about the x-axis
$ES_{y,total}$	effective moment of stiffness about the y-axis
$EI_{x,total}$	effective bending stiffness about the x-axis
$EI_{y,total}$	effective bending stiffness about the y-axis
$EI_{xy,total}$	effective moment of centrifugal stiffness
$EI_{x,\mathrm{PE}}$	$EI_{x,total}$ translated to the point of elasticity
$EI_{y,\mathrm{PE}}$	$EI_{y,total}$ translated to the point of elasticity
$EI_{xy,\mathrm{PE}}$	$EI_{xy,total}$ translated to the point of elasticity
F	Prandtl's tip-loss factor
$\mathcal{F}_i$	front, where $i = 1, 2, \ldots$, etc.
f_P	expression used to calculate F
$f(V_o)$	wind speed probability of a candidate site
H	hub height
h_1, h_2, h_3	calibration constant one, two and three respectively
I	second moment of inertia
I_x, I_y	second moment of inertia about the x- and y-axis respectively
I_{xy}	product of inertia
$\mathcal{K}_i$	front (for local search)
l	iteration (generation) number
M_1	bending moment about the first principal axis
M_2	bending moment about the second principal axis
$M_{1,\mathrm{NREL}}$	bending moment about the first principal axis for NREL 5 MW
$M_{1,\mathrm{PO}}$	bending moment about the first principal axis for PO
$M_{2,\mathrm{NREL}}$	bending moment about the second principal axis for NREL 5 MW
$M_{2,\mathrm{PO}}$	bending moment about the second principal axis for PO
$M_{flap,root}$	flapwise root-bending moment
M_y, M_z	bending moment about the y- and z-axis respectively
$M_y^{(N)}$, $M_z^{(N)}$	bending moment about the y- and z-axis at tip respectively
m	linear mass (mass/length)
$\dot{m}$	mass flow rate of air
m_{blade}	blade mass
N	number of blade elements
N_d	number of equality constraints
N_e	number of in-equality constraints
N_{pop}	population size
N_u	number of control points for twist
N_v	number of control points for chord
N_w	number of master airfoils plus one
$N_{z,norm}$	normal force in/out of x-y plane
n	number of decision variables

P	power
P_l	population at iteration (generation) l
P_o	initial population
P_{opt}	power at optimum
P_{rated}	rated power
P_{wind}	total power from wind
P_l^{local}	saw-tooth probability function
p_m	mutation probability
p_n	normal aerodynamic force per length of blade
p_t	tangential aerodynamic force per length of blade
p_y	aerodynamic load per length of blade in y-direction
p_z	aerodynamic load per length of blade in z-direction
PF_{true}	true Pareto front
Q	torque
Q_l	offspring population
Q_{opt}	torque at optimum
q	number of objective functions
r	radius from centre of rotation
r_{hub}	hub radius
r/R	non-dimensional radius from centre of rotation
R	rotor radius
Re	Reynolds number
R_l	combined parent and offspring population
RS	ranking score
S	first moment of area
S_x, S_y	first moment of area about the x- and y-axis respectively
T	thrust
T_y, T_z	shear force in y- and z-direction respectively
$T_y^{(N)}$, $T_z^{(N)}$	shear force in y- and z-direction at tip respectively
t	airfoil dimensional thickness
t_s	time
t/c	relative thickness
u	wind speed at rotor disk
u_o	uniformly distributed pseudo-random number between 0 and 1
u_1	wind speed at rotor wake
V_o	undisturbed wind speed
$V_{o,cut\text{-}in}$	minimum (cut-in) wind speed
$V_{o,cut\text{-}out}$	maximum (cut-out) wind speed
V_{rel}	relative velocity
W	induced velocity
w_i	weight, where $i = 1, 2, \ldots, q$
X	feasible region
x_{PE}	point of elasticity x-coordinate
x_k	decision variable, where $k = 1, 2, \ldots, n$

x_k^L, x_k^U	lower and upper bound of decision variable respectively
$x_{k,Child}$	decision variable of child
$x_{k,Mut.Child}$	decision variable of mutated child
y_{PE}	point of elasticity y-coordinate
z_i	objective function
$\bar{z}_i$	objective function of reference point
z_i^{max}	maximum objective-function value
z_i^{min}	minimum objective-function value

Greek Symbol	Definition
α	angle of attack
β	twist
$\gamma_{airfoil}$	r/R of master airfoils
$\gamma_{w,airfoil}$	r/R of master airfoil, where $w = 1, 2, \ldots, N_w$
$\gamma_{w,airfoil}^L$, $\gamma_{w,airfoil}^U$	lower- and upper-bound r/R of master airfoil respectively
Δ	relative change
Δp	pressure drop
δ_{max}	maximum normal (flapwise) tip deflection
δ_n, δ_{flap}	normal (flapwise) deflection
δ_t	tangential (edgewise) deflection
δ_y, δ_z	deflection in y- and z-direction respectively
$\delta_y^{(1)}$, $\delta_z^{(1)}$	deflection in y- and z-direction at root respectively
δ_{flap}^{tip}	normal (flapwise) tip deflection
ε	strain
ε_1, ε_2	strain due to M_1 and M_2 respectively
$\varepsilon_{1,max}$, $\varepsilon_{2,max}$	maximum strain due to M_1 and M_2 respectively
ζ, $\bar{\zeta}$	polynomial-mutation parameter 1 and 2 respectively
η_m	mutation distribution index
θ	blade-pitch angle
θ_{opt}	blade-pitch angle at optimum
θ_t	blade-pitch angle plus twist ($\theta + \beta$)
κ_1	curvature about the first principal axis
κ_2	curvature about the second principal axis
κ_y, κ_z	curvature about the y- and z-axis respectively
λ	tip speed ratio
λ_{opt}	tip speed ratio at optimum
λ_r	local speed ratio
μ	r/R
ξ	principal stiffness angle
ξ_{CM}	orientation of principal inertia axes referenced to the centre of mass
ρ	density
ρ_{air}	density of atmospheric air
ρ_{o}	augmentation coefficient

ρ^{Shell}	equivalent density of shell
σ	blade solidity
τ	skin thickness
ϕ	flow angle
ψ_y, ψ_z	slope in y- and z-direction respectively
$\psi_y^{(1)}$, $\psi_z^{(1)}$	slope in y- and z-direction at root respectively
ω	rotor angular velocity

Bold Symbol	Definition
$\mathbf{w}$	weighting vector
$\mathbf{x}$	decision vector
$\mathbf{x}^{(1)}$, $\mathbf{x}^{(2)}$	decision vector of individual 1 and 2 respectively
$\mathbf{x}_{Child}^{(1)}$, $\mathbf{x}_{Child}^{(2)}$	decision vector of child 1 and 2 respectively
$\mathbf{x}_{Parent}^{(1)}$, $\mathbf{x}_{Parent}^{(2)}$	decision vector of parent 1 and 2 respectively
$\mathbf{z}$	objective vector
$\bar{\mathbf{z}}$	objective vector of reference point

Other Symbol	Definition
$[\dots]^{\text{Shell}}$	property of shell
$[\dots]^{\text{Spar Caps}}$	property of spar caps
$[\dots]_{layer}^{\text{Webs/Panels}}$	property of shear web or panel layer
$\mathcal{F}_i(\dots)$	individual belonging to front $\mathcal{F}_i$
$f_i(\dots)$	objective function
$\mathbf{f}(\dots)$	objective vector
$g_d(\dots)$	equality-constraint function
$h_e(\dots)$	inequality-constraint function
$\in$	is an element of
$\cup$	union
$\emptyset$	empty set
$\mathbb{R}^n$	n-dimensional real numbers
$\prec_n$	crowded-comparison operator
$[\dots]^{\text{NREL}}$	value for NREL 5 MW

Chapter 1

INTRODUCTION

1.1 Need for Wind Energy

Global climate change, air pollution and acid rain have generally been accepted in today's society to be caused by humanity's fossil fuel consumption. Fossil fuels emit harmful pollutants such as carbon dioxide gas, a major contributor to the greenhouse effect. Meeting the future's need for energy without further damage to the environment depends on implementing cleaner alternative-energy solutions. In particular, renewable energy resources are the ideal candidates for reducing humanity's fossil fuel dependency and the harmful pollutants associated with it. With the current continuous increase in global demand for power, renewable energy technologies are becoming more important and must be deployed quickly and extensively.

Examples of renewable energy include solar energy, biofuels, hydropower, geothermal energy and ocean tidal and wave energy. Wind power, through the use of wind turbines, is now one of the most cost-effective and environmentally-friendly methods of generating electricity. An economic and rapid reduction in carbon dioxide emissions can be achieved by large-scale deployment of wind energy. All emissions from a wind turbine construction are offset within the first three to six months of operation. For its remaining 20 year lifetime, wind turbines run emissions free [16].

As projected by the Global Wind Energy Council (GWEC) [5], the annual installed wind capacity across the globe will continue to grow as shown in Figure 1.1. Following the earthquake, tsunami and nuclear disaster of March 11, 2011 in Japan, the world is calling for a transformation of the energy system towards more renewables such as wind power. The German government has decided to phase out all nuclear power by 2020 and has installed

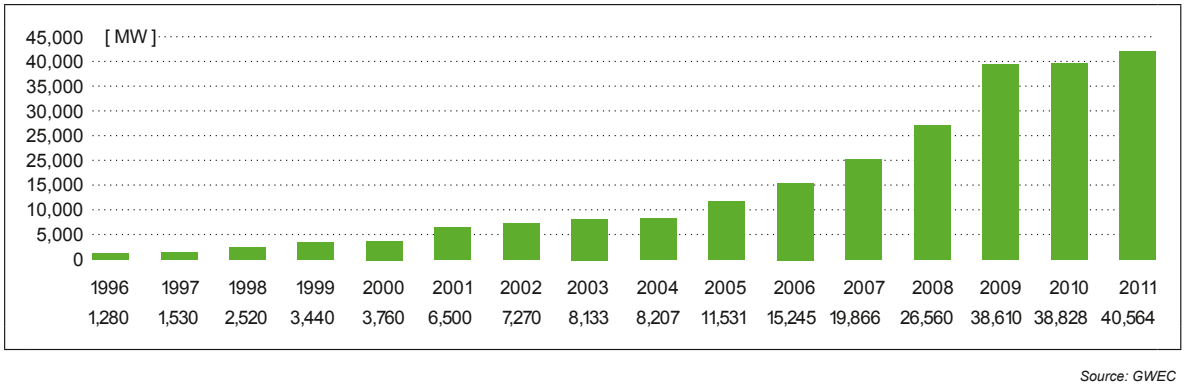

Figure 1.1: Global annual installed wind capacity between 1996 and 2011. Retrieved from [5].

the most wind power of all countries in Europe in 2011.

However, like all other power sources, renewable and non-renewable, wind power does come with its own potential drawbacks. Similarly with solar energy, wind power is an intermittent energy source that can only be used when nature supplies it. If wind is not available when there is a need for energy, electricity must be obtained from a substitute energy source. Conversely, when there is a surplus of wind, the energy must be stored or exported elsewhere. Conventional power sources such as fossil fuel power plants do not depend on the unpredictability of weather conditions.

Other potential drawbacks include noise, visual impact, shadow flickering caused by the sun and rotating blades, electromagnetic interference, collisions with birds and bats, and interference with military aviation. However, a majority of these drawbacks can be dealt with in different ways and are becoming less of an issue in recent years. For offshore wind energy installations, noise, visual impact and flicker are becoming insignificant due to their more remote locations. The positive aspects of wind power outweigh the negative.

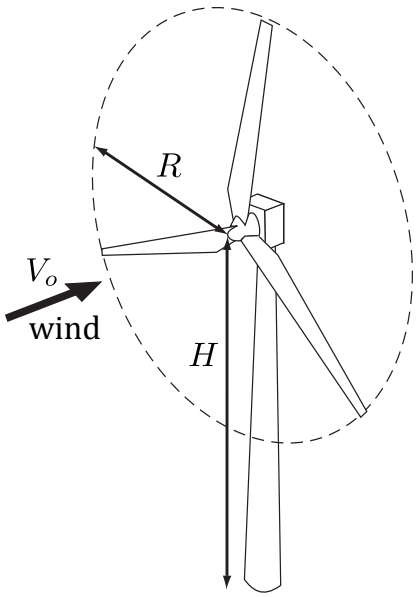

Figure 1.2: Upwind, three-bladed HAWT. Modified from [6]. ©2001 John Wiley & Sons Ltd.

1.2 Wind Turbine Types

Two types of modern wind turbines in use today are horizontal-axis wind turbines (HAWT) and vertical-axis wind turbines (VAWT). When the rotor axis is aligned horizontally or in the direction of the wind, the turbine is called a HAWT. When the rotor axis is aligned vertically or perpendicularly to the wind direction, the turbine is called a VAWT. In the current market, HAWTs are commercially more competitive and hence significantly outnumber VAWTs. Even though VAWTs are generally more expensive, it is important to know that they do have some advantages over HAWTs.

The most predominant type of HAWT has three blades and an upwind configuration as shown in Figure 1.2. The rotor radius is denoted by the letter R and the hub height as the letter H. The length of the blades is obtained by subtracting the hub radius r_{hub}, from R.

There exist subgroups within the HAWT class that are based on the control strategies employed to ensure that the turbine operates within its design range. The most common control strategies involve variable speed and pitch regulation. A variable-speed HAWT can adjust the rotational speed whereas a pitch-regulated one can adjust the angles of the blades

relative to the plane of rotation. A pitch-regulated and variable-speed HAWT is the most common configuration that implements both control strategies and will be the focus for Chapters 3–6. Pitch regulation and variable-speed operation are discussed in section 3.4 of this thesis.

1.3 Power from the Wind

The total power from the wind comes in the form of kinetic energy expressed by:

$$P_{wind} = \frac{1}{2}\dot{m}V_o^2 \tag{1.1}$$

where $\dot{m}$ is the mass flow rate and V_o is the wind speed. The above equation can be rewritten in the following form:

$$P_{wind} = \frac{1}{2}\rho_{air}AV_o^3 \tag{1.2}$$

in terms of the air density ρ_{air}, and the swept area of the rotor, $A = \pi R^2$. Ideally for power extraction, the kinetic energy from the wind is reduced to zero and converted completely into useful mechanical or electrical energy. This is not achievable realistically, thus the non-dimensional quantity known as the power coefficient C_P, is defined:

$$C_P = \frac{P}{P_{wind}} = \frac{P}{\frac{1}{2}\rho_{air}\pi R^2 V_o^3} \tag{1.3}$$

where C_P is the ratio between the power extracted from the wind P, to the total available power. Studying equation (1.3), it is observed that the power depends on R, C_P, and the air density and wind speed of a site.

The site has a significant impact since power depends on the cube of the wind speed. Hence, it is most favourable to place turbines where the average wind speed is high. The second influential factor is R, where a doubling of R results in four times the power. The increase in power with R explains to a great extent the trend of increasing size throughout the years as shown in Figure 1.3. Besides the reasons given in section 1.1, offshore wind

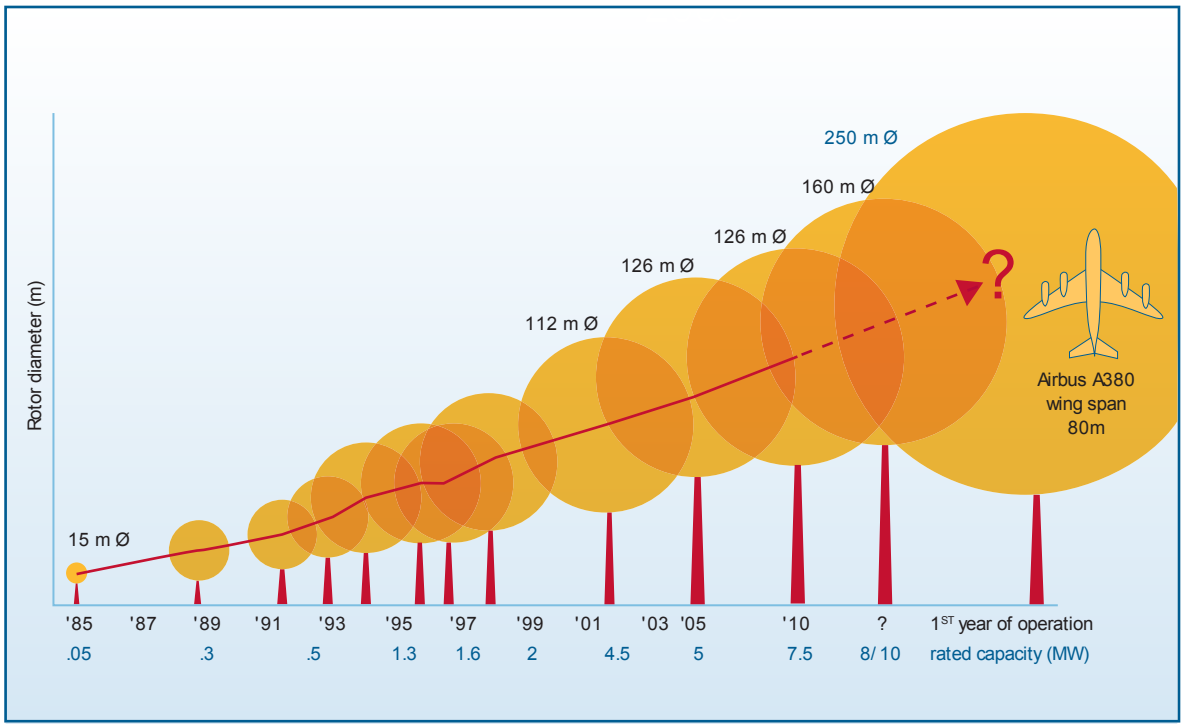

Figure 1.3: Turbine size growth. Retrieved from EWEA [7].

energy installations are also attractive because wind speeds are higher and limitations on R are lower compared to onshore installations.

The power coefficient C_P, depends on the tip speed ratio and the rotor design. For a pitch-regulated turbine, C_P will also depend on the pitch angle of the blades denoted by θ, where θ is the angle between the tip chord and the plane of rotation (see section 3.3.1). The tip speed ratio λ, is the ratio of the rotational speed of the blade tip to the incoming wind speed V_o (i.e. $\lambda = \omega R/V_o$). A maximum value of C_P occurs for one λ and can be achieved for a range of wind speeds by variable-speed operation. Values of λ for maximum C_P in pitch-regulated and variable-speed wind turbines typically range between six and eight.

The theoretical maximum of C_P, known as the Betz–Joukowsky limit [17], is equal to 16/27 but only a C_P of approximately 0.5 can be achieved in practice. The Betz–Joukowsky limit does not represent the maximum efficiency and does not include the efficiency of conversion of mechanical to electrical energy. It is possible to exceed the Betz–Joukowsky limit if the mass flow rate through the rotor is increased, which can be accomplished by placing

the rotor in a diffuser. No such large-scale HAWT employs a diffuser and thus shrouded wind turbines are not studied in this thesis.

1.4 Scope of Thesis

This thesis will focus on the methods used to optimize C_P with respect to rotor design while also considering the blade structural performance. Optimizing C_P does not necessarily mean maximizing the C_P value to attain maximum power as per equation (1.3). A more appropriate target is to maximize the annual energy production (AEP) measured in MWhrs, which is the energy produced by a rotor per year:

$$\text{AEP} = 8760 \int_{V_{o,cut\text{-}in}}^{V_{o,cut\text{-}out}} P(V_o) f(V_o) dV_o \tag{1.4}$$

where 8760 is the number of turbine operating hours per year and $f(V_o)$ is the wind speed probability of a candidate site. The effect of $f(V_o)$ on the AEP is not studied in this thesis, thus the simple and generic Rayleigh probability density function is used. The maximum and minimum wind speeds are $V_{o,cut\text{-}out}$ and $V_{o,cut\text{-}in}$ respectively. The power as a function of the wind speed $P(V_o)$, is known as the *power curve* and is described in detail for a pitch-regulated and variable-speed HAWT in section 3.4.3. The dependency on C_P for the AEP can be observed by combining equations (1.3) and (1.4) that yields:

$$\text{AEP} = 8760 \frac{\pi}{2} \rho_{air} R^2 \int_{V_{o,cut\text{-}in}}^{V_{o,cut\text{-}out}} V_o^3 C_P(V_o, \lambda, \theta) f(V_o) dV_o \tag{1.5}$$

where C_P is a function of V_o, λ and θ for a pitch-regulated and variable-speed HAWT. The goal is therefore to determine C_P such that the integral in equation (1.5) is a maximum.

This thesis studies and applies algorithms for optimizing wind-turbine rotors for AEP and structural performance with the aid of geometric, aerodynamic and structural models. The optimization algorithm and the geometric, aerodynamic and structural models have all been developed by the author using MATLAB® software. Chapter 2 will review the work that

has been done in the past and outline the contributions from this thesis. The aerodynamic model implemented is based on the blade element momentum (BEM) method and will be described in Chapter 3. The structural model is based on a cross-sectional model and Euler-Bernoulli beam theory, and will be described in Chapter 4. A summary of the assumptions involved in the aerodynamic and structural models is provided in Appendix A. In Chapter 5, the optimization algorithm is depicted, which is then applied for the illustrative case of the National Renewable Energy Laboratory's (NREL) 5 MW wind-turbine blade optimization shown in Chapter 6. Lastly, conclusions and future work will be provided in Chapter 7. For further information regarding sections 1.1 to 1.3, see references [5, 6, 7, 16, 17, 18].

Chapter 2

LITERATURE REVIEW

2.1 Introduction

The simultaneous optimization of wind-turbine blade design with respect to the many different and sometimes conflicting requirements is a challenging task. The coupling between the aerodynamics, structural mechanics, acoustics, blade vibrations and other engineering aspects under a number of constraints requires the use of numerical approximation techniques. Purely analytical methods for multi-disciplinary optimization do not exist. Even when considering the aerodynamics alone, analytical methods for optimizing blades are limited. For example, Wilson and Lissaman [19] presented a method of deriving the optimum wind-turbine blade chord and flow angles for the single objective of maximum C_P. The downside of this method is that it requires a prescribed design tip speed ratio and usually the AEP should be considered rather than C_P. The drag of the blade sections was also assumed zero and the tip-loss factors were neglected. Realistically, the drag and the tip loss should be considered when determining the optimum chord and twist.

Numerical methods implemented for wind-turbine blade optimization consist of local and global search algorithms as well as hybrid methods that combine them. Before describing in more detail the numerical methods and their application to wind-turbine blade optimization, the objective-function space must first be studied. The objective-function space will hereafter be referred to as the *objective space*. Many of the concepts described in this chapter are borrowed from Luke [20], who provides a brief and rational overview of the objective space and the field of optimization algorithms.

2.2 Objective Space: Exploitation versus Exploration

Any design problem will have an objective space that is shaped by the range of values of the design (or *decision*) variables. When optimizing a particular design for a single objective, the goal is to attain the global maximum or minimum of the objective space and to extract the corresponding values of the decision variables. The end result is a single optimal solution. In contrast, a multi-objective problem will typically give rise to a set of optimal trade-off (or Pareto-optimal) solutions known as the Pareto-optimal set. It is possible that a multi-objective optimization (MOO) problem has a solution that is optimal in every objective. However, more often than not the objectives are conflicting. In other words, an optimal value for one objective will lead to a non-optimal value for another. The individual who executed a MOO must study the trade-off solutions available to him/her and select the one that is the most suited for his/her applications.

The objective space can be simple; the objective value varies smoothly, continuously and with minimal variations in response to changes in the decision variables. Conversely, some are rapidly changing or stochastic, discontinuous, deceptive, multimodal, or undefined. The performance of a particular type of algorithm largely depends on the objective space under consideration. Hence, an individual who is attempting an optimization would ideally have a good understanding of both the algorithms available and the nature of the objective space. Unfortunately, the nature of the objective space is frequently not known until the objective function has been evaluated a sufficient number of times.

Algorithms with a high degree of *exploitation* are commonly used for most objective spaces because they are the fastest in producing a result. In a exploitative algorithm, an initial design is improved incrementally by local alterations of the decision variables until a local or global optimum is found. Local optimums are designs with the best objective-function value only within the vicinity of the initial design. Global optimums are optimums of the entire objective space. Clearly, a global optimum is much more desirable than a local

optimum. The significant disadvantage of exploitative algorithms is that they usually result in a local optimum.

To attain a global optimum using an exploitative algorithm, either an initial design must be selected that is very near the global optimum or the objective space must be very simple as discussed previously. For example, a very simple objective space would only have a single maxima. This particular objective space would be characterized as unimodal. For the multimodal case, multiple peaks or dips in different magnitudes exist. Exploitative algorithms usually become trapped in local optima for multimodal objective spaces. To increase the probability of attaining a global optimum, *exploration* –the ability to search away from the immediate neighbourhood– must be infused in the algorithm.

The above discussions on the objective space as well as local and global optimality are applicable to both single and multiple objective function optimizations. However, it is important to remember that the number of objective functions may determine the number of optimal solutions typically obtained.

2.3 Gradient-Based Methods

Gradient-based optimization relies on evaluating the derivatives (or finite difference approximations to them) of the objective function and are local search algorithms. They are generally exploitative. Gradient-based techniques perform efficiently only when the function is continuous and differentiable. If the objective function is stochastic, it will likely prematurely converge to a solution that is nowhere near a global or even a local optimum. The derivatives for a stochastic objective function become distorted and when optimality conditions appear to be satisfied at a final point because of noise, the gradient-based algorithm stops. Large steps can be taken in evaluating the derivative to mitigate this problem but the algorithm may take longer to converge to the final solution.

Fuglsang and Madsen [21] employ the method of feasible directions (MFD) for optimizing

a 1 MW stall-regulated rotor for cost performance, defined as the AEP relative to the material consumption. The objective function stated for the optimization is the AEP at a site with the Danish roughness class 1. In the MFD, the sensitivity of the AEP on the decision variables is found by using a forward-difference approximation. The AEP values used in the forward-difference approximation are calculated by perturbing each of the decision variables. Results indicate a potential improvement of cost performance of 11%.

Fuglsang et al. [22] later performed a site-specific design optimization using cost of energy (COE) as the objective. The COE includes both the AEP and turbine component costs, and potentially other costs such as operation and maintenance. A detailed description of the costs included for the COE is shown in the appendix of [22]. Six different sites were investigated comprising of normal flat terrain, offshore and complex terrain. The algorithm employed is not specified, however it is mentioned that numerical differences were used because the exact gradients could not be calculated. Results show that the differences in characteristics of each site had a significant effect on the outcome of the turbine COE.

Lee et al. [23] performed a MOO using a modified method of feasible directions (MMFD) and a probabilistic approach. The probabilistic approach was included to aid the MMFD in reaching a global optimum rather than a local optimum blade shape. Thus by using the probabilistic approach, the disadvantage of the MMFD being a localized optimizer is mitigated. The two objectives of maximum capacity factor (C_F) and minimum blade cost were converted into a single objective using a weight factor. The C_F is defined as the AEP generated during the year, divided by the number of hours in the year multiplied by the turbine rated power P_{rated} (i.e. $C_F = \text{AEP}/(8760\, P_{rated})$. The conversion of a multi-objective problem to a single-objective one using a weight factor is a classical technique called the method of weighted objectives. A set of optimum solutions was then obtained after executing the optimization for different values of the weight factor. This optimum set of solutions (Pareto-optimal set) resulted in an approximation of a trade-off curve known

as the Pareto front. The Pareto front provides information about the compromise between two competing objectives or indicates a global or local maximum. This information can be valuable, which a single-objective optimization (SOO) such as in [21] and [22] cannot provide.

Kenway and Martins [24] optimized the COE for a commercial 5 kW Wes5 Tulipo wind turbine keeping the cost fixed to an original baseline design. In other words, the AEP was the objective being optimized and the cost was held as a constant value. The gradient-based sequential quadratic programming (SQP) method in the commercial software package SNOPT was used to perform the optimization. The BEM method and XFOIL [25] were used in the aerodynamic analysis, while a Timoshenko beam model for the structural. Two different sites were considered for the optimization that resulted in two significantly different optimum blade designs.

Xudong et al. [26] made use of the *fmincon* function in MATLAB to perform a constrained optimization on three different wind-turbine rotors for minimum COE. The COE defined here was simply the ratio of the rotor cost over the AEP. The *fmincon* function implemented is gradient-based because it uses the Hessian to find the minimum of the objective function [27]. The Hessian is the matrix of all second derivatives of the objective function with respect to the decision variables. The optimization was done using an aero-elastic code, which includes structural dynamics and BEM theory models to provide accurate blade performance predictions.

Bottasso et al. [28] also implemented the *fmincon* function, specifically the SQP method in the *fmincon* routine. Conversely to [26], a multi-disciplinary optimization on AEP and blade weight was performed. The two objectives were optimized sequentially in an iterative manner until convergence was achieved. In addition to *fmincon*, Bottaso used another commercial optimization software to allow a more thorough search of the decision space. It is suspected, but not known, that a genetic algorithm (GA) was used as the global optimization solver,

while the SQP was used for localized optimization. This postulation is based on Figure 1 in the paper since a description of the global solver is not given. A high-fidelity aero-servo-elastic model and a detailed cross-sectional structural model were used to compute the AEP and blade weight respectively.

2.4 Evolutionary Algorithms

The genetic algorithm (GA) [29] used in [28] belongs to a larger set of algorithms known as evolutionary algorithms (EAs). Due to their similarity with Darwinian evolution (hence *evolutionary* in EA) many terms from biology are used to describe the various components of EAs. Unlike gradient-based techniques, EAs rely on stochastic operators instead on computing derivatives. For example, the most traditional operators in GAs are called *crossover* and *mutation* (details given in the subsequent paragraph). The stochastic behaviour of EAs allows a global search of the objective space and has the distinct advantage of being capable of handling discontinuous, stochastic and non-differentiable functions. Thus, EAs are generally exploration algorithms whereas gradient-based techniques tend to be exploitative. Unfortunately, the approach implemented in EAs is less efficient than in gradient-based algorithms thus they typically require longer computation times. Hence, when using EAs, it is critical to have objective functions that are as computationally efficient as possible. Computationally intensive objective functions used in conjunction with an EA will result in unreasonable computation times.

In addition to the stochastic based approach, EAs deal with a set of solutions (*population*) rather than a single solution (*individual*) typical of gradient-based methods. Operators such as crossover and mutation are applied to the decision variables of the population in the hope of producing superior individuals. In almost all crossover operators, a portion of the decision variables between two or more individuals (*parents*) are combined when creating new individuals called *children*. To ensure each child is unique (hence enhancing the *diversity*

of the population), the mutation operator applies a slight random alteration of one or more decision variables belonging to the child. For a SOO, the best individual in the population is the end result of the optimization. In MOO, the entire population can be used to approximate the Pareto front in one simulation run. For this reason, EAs are prominent in MOO. In Lee et al. [23], it was necessary to run the optimization several times to attain a Pareto-optimal set. However, modifications to an EA are necessary for MOO applications and as a result these modified EAs belong to a distinctive class known as multi-objective evolutionary algorithms (MOEAs).

One method of converting an EA to a MOEA involves the concept of domination. The well-known non-dominated sorting procedure of Goldberg [29] will be described here. In this procedure, a ranking scheme is used to distinguish superior individuals from the inferior. The first step is to classify the individuals of a population in a multi-objective space as either non-dominated or dominated. Non-dominated individuals are superior to all other individuals in at least one objective function (which may not be same in comparison to different individuals). All other individuals of the population are dominated. The set of non-dominated individuals (*non-dominated* or *Pareto front*) is then assigned the highest ranking score possible (e.g. 1). They are then ignored temporarily and the population is reclassified as non-dominated and dominated. The non-dominated front of the new population is then assigned a rank lower than the previous non-dominated front (e.g. 2). The process is repeated until the entire population is assigned a ranking score. Further description of non-dominated sorting can be found in Chapter 5, section 5.3.

Three primary distinctive types of EAs will be discussed: Genetic algorithm (GA), evolution strategies (ES) and differential evolution (DE).

2.4.1 Genetic Algorithm

Selig and Coverstone-Carroll [30] incorporated an inverse design scheme [31] into a GA for optimizing the AEP of a family of stall-regulated wind-turbine rotors. They named their

computer program PROPGA. The inverse design scheme that was implemented is another separate computer program known as PROPID, which is an extension of the PROP [32] code based on BEM. PROPID allows the determination of blade geometry corresponding to the desired rotor performance and aerodynamic characteristics input by the user. As a result of this approach, certain rotor constraints can be enforced in the GA without the use of constraint-handling techniques such as penalty functions. A penalty function modifies the objective value(s) of the individuals that violate constraints so that they are less likely to be deemed superior to other individuals that do not violate any constraints. Frequently, the worst possible objective value(s) are assigned for the constraint-violating individuals. Because penalty functions are generic, the performance in most cases is not satisfactory [33]. The trade-off studies performed using PROPGA yielded valuable information for wind-turbine blade design.

Giguère and Selig [34] later updated PROPGA to include a MOO capability. In the updated PROPGA, the aerodynamics, structures, noise and cost are considered in the blade geometry optimization. The user can select two objectives from a choice of three, which are minimum COE, maximum AEP or C_P, and minimum rotor thrust or torque. The user may also select the cost of any turbine component instead of the COE for one of the objectives. Unlike in [23], the objectives are not converted into a single objective. The objectives are treated separately by grouping individuals into different Pareto front ranks using non-dominated sorting. Using non-dominated sorting, the trade-off curve was obtained in a single simulation run. The optimization algorithm in PROPGA is a MOEA.

The non-dominated sorting genetic algorithm II (NSGA-II) [14] is another MOEA. NSGA-II combines the non-dominated sorting procedure with a GA and is an improvement from the original NSGA [35] in three respects: The computational complexity is reduced, *elitism* is introduced in the algorithm and the need to specify a *sharing* parameter is removed. When superior individuals are generated within the population at one cycle (*generation*), elitism

ensures that these individuals remain within the population for subsequent generations. This technique is known to improve the convergence of GAs [14]. The sharing function guides the NSGA towards a well-distributed Pareto-optimal set but requires a parameter input by the user. The downside is that the value chosen for this parameter has a significant effect the sharing function's performance and one does not know what the optimum value is for a given problem. Therefore, the sharing function is replaced with the crowded-comparison operator in the NSGA-II, which uses crowding distance as a measure of the density (or diversity) of individuals. When multiple individuals are assigned the same rank, the crowded-comparison operator aids the NSGA-II in selecting the least crowded individuals (see section 5.6). For a real-coded GA within the NSGA-II, the simulated binary crossover (SBX) [36] and polynomial mutation [37] operators are used (see sections 5.7 and 5.8).

An improved version of the NSGA-II has been applied for optimizing the NREL offshore 5 MW baseline wind turbine [4] in Wang et al. [38]. The optimization objectives are maximum C_P at a design wind speed and minimum blade mass. Two improvements were made to the original NSGA-II: 1) the lateral diversity and 2) the uniformity of solutions on the non-dominated front. The crowded-comparison operator discussed previously ensures diversity along a non-dominated front but does not ensure diversity lateral to the non-dominated front (see Figure 2 in [39]). Next, a non-dominated front is considered uniformly distributed only when the non-dominated solutions are equidistant in the objective space. The two improvements were accomplished by incorporating both controlled elitism [39] and a dynamic crowding distance (DCD) approach [40]. All EAs lie at different positions on the exploitation and exploration spectrum, and their placement is directly related to the extent of elitism in the algorithm. Controlled elitism allows the extent of elitism (or lateral diversity) in the NSGA-II to be controlled through a parameter. Next, the methodology used in the NSGA-II to measure the crowding-distance of individuals contains two flaws as noted by Luo et al. [40] that negatively affects the uniformity of solutions. In [40], the DCD is proposed

to account for these two flaws, but the methods will not be discussed in detail here. The crowding-distance measurement is however, explained in Chapter 5, section 5.5.

The NSGA-II was also implemented and modified in [41] where the power coefficient and noise levels were optimized under uncertainty. The source of uncertainty described in [41] was insect contamination, which affects the aerodynamic and acoustic performance of wind-turbine blades. To include the uncertainties as part of their optimization, modifications were made to the non-dominated sorting and crowding-distance measurement in the NSGA-II. In the non-dominated sorting, the values of the ranks were converted from being positive integers to positive real numbers. The non-integer component of the"probabilistic rank" contained information regarding the uncertainty, while the integer component had the same value and purpose as in the original non-dominated sorting procedure.

2.4.2 Evolution Strategies

In addition to the GA in the EA family, evolution strategies (ES) [42] is another type of EA. ES differs from other EAs in that the decision variables are usually altered mainly by the mutation operator. The algorithm typically starts by evaluating the objective-function value (*fitness*) of a randomly generated initial population and *selecting* the fittest individuals (parents) to produce children. The remaining individuals from the population are then eliminated. This selection procedure is called *truncation selection* and is distinctive of ES. The number of parents selected from the population (*mating pool* size) and the total number of children that they produce is chosen by the user. The children then replace or combine with the parent population and the process is repeated. In contrast, GAs most commonly use *tournament selection* whereby the best individual from a number (typically 2) of randomly chosen distinct individuals from the population becomes a parent (see section 5.6). Tournament selection is repeated until the number of parents returned is equal to the size of the mating pool. An application of ES is described by Benini and Toffolo [43] and truncation selection is implied in their step-by-step description of the algorithm. However, in

addition to the mutation operator, they included crossover to alter the decision variables. The crossover operator is a distinguishing feature of GAs, but it has long been included in ES as well.

Benini and Toffolo [43] also implemented a MOEA for optimizing stall-regulated HAWTs similarly as in [34]. The two objectives were to maximize the AEP per square metre of wind park and minimize the COE. Trade-off curves were obtained for different turbine rated powers and were compared to individual commercial turbines. The trade-off curves are also obtained by use of non-dominated sorting. The MOEA used by Benini and Toffolo differs from [34] in the diversity-preserving mechanism and the use of ES instead of the GA. The diversity-preserving mechanisms discussed thus far include the sharing function and crowded-comparison operator. As outlined in [43], the two main goals of a MOEA are 1) convergence to the true Pareto-optimal set and 2) the spread of solutions over the entire Pareto-optimal set. In order to achieve the second main goal, Benini and Toffolo integrated an improved diversity-preserving mechanism that they developed called genetic diversity evaluation method (GeDEM).

The traditional sharing function used in [34] modifies the fitness values (i.e. COE, AEP or C_P, etc...) to maintain diversity in the population. For example, a particular blade geometry (individual) that has dissimilar features in comparison with the rest of the population will have their fitness increased. The amount by which the fitness is increased or decreased is *scaled* in proportion to the individual's level of dissimilarity. As mentioned previously for the NSGA, a parameter input (*scaling factor*) is required. Conversely, Benini and Toffolo's algorithm maintains diversity by including an additional measure together with the Pareto rank score. They call this procedure GeDEM and they used the minimum Euclidean distance in the decision-variable space from another individual as a measure of diversity. In the NSGA-II, the diversity is measured using crowding distance and is evaluated on the objective space rather than the decision-variable space.

2.4.3 Differential Evolution

Differential evolution (DE) [44] is another type of EA. DE is an adaptive mutation algorithm, where the mutation occurs through a vector arithmetic operator between three randomly chosen individuals from the population. At each generation, the magnitude of the mutation changes depending on whether the current population is spread out or condensed. Wood [45] optimized the power and starting performance of small wind-turbine blades using DE and good results were obtained. DE on its own is not a MOEA. To include MOO capabilities to DE, Wood used the method of weighted objectives (similarly as in [23]) and executed the optimization several times to attain the Pareto-optimal set. The Pareto-optimal set could have been obtained in a single run by implementing the dominance concept with DE, however this was not done.

Clifton-Smith [46] optimized small wind-turbine blades with DE as well but with an additional objective function: the aerodynamic noise, which was estimated by using an empirical noise prediction model described in Leloudas et al. [47]. Once again, the method of weighted objectives was used but this time a three-dimensional (3D) Pareto front approximation was obtained. The 3D surface displayed the optimal trade-offs between C_P, starting time and aerodynamic noise. From all the wind-turbine blade optimizations found in the literature, Clifton-Smith's is the only case where a 3D surface was obtained. Clifton-Smith [46] was not the only one to perform noise minimization for wind-turbine blades, since this was also done by Leloudas et al. [47] (using *fmincon*) and others for large-scale turbines.

2.5 Other Non-Gradient Based Methods

2.5.1 Particle Swarm Optimization

Particle swarm optimization (PSO) [48] is a stochastic and population-based approach that mimics the swarming behaviour of insects, the shoaling of fish and the flocking of birds. A population of individuals in EA terminology is analogous to a *swarm* of *particles* in PSO.

In contrast to an EA, the PSO algorithm does not involve any selection or crossover in the population. Particles simply *move* or mutate towards promising regions of the objective space. The movement of the particles are represented by velocity vectors, which are computed by a vector arithmetic much like the DE mutation operator. An inertia weight was later introduced by Shi and Eberhart [49] into the PSO algorithm that allows the balancing between global and local search. The inertia weight can be a function of time or a constant but [49] focussed mostly on the latter.

Liao, Zhao and Xu [50] implemented their own improved PSO algorithm for minimizing the blade mass of a 1.5 MW wind turbine. The improvements include a logarithmic inertia weight that monotonically decreases through each iteration and the addition of a selection operator employed by GAs. The type of selection operator and the reasoning as to why it improves the PSO algorithm is not given. The models used in their optimization are third-party codes and the decision variables are the thickness and location of the layers in the spar caps. A reduction in blade mass was achieved.

Another application of PSO is found in Yang et al. [51], who optimized the power of a 2 MW HAWT. The aerodynamic model implemented involves computing the circulation along the wind-turbine blade axis by means of the Biot-Savart theorem, Kutta-Joukowski lift formula, and wing-section theory. The decision variables were the chord and twist distributions of the wind-turbine blade.

2.5.2 Complex Method

A *complex method* was employed by Zhiquan, Xiong, and Yan [52] to optimize the AEP of a 600 kW wind turbine. Much like EAs, the complex method does not rely on gradients. The complex method searches for the optimum by constructing vertices in a feasible domain. A vertex is a point where two or more lines or edges intersect in geometrical shapes such as polygons or triangles [53]. The geometrical shape formed by the vertices in unconstrained optimization problems is known as a simplex. For constrained optimization problems, the

geometrical shape is a complex. The Nelder-Mead simplex method [54] is a well-known unconstrained optimization solver that was extended by Box [55] to handle boundary and non-linear constraints. The complex formed by the vertices changes shape throughout the optimization according to the objective function evaluated at each of the vertices. The vertex with the worst objective-function value is discarded and a new one is formed. Once the centre of the complex has reached the optimum point under the required degree of accuracy, the optimization is terminated. Results show slight improvements in comparison with the 600 kW NM600/43 commercial wind turbine.

2.6 Hybrid Evolutionary and Memetic Algorithms

Hybrid EAs are algorithms that consist both of an EA and a local search technique, and are also called memetic algorithms. The main reason for including local search procedures in an EA is to reduce the number of objective-function evaluations required to attain the optimum solution, thus improving their convergence speed [56, 57]. No such MOO of wind-turbine blades using a hybrid EA has been found in the literature and is therefore investigated in this thesis. It may be argued that Botasso et al. [28] used both a GA and a local solver for their blade optimization, but the algorithms implemented cannot be considered collectively as a hybrid EA. The local search is likely applied after a number of iterations from the GA. Furthermore, it is not a multi-objective algorithm since a single objective is being optimized sequentially. Lee et al. [23] incorporate a probabilistic approach to enhance the global search abilities of their gradient-based local solver, however there is no mention of the use of an EA. In this thesis, a hybridized MOEA and gradient-based local search is developed and applied for the first time, to the author's knowledge, on a MOO of wind-turbine blades.

In addition to the implementation of a hybrid MOEA for optimizing wind-turbine blades, a three-objective optimization will be performed. All large-scale wind-turbine blade MOOs discussed thus far have only been based on a bi-objective problem resulting in a 2D Pareto

front, which may or may not have included constraints that could have been converted into additional objectives. Instead of a trade-off curve obtained in a bi-objective problem, a trade-off surface will be the end result for the three-objective case. The increase in computational resources required for the three-objective case relative to the bi-objective one may be mitigated by the improved convergence properties of the hybrid MOEA.

2.7 Summary

In this chapter, the field of wind-turbine blade optimization was introduced. Initially, analytical methods were studied and found to be limited by crucial assumptions as noted in Wilson and Lissaman's [19] work. As a result, gradient and non-gradient based numerical methods were implemented by researchers for many years in optimizing wind-turbine blades. For any optimization problem where numerical methods are used, a thorough understanding of the objective space is necessary. Therefore, a brief description of the different shapes (or *landscapes*) of objective spaces and their relationship with the degree of exploitation and exploration in an algorithm was given. Examples of gradient and non-gradient based algorithms applied for wind-turbine blade optimization was then outlined.

From the extensive literature review, it was determined that a hybrid MOEA has never been applied for optimizing wind-turbine blades. Furthermore, all MOO studies on large-scale wind-turbine blades have been restricted to a bi-objective problem resulting in a two-dimensional trade-off curve. Consequently, the aim of this project is to develop a hybrid MOEA and apply it for a three-objective wind-turbine blade optimization problem. To justify the potential of using a hybrid MOEA instead of a regular MOEA, a study on convergence is necessary. Chapters 3 and 4 describe the wind-turbine blade aerodynamic and structural models employed for calculating the three objective functions respectively. Chapter 5 describes the hybrid MOEA in detail, which is applied for the three-objective blade optimization as shown in Chapter 6. The study on convergence for analytical test func-

tions and the blade optimization problem is included in Chapters 5 and 6 respectively. The conclusions on the three-objective blade optimization and convergence results are given in Chapter 7.

Chapter 3

AERODYNAMIC MODEL

3.1 Introduction

The aerodynamic model is based on the classical blade element momentum (BEM) method. BEM is commonly used in industry to predict wind-turbine performance due to its simplicity and speed. With BEM, the aerodynamic forces determine the power and thrust for different λ and pitch angles. Two theories constituting BEM are blade element theory (BET) and momentum theory.

The momentum theory component was first conceived by Rankine [58] in 1865 and was later improved by Froude, R.E. [59] (1889) to estimate ship propeller performance using the actuator disc concept. The actuator disc concept replaces the rotor with a permeable disc of zero thickness in a steady-state, frictionless and incompressible flow field. The pressure and velocity are also assumed to be uniform over the area of the disc, but the pressure can be discontinuous across the disc. With these assumptions, Bernoulli's equation with simple one-dimensional continuity and axial momentum theory can be applied to determine the velocity and pressure distributions upstream and downstream of the rotor as well as the velocity and thrust at the rotor plane. Conservation of energy can subsequently be used to determine the power. In 1920, Joukowski [60] included the effects of wake rotation in the theory [17]. An important drawback of momentum theory is that it does not consider the geometry of the blades. In other words, performance properties are obtained for rotors with an infinite number of blades and for real rotors that have a finite number of blades if corrections such as tip-loss factors are applied.

The secondary component, BET, was originated by Froude, W. in 1878 [61] and developed by Drzewiecki (1892, 1920) [62, 63] for the analysis of airplane propellers [64, 65]. There was

also the contribution by Lanchester in 1915 [66] summarized in Glauert [67]. In BET, the blades are divided into a number of blade elements and treated aerodynamically as airfoils (i.e. two-dimensional (2D)). It is assumed that each blade element acts independently and the radial component of the flow along the blade can be ignored. Thus for each blade element, it is possible to determine the aerodynamic forces based on local 2D flow conditions. The aerodynamic forces over the blade length can then be integrated and used to estimate rotor performance. From this approach, one can study the effect of blade geometry such as the shape of the airfoils used, and the twist and chord distributions. However, the effect of the rotor wake on the local flow conditions in BET is generally not known precisely and as a result a crude assumption is often necessary.

The effect of the rotor wake on local blade element flow conditions can be formulated as an induced velocity W, or as a fraction of the undisturbed wind speed V_o, and the blade element rotational velocity ωr, known as the axial and tangential induction factors a and a' respectively (see Figure 3.3). Fortunately, a and a' can be estimated by combining momentum theory with BET. BET, which considers the blade geometry, provides the geometrical aspect that momentum theory does not have. Then, Glauert combined BET and momentum theory to form BEM and applied it for the aerodynamic analysis of airscrew propellers and windmills [67]. Glauert's work was then extended by Wilson for the application to wind turbines [19]. The essential purpose of BEM is to determine the unknown induction factors needed to calculate the aerodynamic performance of a particular wind-turbine rotor design at a given set of flow conditions. The BEM method based on Hansen's formulation [8] is presented in sections 3.2 and 3.3.

3.2 Actuator Disk Concept

This section will briefly show the theory developed by Rankine and Froude in terms of an energy extracting device such as a wind turbine. Consider a streamtube as shown in

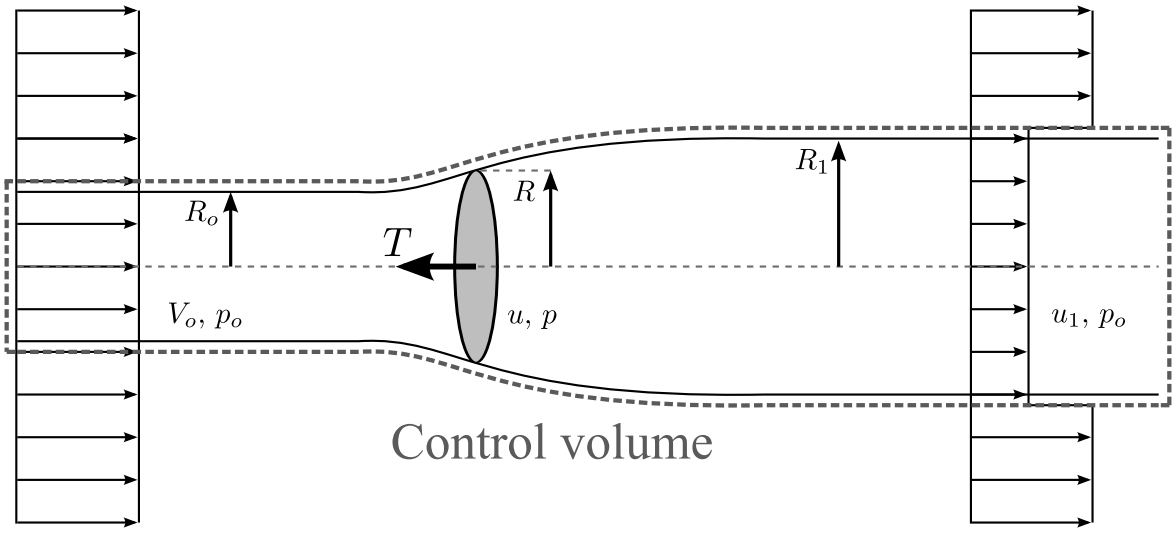

Figure 3.1: Actuator disk concept for a wind turbine. Reproduced from [8].

Figure 3.1 where air enters at V_o, passes through the disk at u, and leaves at u_1 in the wake. Since the disk extracts kinetic energy from the incoming air, u_1 must be less than V_o. The air is also traveling at a low Mach number and thus can be treated as incompressible. Based on these statements and according to continuity:

$$V_o R_o^2 = uR^2 = u_1 R_1^2 \tag{3.1}$$

the flow must expand because $V_o > u > u_1$, hence $R_o < R < R_1$. The thrust T, is the force resulting from the pressure drop (Δp) across the disc expressed as:

$$T = \Delta p \pi R^2 \tag{3.2}$$

which can also be obtained by applying conservation of momentum in the axial direction and using equation (3.1):

$$T = \rho_{air} u \pi R^2 (V_o - u_1). \tag{3.3}$$

Applying Bernoulli's equation between the free stream and just in front of the disc and again between the wake and just behind the disc gives:

$$\Delta p = \frac{1}{2} \rho_{air} (V_o^2 - u_1^2). \tag{3.4}$$

Combining equations (3.2), (3.3), and (3.4) results in:

$$u = \frac{1}{2}(V_o + u_1). \tag{3.5}$$

The axial induction factor a, is denoted by:

$$a = \frac{V_o - u}{V_o}. \tag{3.6}$$

Combining equations (3.5) and (3.6) yields:

$$a = \frac{V_o - u_1}{2V_o}. \tag{3.7}$$

Applying conservation of energy, the power generated is:

$$P = \frac{1}{2}\rho_{air} u \pi R^2 (V_o^2 - u_1^2). \tag{3.8}$$

The power and thrust coefficients are denoted by:

$$C_P = \frac{P}{\frac{1}{2}\rho_{air}\pi R^2 V_o^3} \tag{3.9}$$

and

$$C_T = \frac{T}{\frac{1}{2}\rho_{air}\pi R^2 V_o^2} \tag{3.10}$$

respectively. Combining equation (3.7) with equations (3.8) and (3.9) yields:

$$C_P = 4a(1-a)^2. \tag{3.11}$$

Similarly, combining equation (3.7) with equations (3.3) and (3.10) yields:

$$C_T = 4a(1-a). \tag{3.12}$$

Equations (3.11) and (3.12) are shown graphically in Figure 3.2. It is observed that C_P is a maximum at 16/27 (Betz–Joukowsky limit) when $a = 1/3$. The effects of rotation in the wake and the introduction of the tangential inductor factor a', for the actuator disk concept is provided in [8] and will not be discussed here.

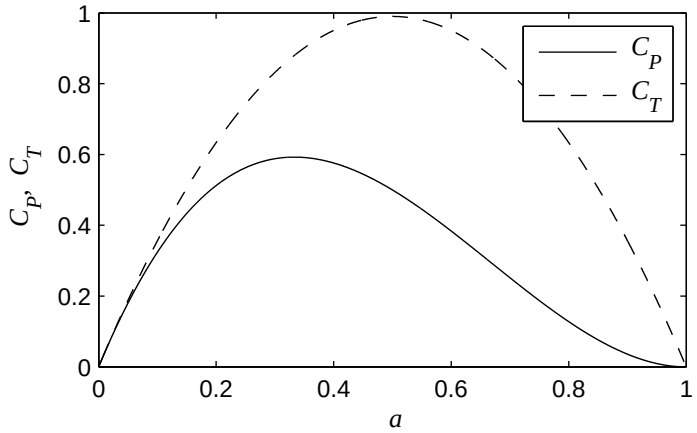

Figure 3.2: The power (C_P) and thrust (C_T) coefficients as a function of the axial induction factor (a).

3.3 Blade Element Momentum Method

3.3.1 Blade Element Theory

Blade element theory begins by discretizing the wind-turbine blade by N number of elements. Each element is of length dr and its cross-section is shown in Figure 3.3. The flow around a blade element is quantified by four components of velocity. The first is the undisturbed wind speed V_o, the second is the rotational velocity of the blade element ωr, and the third is the induced velocity W. By introducing the axial (a) and tangential (a') induction factors, W is decomposed into two separate components in terms of V_o and ωr as shown at the bottom-right of Figure 3.3. The fourth component that is assumed negligible is the velocity of the blade deflections. The wind speed V_o is also assumed to act always in the axial direction normal to the rotor plane. The relative velocity V_{rel}, seen by the blade element is obtained by the vector addition of the three components of velocity. Once the axial and tangential components of V_{rel} are known, the local flow angle ϕ, and the angle of attack α, can be determined by using equations (3.13) and (3.14):

$$\phi = \tan^{-1}\frac{(1-a)V_o}{(1+a')\omega r} = \tan^{-1}\frac{1-a}{(1+a')\lambda_r}, \tag{3.13}$$

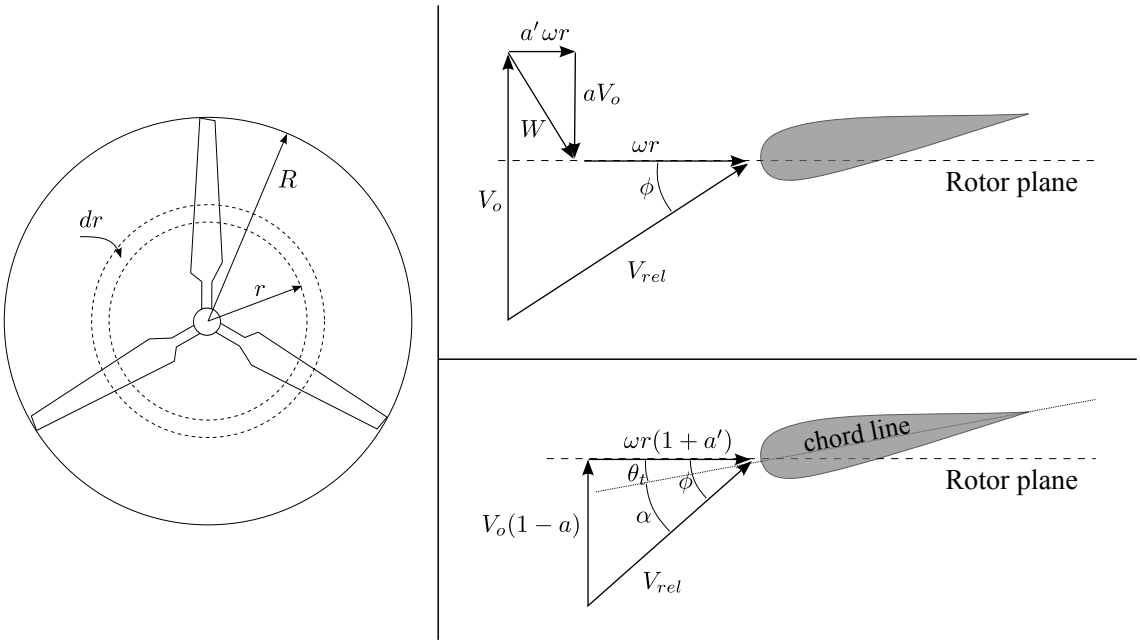

Figure 3.3: Blade discretization (left) and the velocity vectors seen by a blade element (top-right) in terms of the induction factors (bottom-right) where θ_t is a combination of the pitch angle (θ) and twist (β), as $\theta_t = \theta + \beta$. Reproduced from [8].

$$\alpha = \phi - (\theta + \beta) \tag{3.14}$$

where β is the blade-element twist, θ is the blade-pitch angle, and λ_r is the local speed ratio defined as $\lambda_r = \omega r / V_o$. The angle of attack is used to interpolate the lift (C_l) and drag (C_d) coefficients from an airfoil data table typically obtained from either wind tunnel tests or a simulator such as XFOIL and computational fluid dynamics software. For example, Table 3.1 shows the S809 airfoil data obtained from wind tunnel testing at the Delft University of Technology [1]. The data is plotted in Figure 3.4 where the data between $\alpha = 20.16°$ and $\alpha = 30°$ is extrapolated. In the current thesis, high Reynolds number (Re) airfoil data (i.e. $Re \geq 10^6$) typical of large-scale wind-turbine blade sections is used. Since C_l and C_d vary only slightly for high Re, it is assumed that C_l and C_d are independent of Re to simplify the interpolation procedure. Using the lift and drag coefficients, the normal (C_n) and tangential (C_t) force coefficients can be determined for a given ϕ as shown in Figure 3.5 and equations (3.15) and (3.16):

Table 3.1: S809 airfoil data table for Reynolds number of 1.0 million [1]

$\alpha(^\circ)$	C_l	C_d
-1.04	0.019	0.0095
-0.01	0.139	0.0094
1.02	0.258	0.0096
2.05	0.378	0.0099
3.07	0.497	0.0100
4.10	0.617	0.0100
5.13	0.736	0.0097
6.16	0.851	0.0095
7.18	0.913	0.0127
8.20	0.952	0.0169
9.21	0.973	0.0247
10.20	0.952	0.0375
12.23	1.007	0.0636
13.22	1.031	0.0703
14.23	1.055	0.0828
15.23	1.062	0.1081
16.22	1.043	0.1425
17.21	0.969	0.1853
18.19	0.938	0.1853
19.18	0.929	0.1853
20.16	0.923	0.1853

$$C_n = C_l \cos\phi + C_d \sin\phi, \tag{3.15}$$

$$C_t = C_l \sin\phi - C_d \cos\phi. \tag{3.16}$$

Once C_n and C_t are determined for all blade elements, the rotor thrust and torque can be calculated. The differential thrust (dT) and torque (dQ) for each element are given by equations (3.17) and (3.18):

$$dT = Bp_n dr, \tag{3.17}$$

$$dQ = rBp_t dr \tag{3.18}$$

where B is the number of blades, and p_n and p_t are the normal and tangential forces per length evaluated using:

$$p_n = C_n \frac{1}{2} \rho_{air} V_{rel}^2 c, \tag{3.19}$$

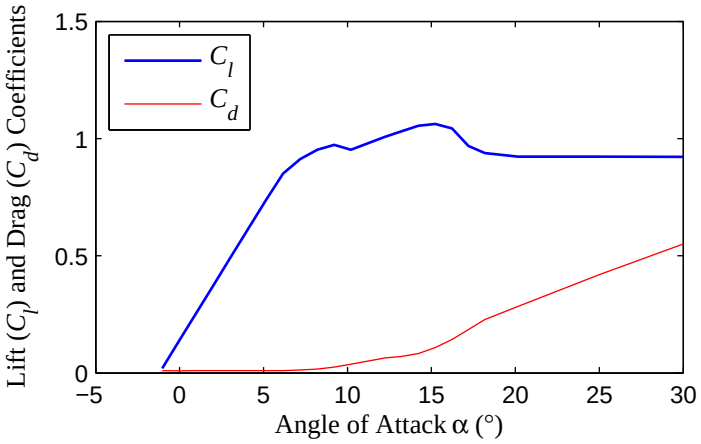

Figure 3.4: Lift and drag coefficients as a function of the angle of attack for the S809 airfoil. Retrieved from [9].

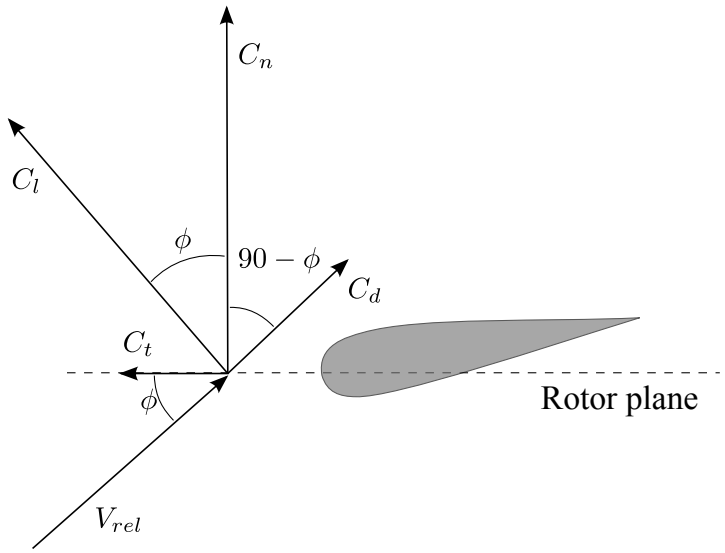

Figure 3.5: Aerodynamic forces occurring at a local blade element. Reproduced from [8].

$$p_t = C_t \frac{1}{2} \rho_{air} V_{rel}^2 c. \tag{3.20}$$

In equations (3.19) and (3.20), the variable c is the chord length of the blade element. From Figure 3.3, V_{rel} is given by:

$$V_{rel} = \frac{(1-a)V_o}{\sin\phi} \tag{3.21}$$

and

$$V_{rel} = \frac{(1+a')\omega r}{\cos\phi}. \tag{3.22}$$

Combining equations (3.17), (3.19) and (3.21) gives:

$$dT = \frac{1}{2} \rho_{air} B \frac{V_o^2 (1-a)^2}{\sin^2\phi} c C_n dr. \tag{3.23}$$

Similarly with equations (3.18), (3.20) and (3.22):

$$dQ = \frac{1}{2} \rho_{air} B \frac{V_o (1-a) \omega r (1+a')}{\sin\phi \cos\phi} c C_t r dr. \tag{3.24}$$

The only unknowns in equations (3.23) and (3.24) are a and a', which are obtained by combining BET with momentum theory.

3.3.2 Momentum Theory

A modified momentum theory is implemented in BEM where the flow through the rotor is assumed to behave as non-interacting circular streamtubes. This method is commonly referred to as strip theory and involves the discretization of a control volume in N streamtubes. This is in contrast to the actuator disk concept described in section 3.2, where the control volume involves no discretization. By dividing the control volume into N streamtubes, the set of equations from momentum theory can be combined with the blade element equations, which were obtained by dividing the blade by N as well. A streamtube of thickness dr is shown in Figure 3.6.

Applying conservation of axial momentum on a streamtube gives an expression for the differential thrust:

$$dT = 4\pi r \rho_{air} V_o^2 a(1-a) dr. \tag{3.25}$$

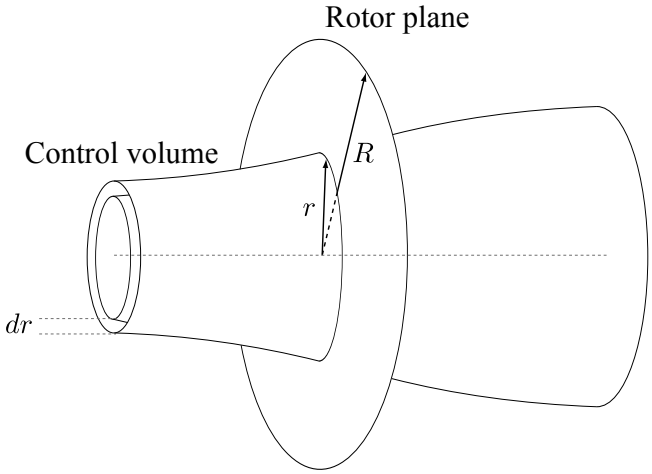

Figure 3.6: Streamtubes used in BEM. Reproduced from [8].

Similarly, applying conservation of angular momentum gives the differential torque:

$$dQ = 4\pi r^3 \rho_{air} V_o \omega (1-a) a' dr. \tag{3.26}$$

The power (dP) is obtained by multiplying dQ with the angular velocity of the rotor, ω:

$$dP = \omega dQ \tag{3.27}$$

Before combining equations (3.25) and (3.26) with equations (3.23) and (3.24), momentum theory must be corrected using Prandtl's tip-loss factor and Glauert's correction.

3.3.2.1 Tip-Loss Factor

The momentum equations ((3.25) and (3.26)) were derived assuming the rotor consisted of an infinite number of blades (i.e. permeable disk). Clearly, turbines in reality only have a limited number of blades and this assumption is not valid. The influence of the vortices shed by a rotor with a finite number of blades on the induced velocity field is different from that of a rotor with an infinite number of blades. These shed vortices are concentrated at the blade tips and create a helical structure in the wake. For an infinite number of blades, the helical structure will be a vortex cylinder, whereas the helical structure for the finite case will consist of B discrete tip vortices. Therefore, a correction should be applied to the induced

velocities near the tip region as a function of B to account for this effect. The inclusion of a tip correction is critical because the aerodynamic forces near the tip greatly contributes to the overall performance of the wind turbine. The most widely used tip correction involves Prandtl's tip-loss factor F, shown in Glauert [67] as the ratio between the average induced velocity from the streamtube $\bar{a}$, and the induced velocity at the blades a_b, which tends to zero near the tip. Prandtl's tip-loss factor presented by Glauert is inconvenient for BEM computations and a simpler approximate expression is given by:

$$F = \frac{2}{\pi} \cos^{-1} e^{-f_P} \tag{3.28}$$

where

$$f_P = \frac{B}{2} \frac{R - r}{r \sin \phi}. \tag{3.29}$$

Using Prandtl's tip-loss factor, the momentum equations ((3.25) and (3.26)) are corrected as follows:

$$dT = 4\pi r \rho_{air} V_o^2 a(1 - a) F dr, \tag{3.30}$$

$$dQ = 4\pi r^3 \rho_{air} V_o \omega (1 - a) a' F dr. \tag{3.31}$$

In Prandtl's derivation, a series of parallel planes with uniform spacing was used to approximate the helical vortex system behind the rotor. A more realistic and accurate analysis was performed by Goldstein [68], however its solution is complex because it involves an infinite series of Bessel functions. Due to the simplifications made by Prandtl, his tip correction has limitations affecting its accuracy. For example, Prandtl's approximation should only be used for high tip-speed ratios and when the number of blades exceeds two. If these limitations are respected, then a similar result to that of Goldstein's is achieved. A more recent tip correction was proposed by Shen et al. [69], which they claim results in better aerodynamic load predictions near the tip. However, Clifton-Smith [70] found that the suitability of the tip correction by Shen et al. to be highly questionable from an aerodynamic point of view for blade optimizations. Despite the more accurate tip-correction models available in the

literature such as those discussed in [68] and [69], Prandtl's is used here because of its simple implementation.

3.3.2.2 High-Thrust Correction

When the axial induction factor a, becomes approximately 0.4, the turbine enters in the *turbulent-wake state*. This occurs when the turbine is operating at low wind speeds with constant rotation (i.e. high values of λ). In the turbulent-wake state, the thrust coefficient C_T, deviates from momentum theory as shown by the experimental data [71] plotted in Figure 3.7. According to momentum theory, see equation (3.7), the speed of the flow in the rotor wake u_1 becomes zero at $a = 0.5$ and negative for $a > 0.5$. This implies that the wake begins to propagate upstream, which does not occur in reality. As a increases past 0.4, turbulence in the rotor wake develops and increases. Consequently, the flow in the wake slows down but C_T continues to increase.

Glauert proposed an empirical relationship to fit the experimental data but did not include the tip-loss effect. This can be adjusted by multiplying the momentum component, $C_T = 4a(1-a)$, and a in Glauert's fit by F. However, this forms a discontinuity at $a = 0.4$ whenever F is less than one. A modified Glauert correction by Buhl [10] is used here that accounts for both the tip-loss effect and the discontinuity. It's implementation will be shown in the following section. Although the equations proposed by Glauert and Buhl approximately replicate the experimental data, they are not based on any physical rationalization of the flow behaviour and additional thrust occurring in the turbulent-wake state [65]. More accurate experimental data at high thrust is required which to base an accurate correction.

3.3.3 BEM Algorithm

The blade element and momentum theory equations have been introduced and it is now possible to describe the last step in the BEM algorithm. The axial and tangential induction factors are obtained by combining equation (3.23) with (3.30) and equation (3.24) with (3.31)

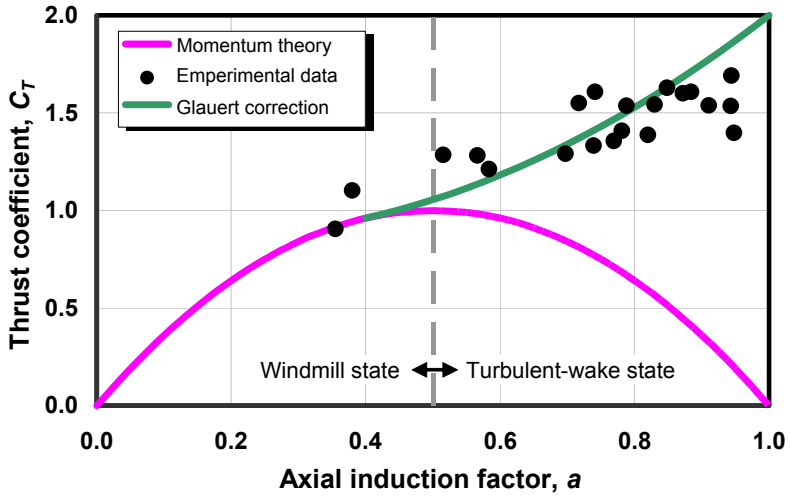

Figure 3.7: C_T as a function of a showing momentum theory and Glauert's empirical relationship when tip-loss effect is ignored. Modified from [10].

respectively:

$$a = \left(\frac{4F \sin^2 \phi}{\sigma C_n} + 1 \right)^{-1}, \tag{3.32}$$

$$a' = \left(\frac{4F \sin \phi \cos \phi}{\sigma C_t} - 1 \right)^{-1} \tag{3.33}$$

where the solidity σ, is a function of r and is defined by:

$$\sigma(r) = \frac{c(r)B}{2\pi r}. \tag{3.34}$$

Note that the modified Glauert correction:

$$a = \frac{18F - 20 - 3\sqrt{C_T(50 - 36F) + 12F(3F - 4)}}{36F - 50} \tag{3.35}$$

is applied instead of equation (3.32) when $C_T \geq 0.96F$, which is the equivalent of when $a \geq 0.4$. The thrust coefficient, C_T, is obtained by combining its definition (equation (3.10)) for a blade element:

$$C_T = \frac{dT}{\rho_{air} \pi V_o^2 dr} \tag{3.36}$$

with equation (3.23) from blade element theory that yields:

$$C_T = \frac{(1-a)^2 \sigma C_n}{\sin^2 \phi}. \tag{3.37}$$

Returning to equations (3.13) and (3.14), the induction factors a and a' are not known until equations (3.32), (3.33) and (3.35) are calculated. Therefore, a and a' in BEM must be solved iteratively until convergence is achieved. The BEM algorithm is summarized by the following 6 steps and can be executed simultaneously for all blade elements:

1. Set an initial guess of $a = 0$ and $a' = 0$;

2. Compute the flow angle ϕ, and hence the angle of attack α, using equations (3.13) and (3.14);

3. Interpolate the lift (C_l) and drag (C_d) coefficients from airfoil data tables using α and compute the normal (C_n) and tangential (C_t) force coefficients using equations (3.15) and (3.16);

4. Compute the tip-loss factor F, using equations (3.28) and (3.29), and the thrust coefficient C_T, using equation (3.37);

5. Compute a' using equation (3.33) and apply equation (3.32) or (3.35) depending on the value of C_T for a;

6. Check the values of a and a' with those from the previous iteration. If the tolerance level is met, terminate the algorithm, else return to step 2 and input the values of a and a' from step 5.

Once a and a' are obtained within a certain tolerance level or the maximum number of iterations pre-set by the user is reached, the thrust and power can be calculated from either the blade element or momentum theories. The blade element theory equations (3.23) and (3.24) are used here and normalized to give the differential power (dC_P) and thrust (dC_T) coefficients with respect to $\mu = r/R$:

$$dC_P = B\frac{(1-a)\lambda^2(1+a')}{\pi R \sin\phi\cos\phi}cC_t\mu^2 d\mu, \tag{3.38}$$

$$dC_T = B\frac{(1-a)^2}{\pi R \sin^2\phi} cC_n d\mu. \tag{3.39}$$

Equation (3.38) is obtained by combining equations (3.9), (3.24) and (3.27) for a blade element and similarly equation (3.39) by combining equations (3.23) and (3.36). The C_P and C_T for a rotor is then calculated by integrating from the hub radius r_{hub}/R, to 1. Recall that the BEM method involves a discretization by N and hence trapezoidal integration is used to numerically evaluate equations (3.40) and (3.41):

$$C_P = \int_{r_{hub}/R}^{1} B\frac{(1-a)\lambda^2(1+a')}{\pi R \sin\phi\cos\phi} cC_t\mu^2 d\mu, \tag{3.40}$$

$$C_T = \int_{r_{hub}/R}^{1} B\frac{(1-a)^2}{\pi R \sin^2\phi} cC_n d\mu. \tag{3.41}$$

3.4 Control and Regulation Strategy

Modern HAWTs are equipped with control or regulation systems to ensure the turbine operates safely within its design range. For example, at high wind speeds, the power produced by the aerodynamic torque (see dQ in equation (3.27)) may exceed the maximum limit for the generator. To prevent exceeding the generator limit, a control system can adjust the pitch angle of the blades or the rotor's rotational speed, ω. Control and regulation systems are also necessary in emergency situations. For instance, in case of a grid outage and high winds, the rotational speed of the rotor will accelerate dangerously due to the loss in generator torque. Unless a countermeasure is employed, the rotor's rotational speed will continue to increase leading to the destruction of the turbine.

Pitch and variable-speed control are not only used as safety mechanisms but also to optimize C_P in equation (1.5) at lower wind speeds. In addition, to maximize the amount of wind through the rotor, yaw control is used to ensure the rotor's rotation axis is aligned with the wind direction at all times. Wind-turbine yaw and varying wind directions, however, is not considered in this thesis. This section will describe how the BEM method can be used

to predict the power curve for a pitch-regulated and variable-speed HAWT. Pitch regulation will be discussed first followed by variable-speed operation.

3.4.1 Pitch Regulation

By actively changing the pitch angle of the blade θ, as shown in Figure 3.3 and equation (3.14), the angle of attack α, can be adjusted to control the lift and drag forces, and consequently the power output. The adjustments can be achieved in practice by fitting each blade with a motor and rotating each blade independently. Two pitch-regulation methods to reduce the power output include increasing the angle of attack until the blades begin to stall (*pitch-to-stall*) or decreasing the angle of attack such that the leading edge of the blade is pointing towards the wind direction (*pitch-to-feather*). The former method is advantageous in that the necessary angle to pitch the blade is smaller in comparison with the later. However, pitching to stall is not as precise and is accompanied by severe aerodynamic loadings. For these reasons, among others, most modern HAWTs pitch the blades towards feather in high winds. Pitch-to-stall and pitch-to-feather can readily be observed by referring to Figure 3.4. When α exceeds approximately 15.3°, the airfoil (or the blade element) begins to stall and the drag coefficient becomes large. Conversely, when pitching to feather, α becomes small and the lift and drag coefficients approach zero. Both methods reduce the tangential force coefficient C_t, in equation (3.16) that results in lower torque (equation (3.24)) and power (equation (3.27)).

The power curve for a fixed-speed HAWT with and without pitch regulation is shown in Figure 3.8. From this figure, the turbine that is kept at $\theta = 0°$ pitch far exceeds its rated power (P_{rated}) of 60 kW and thus also its generator limit. When the same turbine with pitch regulation reaches 60 kW at the rated wind speed of 12 m/s, P_{rated} is achieved for all higher wind speeds by pitching the blades to feather. Instead of pitch regulation, the 0° blade pitch could be readjusted such that the peak power lies below the P_{rated} line. HAWTs that implement this approach are called *stall regulated* as opposed to pitch regulated. To

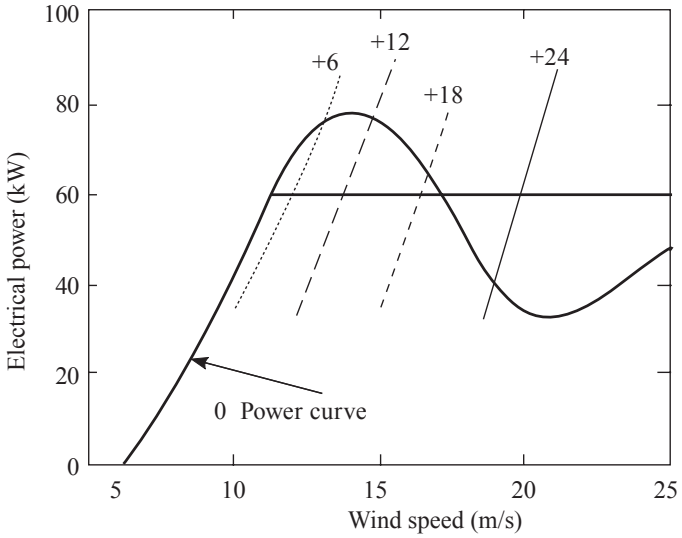

Figure 3.8: Fixed-speed HAWT with and without pitching to feather. Modified from [6]. ©2001 John Wiley & Sons Ltd.

decrease α in pitch-regulated HAWTs, θ must increase per equation (3.14). The increase in θ is shown in Figure 3.8 where the pitch angle increases from 6° to 24°. It is also possible to increase the power output below the rated wind speed using pitch adjustments, however this becomes unnecessary for pitch-regulated HAWTs that also feature variable-speed operation.

3.4.2 Variable Speed

As discussed in section 1.3, the power coefficient C_P, depends on the tip speed ratio λ, and the pitch θ, for pitch-regulated wind turbines for both constant and variable speed. By implementing pitch regulation and variable speed, it is possible to run the turbine at the optimum C_P ($C_{P,opt}$) for a range of wind speeds at one λ and θ (λ_{opt} and θ_{opt}). Figure 3.9 displays the power as a function of the rotational speed for a fixed-pitch wind turbine with and without variable speed. Variable-speed operation is represented by the thick curved line that intersects the point of maximum possible power at each wind speed, V_o. Each intersection corresponds to $C_{P,opt}$ at a constant $\lambda_{opt} = \omega R/V_o$ where ω increases proportionally with V_o. In contrast, fixed-speed operation is represented by the thin vertical line and it is easily

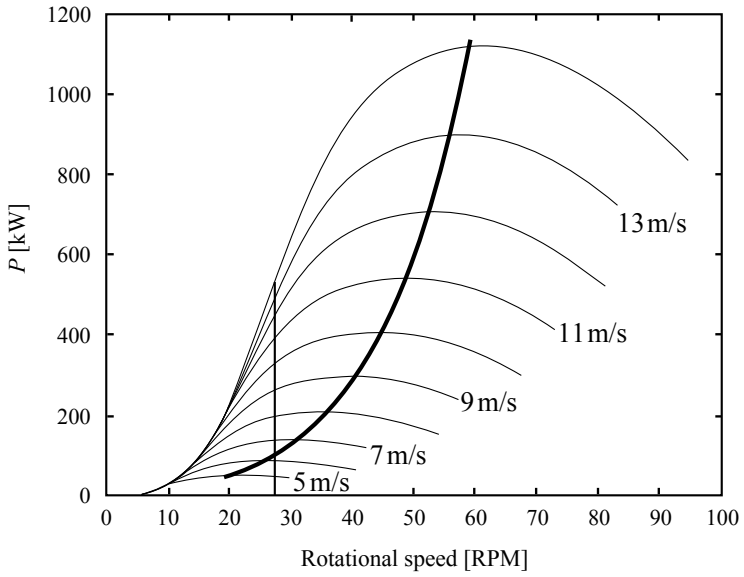

Figure 3.9: Fixed (thin vertical line) vs. variable (thick curved line) speed operation. Reproduced from [8].

observed that maximum power is not achieved at each V_o.

If $C_P = C_{P,opt} = C_P(\lambda_{opt}, \theta_{opt})$ for a range of V_o, then equation (1.3) can be combined with $P = \omega Q$ to solve for the torque, Q_{opt}:

$$Q_{opt} = \frac{1}{2}\rho_{air}\frac{R^5 \pi C_P(\lambda_{opt}, \theta_{opt})}{\lambda_{opt}^3}\omega^2 = K_{opt}\omega^2 \tag{3.42}$$

where K_{opt} is a constant. Combining equation (3.42) with $P = \omega Q$ once again gives an expression for the optimum power:

$$P_{opt} = K_{opt}\omega^3. \tag{3.43}$$

The power for variable-speed operation (curved line) shown in Figure 3.9 is given by equation (3.43) and will continue to increase with ω^3 until either the maximum tip speed (ωR), ω, or P_{rated} is reached. The limit on tip speed is due to noise emission, since wind turbine generated noise is well correlated with ωR (although there are other factors such as tip and airfoil shapes) [72]. If the limit on ωR is reached before the P_{rated} mark for increasing V_o, ω becomes constant and the power is maximized using pitch adjustments. Once P_{rated} is attained, pitch adjustments are no longer used to maximize the power but rather to maintain

P_{rated} for all higher values of V_o as shown in Figure 3.8.

3.4.3 Pitch-Regulated and Variable-Speed HAWT Control Regions

To help illustrate sections 3.4.1 and 3.4.2, Figure 3.10 displays the power and thrust curves as well as the pitch and RPM schedules for a pitch-regulated and variable-speed wind turbine. Three distinct control regions, I, II and III are shown in Figure 3.10. Region I is the variable-speed region where equation (3.43) applies. As shown in Figure 3.10(d), the RPM increases proportionally with V_o to maintain a constant λ_{opt} and $C_P(\lambda_{opt}, \theta_{opt})$. The constant $C_P(\lambda_{opt}, \theta_{opt})$ is also reflected in Figure 3.10(c), where $\theta = \theta_{opt}$. In region II, the RPM becomes constant due to the tip-speed limit and pitch adjustments are used to optimize the power. When optimizing for power in region II, the pitch will typically decrease to achieve an increase in C_t (see section 3.4.1). However, it is common practice to constrain the pitch to be greater than or equal to θ_{opt}. This simplifies the pitch scheduling and also reduces the adverse thrust. As shown in Figure 3.10(b), the highest thrust occurs between regions II and III, and would increase further if the pitch constraint were removed. The reduction in thrust by imposing the pitch constraint is considered more beneficial than the potential gain in power. In region III, P_{rated} is reached and remains constant as shown in Figure 3.10(a). The constant P_{rated} is the result of pitch regulation, which pitches the blades towards feather as shown in Figure 3.10(c). Also in region III, the thrust decreases and the RPM remains at its maximum allowable value.

To obtain the performance curves in Figure 3.10 using the BEM method, it is necessary to compute C_P and C_T through equations (3.40) and (3.41) for a range of λ and θ that encompasses all possible operating conditions typical to pitch-regulated and variable-speed HAWTs. Surface plots of C_P and C_T as a function of λ and θ are displayed in Figures 3.11 and 3.13 respectively. As shown for large values of λ and θ in Figure 3.11, a negative value of C_P indicates that the rotor will not turn and will act as a brake [73]. Following the descriptions in sections 3.4.1 and 3.4.2, the performance curves are then extracted from the

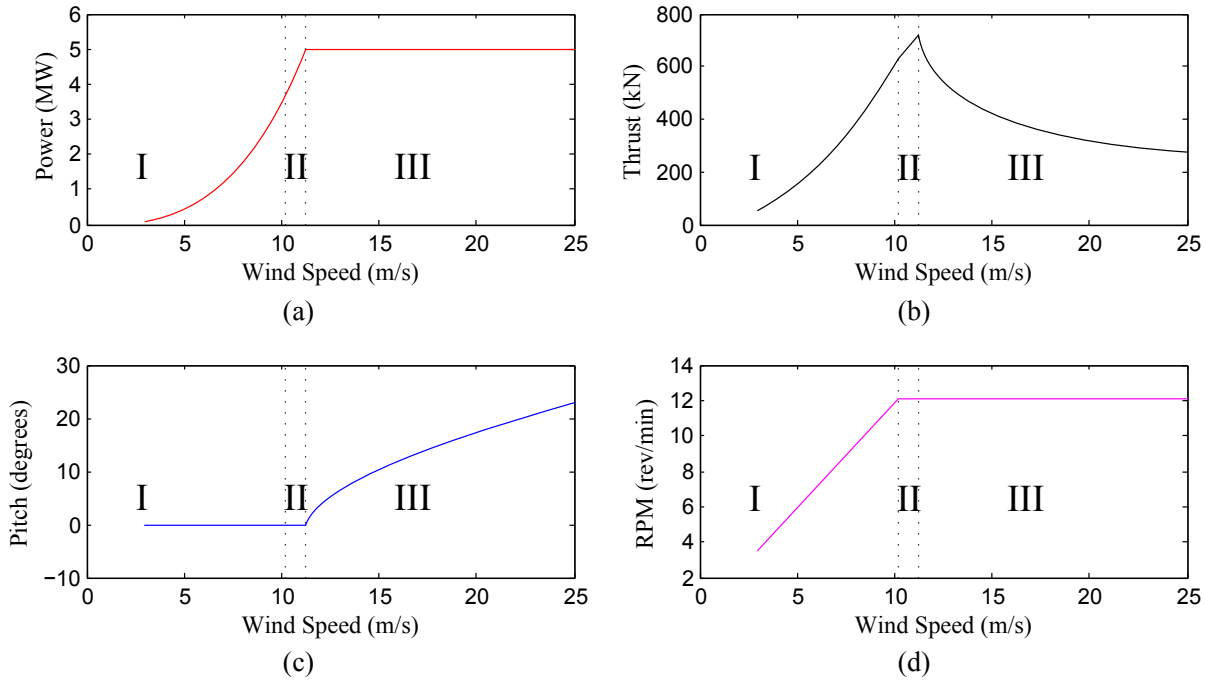

Figure 3.10: Power (a) and thrust (b) curves for a typical pitch-regulated (c) and variable-speed (d) HAWT.

surface plots, which lie in the positive region of C_P and C_T as illustrated in Figures 3.12 and 3.14 respectively.

3.5 Verification and Experimental Validation

3.5.1 Verification with WT_Perf

A BEM code was developed following the description given in section 3.3 and verified with WT_Perf by the National Wind Technology Center (NWTC) [74]. WT_Perf is a descendent of the PROP code written in FORTRAN, which is also based on the BEM method. The Advanced Wind Turbine (AWT-27) with a 27 m rotor diameter is selected from the WT_Perf test archive as the baseline turbine for comparing C_P results. C_T is not considered because WT_Perf does not provide a readily available output for this coefficient. Furthermore, differences in C_P as a function of λ and θ are studied rather than differences in the power and thrust curves (as shown in Figure 3.10) because WT_Perf does not have a pitch and RPM

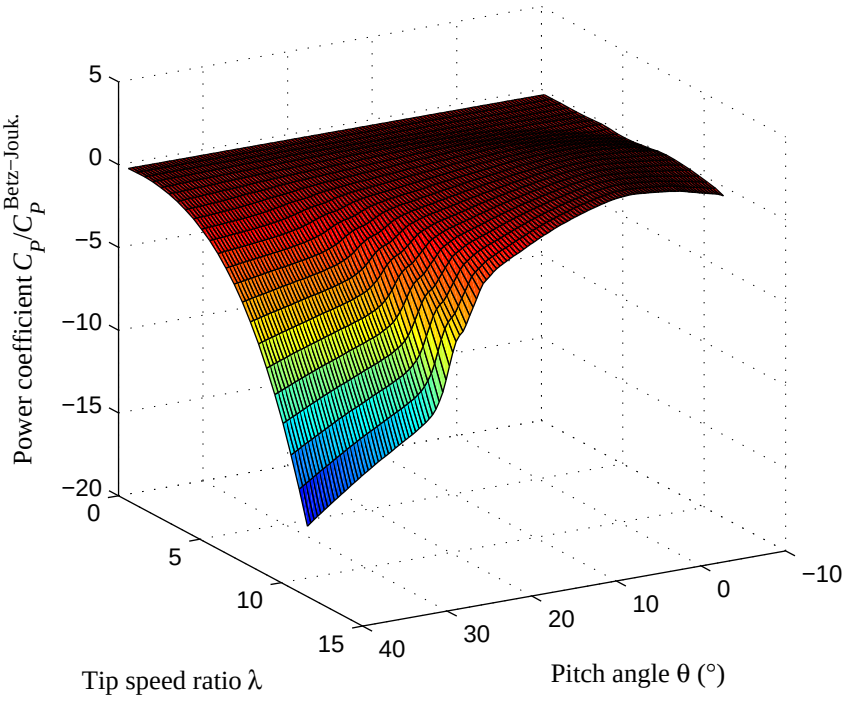

Figure 3.11: Power coefficient C_P, as a function of λ and θ for a typical HAWT.

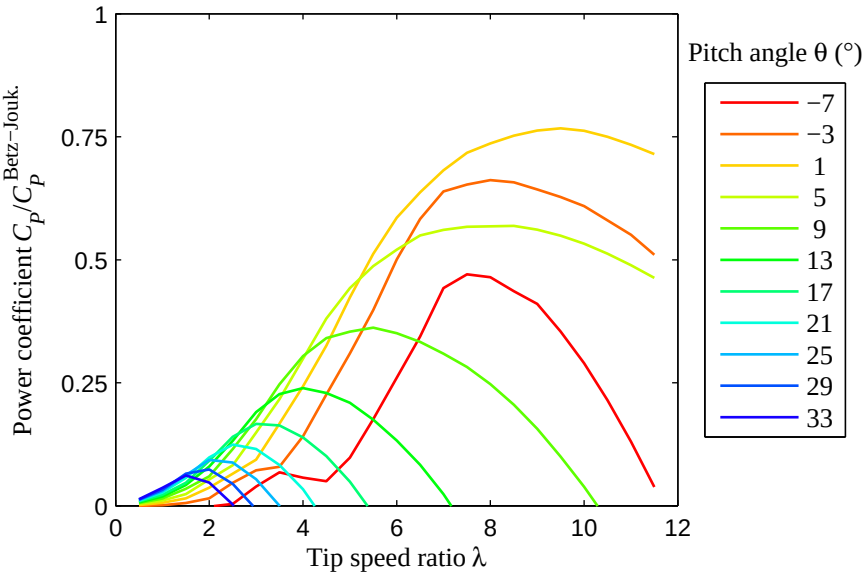

Figure 3.12: 2D plot of power coefficient $C_P(+)$, as a function of λ and θ for a typical HAWT.

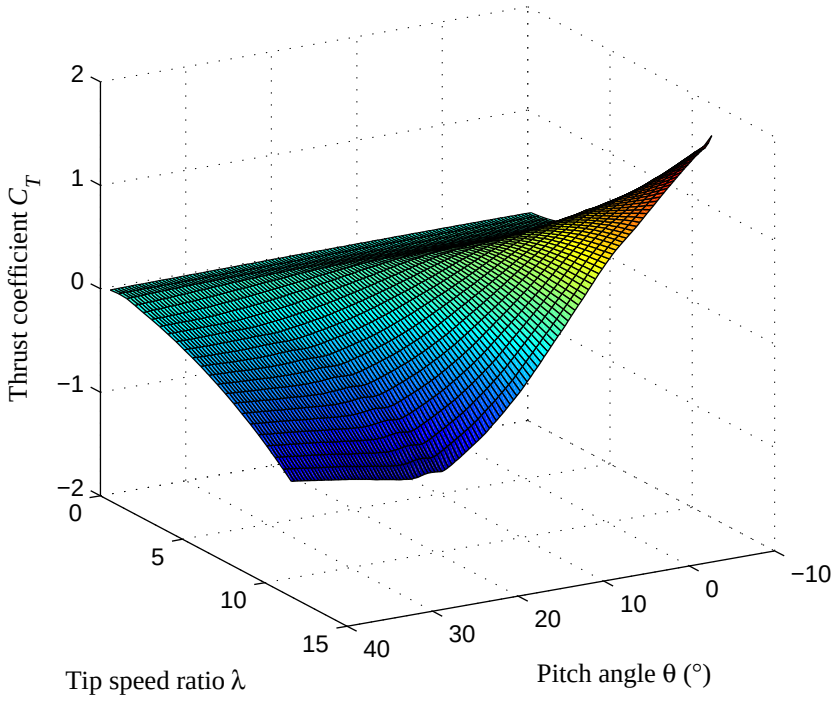

Figure 3.13: Thrust coefficient C_T, as a function of λ and θ for a typical HAWT.

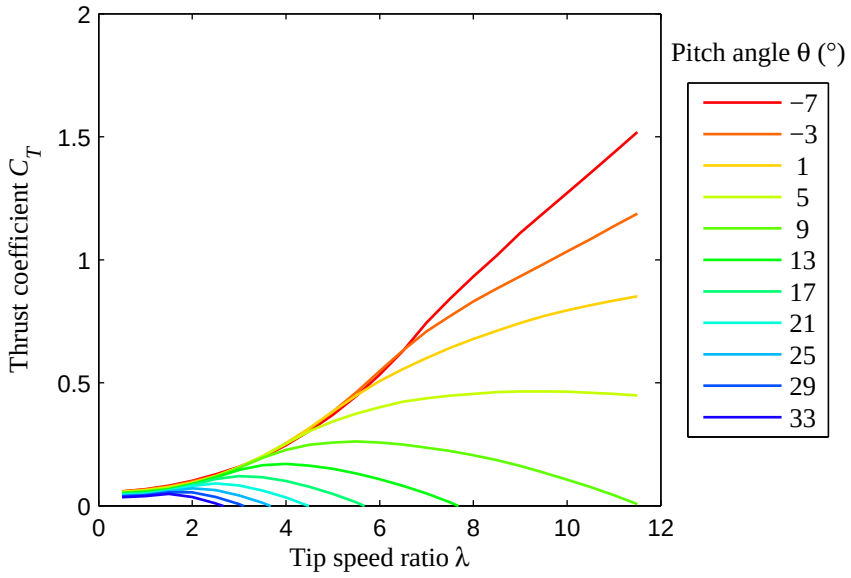

Figure 3.14: 2D plot of thrust coefficient $C_T(+)$, as a function of λ and θ for a typical HAWT.

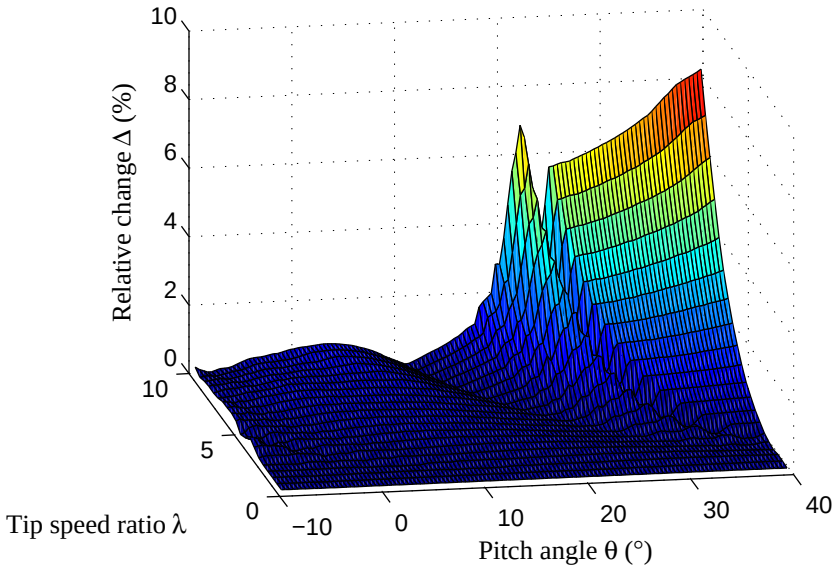

Figure 3.15: Relative change Δ, for C_P of AWT-27.

scheduler. The relative change Δ, is calculated using:

$$\Delta = \left| \frac{C_P - C_P^{\text{WT\_Perf}}}{C_P^{\text{Betz-Jouk.}}} \right| 100\% \tag{3.44}$$

where $C_P^{\text{Betz-Jouk.}} = 16/27$. The results are shown in Figure 3.15 for λ from 0.5 to 10 and θ from -10° to 40°. For λ beyond 10, WT_Perf does not converge for some values of θ and hence is not computed.

The minimum and maximum values of Δ are $6.4 \times 10^{-5}\%$ and 8.28% respectively. As shown in Figure 3.15, Δ becomes large for high values of λ and θ. This occurs because the absolute magnitude of C_P increases significantly in this region as shown in Figure 3.11, which results in a large difference between C_P and $C_P^{\text{WT\_Perf}}$ in the numerator of equation (3.44). Consequently, the reference value of $C_P^{\text{Betz-Jouk.}}$ in the denominator becomes inappropriate (i.e. too small), yielding a large Δ. If $C_P^{\text{WT\_Perf}}$ is used as the reference value instead of $C_P^{\text{Betz-Jouk.}}$ in equation (3.44), then $\Delta < 1\%$ would be the result. However, $C_P^{\text{WT\_Perf}}$ was not chosen as the reference value because Δ approaches infinity when $C_P^{\text{WT\_Perf}}$ is near zero. Nevertheless, pitch-regulated and variable-speed HAWTs rarely operate within this range because of the negative C_P and can therefore be neglected in the blade optimization.

Besides the propagation and accumulation of small numerical inconsistencies throughout the BEM algorithms, the source of discrepancy between the two codes may also be the result of the different methods implemented for solving the induction factors. The developed BEM code uses fixed-point iteration with relaxation factors, while WT_Perf employs a combination of the Newton-Raphson and bisection methods. An attempt was made to incorporate the Newton-Raphson and bisection methods for the developed BEM code, however the fixed-point approach (with relaxation factors) was found to be easier to implement for the optimization considered in this thesis. For details regarding the fixed-point and Newton-Raphson methods, refer to [75]. As shown in Figure 3.16, the values of C_P computed from the developed BEM code and WT_Perf are almost identical. Therefore, the developed BEM code is assumed to be sufficiently accurate for the remainder of this thesis.

3.5.2 Validation with NREL UAE Measurements

This section describes the accuracy of the BEM method with respect to measurements in a controlled experimental setting. First, potential corrections needed in the BEM method for 3D effects and its relationship with aerodynamic stall and rotation will be discussed. Then, the results obtained from BEM with and without the 3D corrections will be compared to experimental measurements for a stall-regulated wind turbine. The BEM code developed in this thesis does not include 3D corrections for simplicity and is deemed to have less of an effect for pitch-regulated wind turbines. Furthermore, as will be shown in section 3.5.2.2, discrepancies still occur despite the corrections. Determining and implementing the most appropriate 3D correction for BEM is beyond the scope of this thesis. Nonetheless, the effects of 3D flow behaviour should be discussed.

3.5.2.1 Three-Dimensional and Rotational Effects

As discussed in section 3.1 for BET, each blade element on the blade is treated aerodynamically as an airfoil that acts independently from other blade elements. In addition, the radial

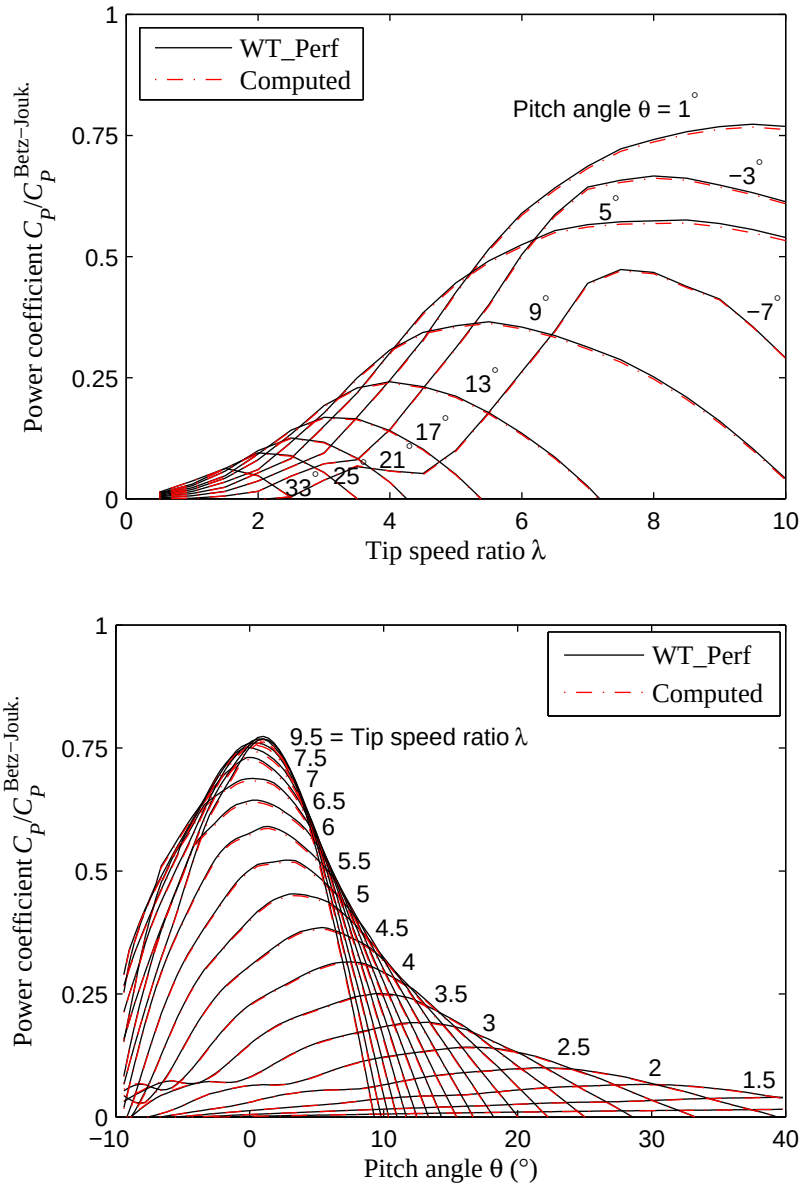

Figure 3.16: 2D plots of the computed power coefficient C_P, as a function of λ and θ vs. from WT_Perf for AWT-27.

component of the flow along the blade is ignored. Consequently, BEM does not take 3D effects into account. While a wind-turbine rotor is rotating, a component of the flow moves outwards from the blade root to the blade tip due to centrifugal and Coriolis forces. This particular phenomenon leads to *stall delay* and predominantly influences the aerodynamics near the blade root. In terms of blade performance, an augmentation in the lift (especially) and drag is observed. As a result, the performance of a wind turbine benefits from stall delay. Although stall delay may appear logical, it is still far from being completely understood. The inclusion of the stall-delay effect in BEM can be approximated by adjusting the 2D airfoil data near the aerodynamic stall region.

Wind-turbine researchers have developed numerous different methods for adjusting airfoil data to include stall delay. One method is by Chaviaropoulos and Hansen [76] and is based on a semi-empirical correction law that is derived from a quasi-3D Navier-Stokes model. The quasi-3D model is a simplification of the 3D incompressible Navier-Stokes equations. The semi-empirical relations are given by:

$$C_{l,\mathrm{3D}} = C_{l,\mathrm{2D}} + h_1(c/r)^{h_2}\cos^{h_3}(\beta)[C_{l,\mathrm{INVISICID}} - C_{l,\mathrm{2D}}], \tag{3.45}$$

$$C_{d,\mathrm{3D}} = C_{d,\mathrm{2D}} + h_1(c/r)^{h_2}\cos^{h_3}(\beta)[C_{d,\mathrm{2D}} - C_{d,\mathrm{2D(MIN)}}] \tag{3.46}$$

where C_l and C_d are the lift and drag coefficients respectively. For each blade element, the variable c is the chord length, r is the radius from the centre of rotation, and β is the twist. The three constants h_1, h_2, and h_3 are calibrated based on a computational data base, and they depend on the airfoil data table used. For the stall-regulated NREL UAE wind turbine described in section 3.5.2.2, h_1, h_2, and h_3 are equal to 2.2, 1.3, and 4 respectively. From equations (3.45) and (3.46), the pronounced influence of stall delay near the blade root is indicated by the c/r term. At the root section, r is small and c is large, giving a large value for c/r and hence an increase in $C_{l,\mathrm{3D}}$ and $C_{d,\mathrm{3D}}$. The effect of the correction on the lift and drag coefficients is shown in Figure 3.17 for the S809 airfoil at 33% of the blade span.

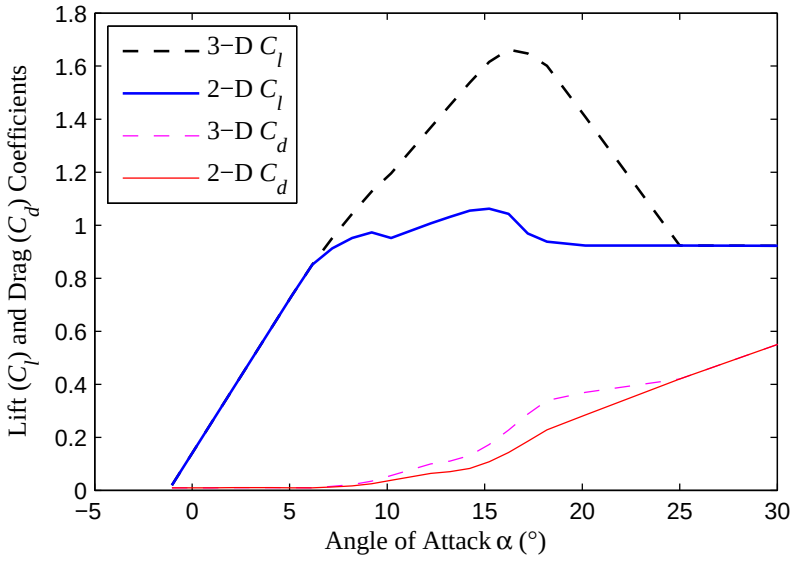

Figure 3.17: 2D- versus 3D-corrected S809 airfoil data at 33% of the blade span.

3.5.2.2 NREL UAE Measurements

The semi-empirical model developed by Chaviaropoulos and Hansen has been incorporated in BEM and renamed ROTABEM. ROTABEM was then used to model the aerodynamic performance of an instrumented, 2-bladed and stall-regulated wind turbine constructed by NREL. The NREL wind turbine has a 10 m rotor diameter and was placed in the National Full-Scale Aerodynamics Complex located in the NASA Ames Research Center for experimental testing. This particular experimental test is known as the NREL Unsteady Aerodynamics Experiment (UAE) in the NASA-Ames wind tunnel or alternatively, NREL UAE Phase VI. A blind comparison was conducted where numerous researchers (e.g. Chaviaropoulos and Hansen) attempted to predict the performance of the NREL turbine using their own modeling tools without knowing the experimental results. The results from the NREL UAE is compared to the BEM output in this section.

ROTABEM has been replicated in MATLAB by incorporating equations (3.45) and (3.46) with the BEM code as described in section 3.3, and replacing the correction by Buhl with the one used by Chaviaropoulos and Hansen, the unmodified Glauert correction. The necessary instructions, airfoil data, and blade dimensions were taken directly from Chaviaropoulos and

Hansen's documentation of their code in the *Participant's documentation* file available on the NREL Ames test website [9]. The replication was required to study the ROTABEM output with and without the 3D corrections. Furthermore, NREL kept all modeler predictions anonymous and it was unknown which of the results belonged to Chaviaropoulos and Hansen's ROTABEM.

Figure 3.18 displays the results for the particular test case consisting of a steady wind at varying speeds with the NREL turbine in an upwind configuration and 0° yaw. Four torque curves are shown of which two are acquired by digitizing Figure 8 in [11]. The digitized data consists of the experimental measurements obtained from the instrumentation mounted on the NREL wind turbine (black curve) and the output from ROTABEM (purple curve). The remaining two curves are from the replicated ROTABEM code with (blue curve) and without (red curve) the 3D corrections. As shown in Figure 3.18, a nearly identical match is achieved between ROTABEM developed by Chaviaropoulos and Hansen, and the replicated version. However, despite the 3D corrections, discrepancies exist between ROTABEM and the measured data. As one might expect, according to stall-delay theory, the BEM code without the 3D correction under predicts the torque for all wind speeds. Conversely, ROTABEM over predicts the torque from 10 m/s to 13 m/s but also under predicts the torque from 15 m/s to 25 m/s. Based on this analysis, it is not evident how current 3D-correction models may significantly improve the accuracy of BEM, and is therefore not included in this thesis. A similar conclusion was also found by Breton, Coton and Moe [77], where a total of six different 3D-correction models were investigated and in general, over predicted the loads on the turbine.

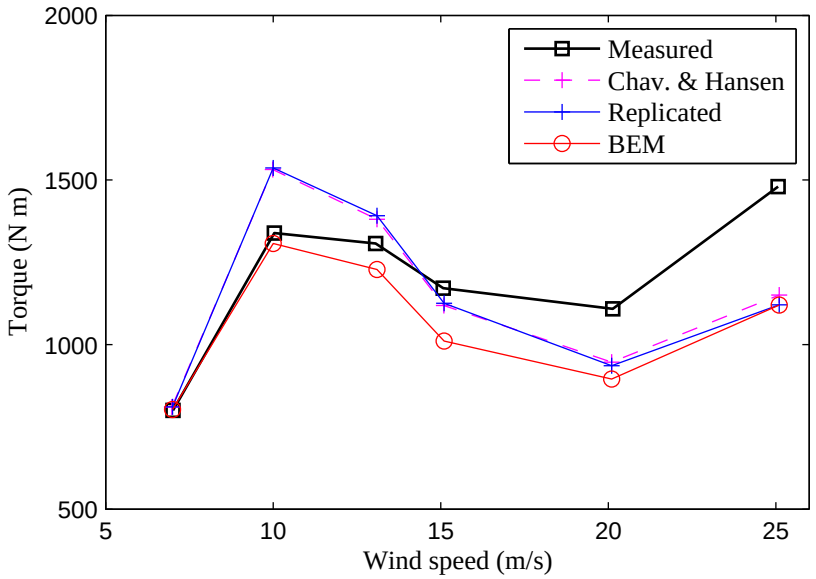

Figure 3.18: Comparison of torque versus wind speed between measurements and BEM with (Replicated) and without (BEM) 3D corrections, for upwind, 0° yaw NREL turbine. Measured data, and Chaviaropoulos and Hansen results digitized from [11].

Chapter 4

STRUCTURAL MODEL

4.1 Introduction

The structural model consists of a cross-sectional model and beam theory. Similarly as in the BEM method, the blade is divided into N blade elements where the cross-section of each element is analyzed structurally. Figure 4.1 illustrates a typical wind-turbine blade cross-section. To perform the structural analysis, the mechanical properties of each material in the cross-section are assumed to be isotropic. Consequently, a mechanical property such as the elastic modulus E, is independent of the direction of loading considered. The isotropic assumption allows E to be simply multiplied with the cross-sectional area A, the first moment of area S, and second moment of inertia I, to obtain the stiffness EA, ES and EI for each blade element. In reality, most wind-turbine blades are fabricated from fibre-reinforced plastics (FRP), whose properties do depend on the direction of loading and are said to be anisotropic. The fibre orientation in FRPs provides stiffness to the blade in the directions where the loads are large, and less stiffness where it is not needed. In addition to its superior stiffness properties, FRPs have high strength-to-weight ratios making them ideal for wind-turbine blades. The calculation of cross-sectional properties including anisotropic effects, however, is complex and as a result the cross-sectional model presented here is restricted to the simpler isotropic case. To estimate the structural behaviour of a wind-turbine blade using beam theory, the cross-sectional properties such as the bending stiffness EI, are required as input.

By definition, a beam is a structure having one of its dimensions much larger than the other two [78]. Beams are commonly used in civil and mechanical engineering with the main purpose of supporting loads. For a wind turbine, the blade's inner core is designed

Figure 4.1: Photo of an actual wind-turbine blade cross-section taken at NREL in Golden, CO, USA. Credit: Green Career Central (http://www.greencareercentral.com).

similarly to that of a beam to support the aerodynamic loads produced by the blade's outer aerodynamic shape. In contrast, the blade's outer aerodynamic shape is usually designed as a thin shell that contributes minimally to the blade structural strength. Because of the resemblance, beam theory can be used to model the structural behaviour of a wind-turbine blade.

Beam theory allows designers to perform simple structural analyses. Alternatively, tools that implement the finite element method can also be used but rely on increased computing costs, and are more suitable for detailed stress and displacement analysis of complex structures. A number of beam theories exist in the literature based on different assumptions and levels of accuracy. Among them, Euler-Bernoulli beam theory is one of the simplest and most widely used. The Euler-Bernoulli assumptions are as follows [78]:

1. The cross-section is infinitely rigid in its own plane;

2. The cross-section remains plane after deformation;

3. The cross-section remains normal to the deformed axis of the beam.

These assumptions are typically valid for thin cross-sections and small deformations. For thick structures and large deflections, the assumptions are not valid because shear deformation and cross-sectional warping occurs [79]. To account for some of the Euler-Bernoulli assumptions, a higher order Timoshenko beam model can be used instead. In Timoshenko beam theory, cross-sections still remain plane but are no longer normal to the deformed axis of the beam (shear deformation). The Euler-Bernoulli beam model is implemented here because of its simpler implementation with the cross-sectional model in the preliminary design optimization of wind-turbine blades. Consequently, it is assumed that blade deformations are small in comparison with the blade length and shear effects are negligible.

4.2 Cross-Sectional Model

4.2.1 Cross-Sectional Layup

The cross-section of a wind-turbine blade is a complex shape composed of many parts and different materials. There are several designs of the layup regarding the number and placement of skins, shear webs, leading- and trailing-edge reinforcements, and spar caps, in addition to the dimensions and materials selected for each (see Figure 4.2 for definitions of terms). A layup common to many blade designs is the box type as shown in Figure 4.2, and is selected as the baseline for the cross-sectional model. In the box-type layup, the spar caps are glued in-between the two shear webs forming a box within the upper and lower surfaces. Although box-type layups may vary from one wind-turbine blade to another, the one considered here includes a shell composed of a gelcoat (for the surface) and two skins, two shear webs, fore and aft panels, and two spar caps of equal thickness. Leading- and trailing-edge reinforcements, which mainly provide edgewise stiffness (EI_y in section 4.2.4), are not included. Approximate dimensions for the gelcoat, skins, shear webs, and panels are obtained from [80]. The thickness distribution of the spar caps between the blade root and tip is left as an optimization variable, and is discussed in section 4.4. The materials selected for the

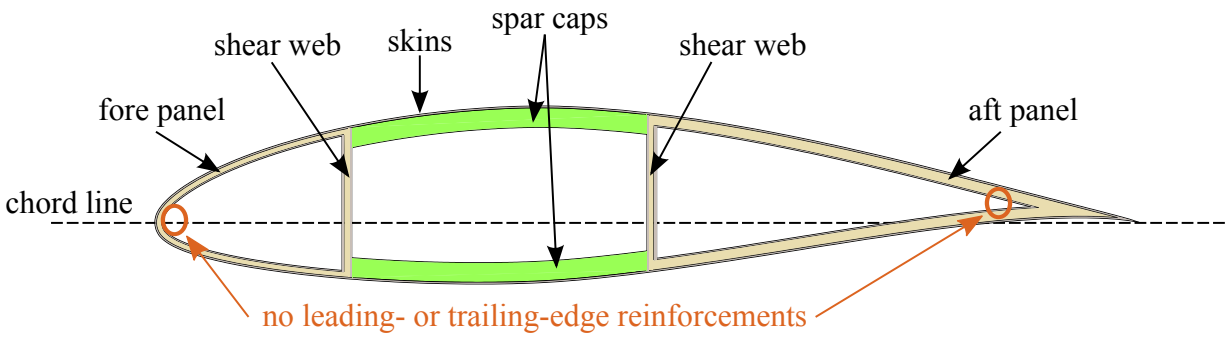

Figure 4.2: Typical box-type layup at a wind-turbine blade cross-section.

various components of the cross-section are from [2] and summarized in Table 4.1 with their mechanical properties. Since materials are treated in an isotropic manner as mentioned in section 4.1, the more crucial flapwise component from [2] is chosen for the elastic modulus E. If desired, the user may input their own dimensions and material properties, as well as the location of the shear webs in the cross-sectional model. Here, the shear webs are located at $0.2c$ and $0.5c$, where c is the chord length. However, to further describe this model, materials from [2] will be used as example.

Table 4.1: Material properties used in cross-sectional model [2].

Property	[0°] A260	[±45°][0°] CDB340	Rand. Mat	Balsa	Gel Coat
Elastic Mod., E (GPa)	31.0	24.2	9.65	2.07	3.44
Density, ρ (kg/m^3)	1700	1700	1670	144	1230

The skins and spar caps are fabricated from an epoxy matrix reinforced with E-glass fibres (i.e. fibreglass). The spar cap is composed of uniaxial ([0°]) A260 fabric, where the fibres are oriented along the blade ([0°]) giving maximum stiffness in that direction. The two skins in the shell consist of a random mat and triaxial ([±45°][0°]) fibreglass laminate designated CDB340. For the shear webs and panels, balsa is used with a layer of CDB340 on each side. This forms a sandwich construction of CDB340 separated by a balsa core. To facilitate the integration across the shear-web and panel coordinates (see section 4.2.2), a continuous piece of balsa between the shear web and panel is assumed.

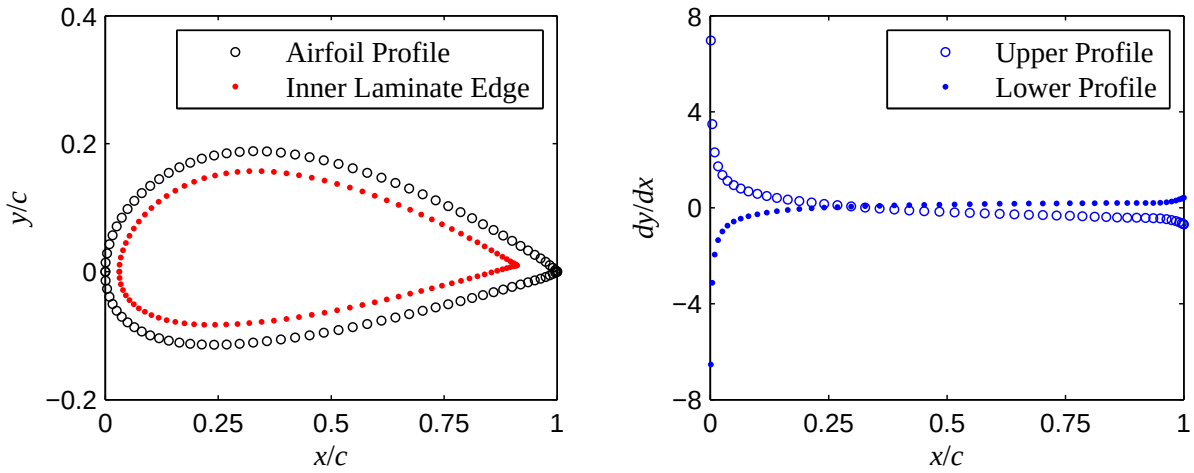

Figure 4.3: Cross-section showing laminate thickness calculation (left) using upper and lower airfoil profile slopes (right).

4.2.2 Laminate Coordinates Calculation

The cross-sectional model begins by importing the x- and y-airfoil profile coordinates corresponding to each blade element from the blade root to tip. To obtain a laminate of constant thickness all around the inner airfoil's contour (see left of Figure 4.3), the slope across the coordinates of the laminate must match that of the airfoil profile. Therefore, the subsequent step is to compute the slope about the airfoil's upper and lower profile using finite differences as shown on the right of Figure 4.3. Using the slope normal to that of the airfoil profile and a given thickness, the coordinates of the laminate are computed. This procedure is extended to the multi-laminated cross-section in Figure 4.2 and scaled in proportion to the blade element chord, as illustrated in Figure 4.4.

4.2.3 Green's Theorem

Green's theorem is:

$$\iint_S \left(\frac{\partial N}{\partial x} - \frac{\partial M}{\partial y} \right) dxdy = \oint_L Mdx + Ndy, \tag{4.1}$$

which states that the surface integral over a planar region A_s, can be converted to a line integral along the boundary of A_s. Applying Green's theorem, the surface integral equations

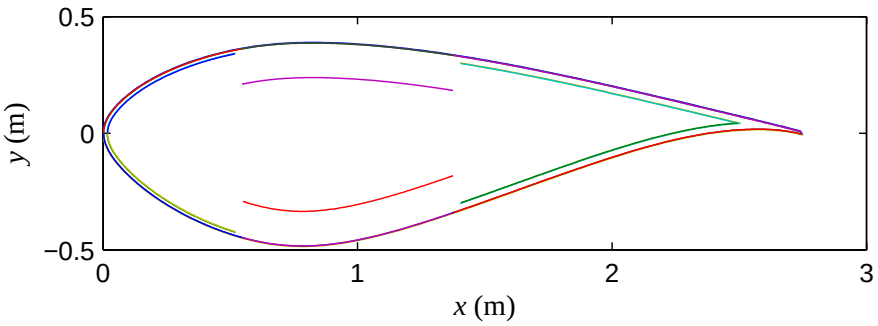

Figure 4.4: A multi-laminated cross-section scaled in proportion to the blade element chord.

for the area (A), first moment of area (S), and second moment of inertia (I) are converted to line integral equations, as shown by:

$$A = \iint_{A_s} dxdy = -\frac{1}{2}\oint_L y\,dx - x\,dy, \tag{4.2}$$

$$S_x = \iint_{A_s} x\,dxdy = \frac{1}{2}\oint_L x^2\,dy, \tag{4.3}$$

$$S_y = \iint_{A_s} y\,dxdy = -\frac{1}{2}\oint_L y^2\,dx, \tag{4.4}$$

$$I_x = \iint_{A_s} x^2\,dxdy = \frac{1}{3}\oint_L x^3\,dy, \tag{4.5}$$

$$I_y = \iint_{A_s} y^2\,dxdy = -\frac{1}{3}\oint_L y^3\,dx, \tag{4.6}$$

$$I_{xy} = \iint_{A_s} xy\,dxdy = -\frac{1}{4}\oint_L xy^2\,dx - x^2y\,dy. \tag{4.7}$$

The conversion of a surface to a line integral allows the geometrical properties A, S_x, S_y, I_x, I_y and I_{xy} for each laminate in a multi-laminated cross-section to be evaluated by simply integrating from one coordinate to the next.

4.2.4 Calculation of Cross-Sectional Properties

Before calculating the cross-sectional properties, definitions must be outlined. Following the reference coordinate system shown on Figure 4.5, the definitions are as follows [8]:

- Linear mass $\rho A = \iint\limits_{A_s} \rho(x,y)\,dxdy$;
- Longitudinal stiffness $EA = \iint\limits_{A_s} E(x,y)\,dxdy$;
- Moment of stiffness about the x-axis $ES_x = \iint\limits_{A_s} E(x,y)y\,dxdy$;
- Moment of stiffness about the y-axis $ES_y = \iint\limits_{A_s} E(x,y)x\,dxdy$;
- Bending stiffness about the x-axis $EI_x = \iint\limits_{A_s} E(x,y)y^2\,dxdy$;
- Bending stiffness about the y-axis $EI_y = \iint\limits_{A_s} E(x,y)x^2\,dxdy$;
- Moment of centrifugal stiffness $EI_{xy} = \iint\limits_{A_s} E(x,y)xy\,dxdy$.

For homogeneous and isotropic materials, ρ and E are constants and simply multiplied with equations (4.2) to (4.7) to obtain the above-mentioned cross-sectional properties.

The weighting method as described in [81] is used to extract the effective cross-sectional properties for each blade element. First, the equivalent elastic modulus of the shell E^{Shell}, is calculated by using the thickness τ, of the shell's constituents as weights:

$$E^{\text{Shell}} = \frac{E_{\text{gelcoat}}\tau_{\text{gelcoat}} + E_{\text{random mat}}\tau_{\text{random mat}} + E_{\text{CDB340}}\tau_{\text{CDB340}}}{\tau_{\text{gelcoat}} + \tau_{\text{random mat}} + \tau_{\text{CDB340}}}. \tag{4.8}$$

A similar approach is performed to obtain the equivalent density of the shell, ρ^{Shell}. The linear mass for the shell, spar cap, shear webs, and panels are then computed and aggregated to obtain the linear mass of a blade element m:

$$m = [\rho A]^{\text{Shell}} + [\rho A]^{\text{Spar Caps}} + \sum^{\text{num. layers}} [\rho A]^{\text{Webs/Panels}}_{layer}. \tag{4.9}$$

Similarly, the effective stiffness quantities are obtained as follows:

$$EA_{total} = [EA]^{\text{Shell}} + [EA]^{\text{Spar Caps}} + \sum^{\text{num. layers}} [EA]^{\text{Webs/Panels}}_{layer}, \tag{4.10}$$

$$ES_{x,total} = [ES_x]^{\text{Shell}} + [ES_x]^{\text{Spar Caps}} + \sum^{\text{num. layers}} [ES_x]^{\text{Webs/Panels}}_{layer}, \tag{4.11}$$

$$ES_{y,total} = [ES_y]^{\text{Shell}} + [ES_y]^{\text{Spar Caps}} + \sum^{\text{num. layers}} [ES_y]^{\text{Webs/Panels}}_{layer}, \tag{4.12}$$

$$EI_{x,total} = [EI_x]^{\text{Shell}} + [EI_x]^{\text{Spar Caps}} + \sum^{\text{num. layers}} [EI_x]^{\text{Webs/Panels}}_{layer}, \tag{4.13}$$

$$EI_{y,total} = [EI_y]^{\text{Shell}} + [EI_y]^{\text{Spar Caps}} + \sum^{\text{num. layers}} [EI_y]^{\text{Webs/Panels}}_{layer}, \tag{4.14}$$

$$EI_{xy,total} = [EI_{xy}]^{\text{Shell}} + [EI_{xy}]^{\text{Spar Caps}} + \sum^{\text{num. layers}} [EI_{xy}]^{\text{Webs/Panels}}_{layer}. \tag{4.15}$$

To calculate the strains and deflections using Euler-Bernoulli beam theory as explained in section 4.3, the bending stiffness about the principal axes (EI_1 and EI_2), where the axes have its origin in the point of elasticity (PE), are required as input. The PE is defined as the point where a normal force $N_{z,norm}$ (in/out of the x-y plane), will not give rise to a bending of the beam. The procedure given by Hansen [8] is used here to determine EI_1 and EI_2. First, the PE is calculated in the x-y reference frame as follows:

$$x_{\text{PE}} = \frac{ES_{y,total}}{EA_{total}}, \tag{4.16}$$

$$y_{\text{PE}} = \frac{ES_{x,total}}{EA_{total}}. \tag{4.17}$$

Then, the parallel axis theorem is used to translate $EI_{x,total}$, $EI_{y,total}$, and $EI_{xy,total}$ (equations (4.13) to (4.15)) to the PE:

$$EI_{x,\text{PE}} = EI_{x,total} - y^2_{\text{PE}} EA_{total}, \tag{4.18}$$

$$EI_{y,\text{PE}} = EI_{y,total} - x^2_{\text{PE}} EA_{total}, \tag{4.19}$$

$$EI_{xy,\text{PE}} = EI_{xy,total} - x_{\text{PE}}\, y_{\text{PE}} EA_{total}. \tag{4.20}$$

The angle between the x-axis (with origin at the PE) and the first principal axis is referred to as the principal stiffness angle ξ, and is defined as:

$$\xi = \frac{1}{2}\tan^{-1}\left(\frac{2EI_{xy,\text{PE}}}{EI_{y,\text{PE}} - EI_{x,\text{PE}}}\right). \tag{4.21}$$

Finally, EI_1 and EI_2 are obtained through:

$$EI_1 = \frac{EI_{x,\text{PE}} + EI_{y,\text{PE}}}{2} + \frac{EI_{x,\text{PE}} + EI_{y,\text{PE}}}{2}\cos 2\xi - EI_{xy,\text{PE}} \sin 2\xi, \tag{4.22}$$

$$EI_2 = \frac{EI_{x,\mathrm{PE}} + EI_{y,\mathrm{PE}}}{2} - \frac{EI_{x,\mathrm{PE}} + EI_{y,\mathrm{PE}}}{2} \cos 2\xi + EI_{xy,\mathrm{PE}} \sin 2\xi. \tag{4.23}$$

The above procedure can be visualized in Figure 4.5, which displays a cross-section with the relevant cross-sectional properties.

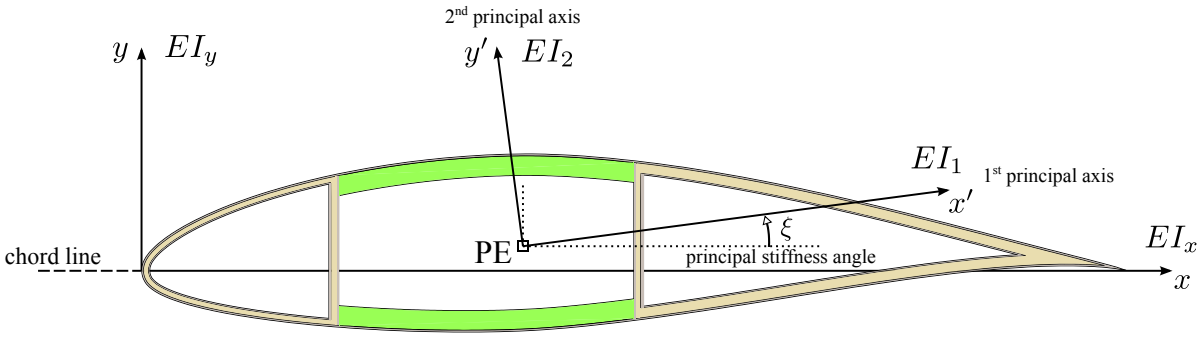

Figure 4.5: Cross-section showing relevant structural properties (ξ enlarged for clarity).

4.2.5 Verification with Analytical Model

This section describes the verification results using an analytical model referred to as the *double-ellipse*. In the double-ellipse model, a blade consists entirely of an elliptical annulus made of a single isotropic material. The double-ellipse model is to verify the calculation of the cross-sectional properties (section 4.2.4) because of its readily available solution. Figure 4.6 displays the cross-section at the blade root and tip for an arbitrary blade. The width and height of the outer ellipse is equal to the chord and thickness of the blade element respectively. The blade element cross-sections in-between the root and tip are not shown in Figure 4.6 for brevity.

In addition to an analytical model, PreComp (**Pre**-processor for computing **Comp**osite blade structural properties) [82] written in FORTRAN by the NWTC will also be used for verification. Cross-sectional properties computed by PreComp include flapwise (EI_x), edgewise (EI_y), longitudinal (EA) and torsion stiffness, cross-coupled stiffness properties (for anisotropic layups), inertia properties, and shear-centre (SC), centre-of-mass (CM), and

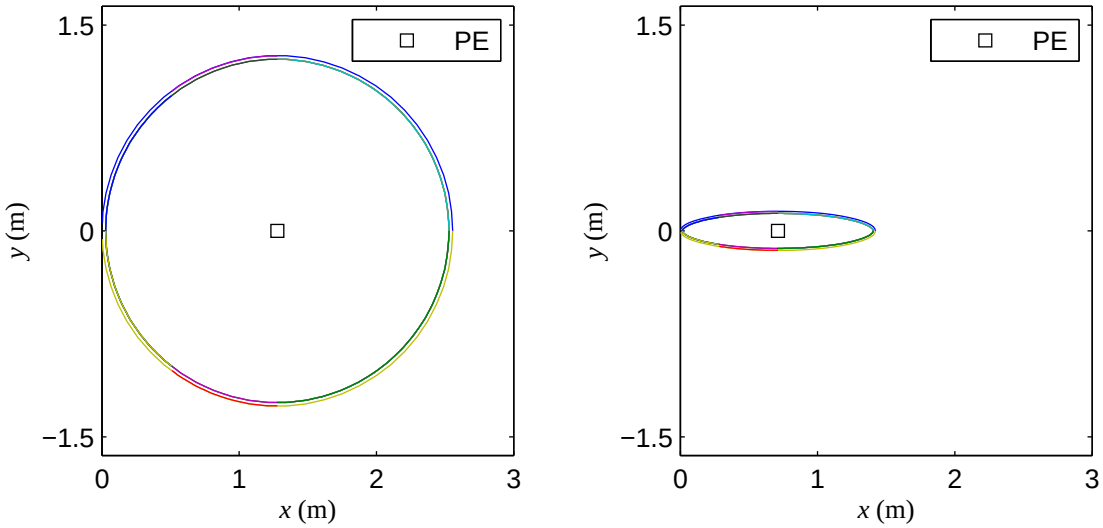

Figure 4.6: Double-ellipse cross-section at blade root (left) and tip (right) of an arbitrary wind-turbine blade.

tension-centre (i.e. PE) offsets. To compute these properties, PreComp uses a method that combines a modified classical laminate theory with a shear-flow approach. The shear-flow approach, akin to Bredt-Batho's for metallic blades, accounts for the warping effects when computing the torsion stiffness, cross-coupled stiffness properties, and other structural properties [83]. Although tailored for composite blades with anisotropic layups, PreComp may also be used to compute cross-sectional properties for the special case of an isotropic composite material. As stated in the user's guide [83], PreComp was verified with analytical models (elliptical, rhombus and rectangular) made of isotropic materials.

The computed, analytical and PreComp results for the relevant cross-sectional properties of an arbitrary blade using the double-ellipse model are shown in Figures 4.7 to 4.10. Since stiffness properties from PreComp are referenced to the SC by default, it was necessary to obtain the computed and analytical stiffness results referenced to the SC for comparison. The SC is defined as the point where a shear force will not give rise to a twisting of the beam. Since the torsional stiffness and SC are not considered in the current cross-sectional model, the PE coordinates from equations (4.16) and (4.17) are manually replaced with the

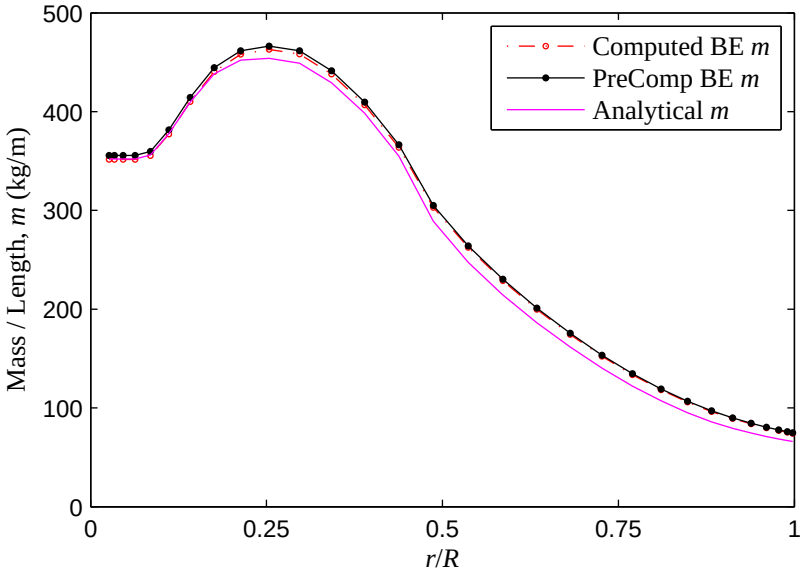

Figure 4.7: Comparison of computed, PreComp, and analytical linear mass m, of an arbitrary blade using double-ellipse model.

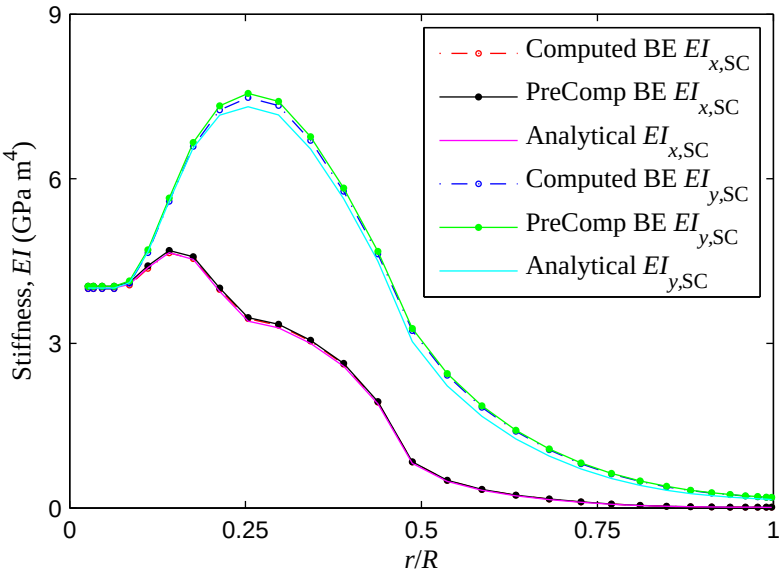

Figure 4.8: Comparison of computed, PreComp, and analytical stiffness $EI_{x,\mathrm{SC}}$ and $EI_{y,\mathrm{SC}}$, of an arbitrary blade using double-ellipse model.

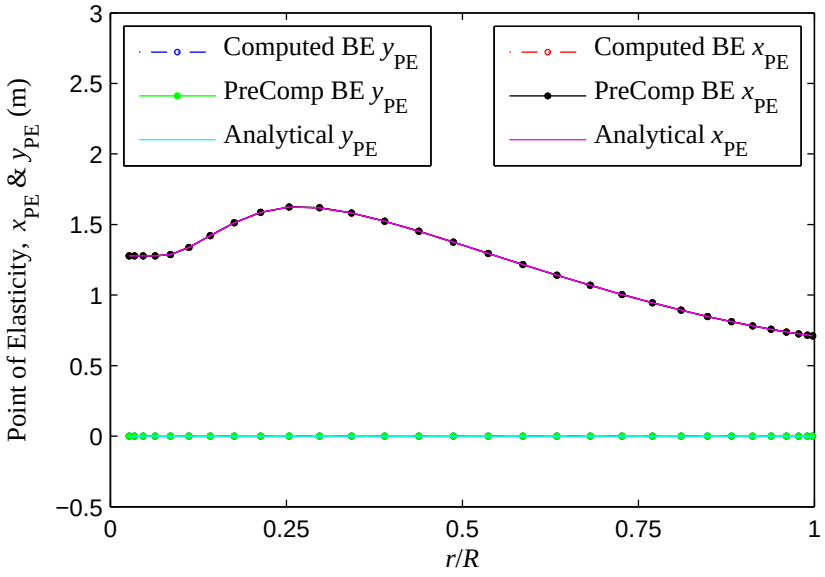

Figure 4.9: Comparison of computed, PreComp, and analytical PE coordinates x_{PE} and y_{PE}, of an arbitrary blade using double-ellipse model.

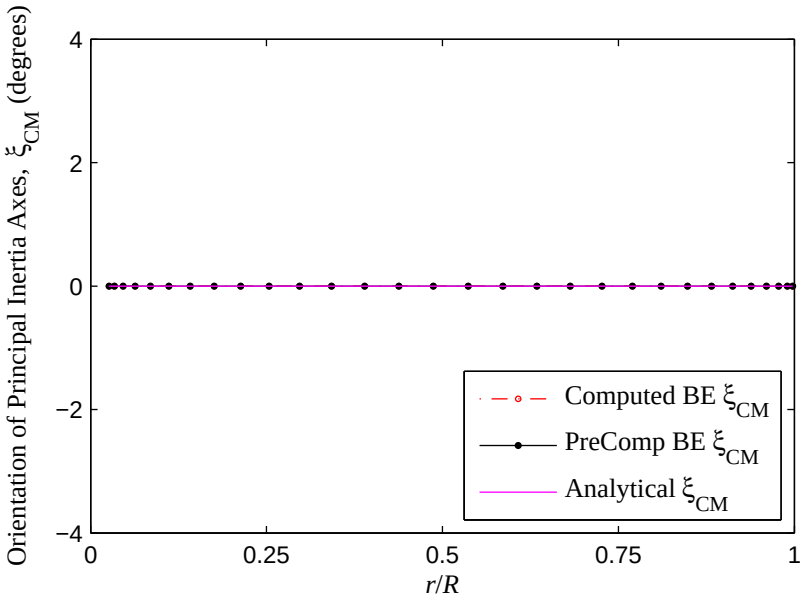

Figure 4.10: Comparison of computed, PreComp, and analytical orientation of principal inertia axes ξ_{CM}, of an arbitrary blade using double-ellipse model.

SC coordinates from PreComp for verification studies only. Similarly, PreComp does not compute the principal stiffness angle ξ, but rather the orientation of the principal inertia axes ξ_{CM}, which is referenced to the CM. Modifications were made to the cross-sectional model to output ξ_{CM}.

Results from Figures 4.7 to 4.10 demonstrate good agreement between the current model and PreComp, but slight discrepancies with the analytical solution. To further distinguish the discrepancies, the relative change Δ, from the analytical solution, is plotted in Figures 4.11 and 4.12. As shown in Figure 4.11, Δ grows in a similar trend for both the cross-sectional model and PreComp from the blade root to tip. The increased magnitude of Δ from PreComp in comparison to the current model is because of the limit imposed by PreComp on the number of airfoil coordinates used as input. Since the resolution of the airfoil profiles for the current model is greater than that of PreComp, it is expected that the current model will have a smaller magnitude of Δ. The maximum values of Δ at the blade root and tip are 1% and 24.4% respectively. Although Δ for the PE coordinates and ξ_{CM} are very small, the significant increase in Δ for the mass and stiffness is disconcerting. Recognizing that similar results were obtained for the current model and PreComp, further study on the double-ellipse was performed.

In the double-ellipse model, the slope of the inner ellipse does not match that of the outer ellipse. As shown on the bottom of Figure 4.13, the relative change in slope Δ_{slope}, between the outer and inner ellipses grows as the relative thickness (t/c) decreases (where t in this case is the outer-ellipse's height). The same trend is observed in Δ from Figure 4.11, where t/c decreases towards the blade tip. Recall from section 4.2.2 that the cross-sectional model calculates the inner-contour coordinates for a given distance (or laminate thickness) normal to the airfoil profile. This procedure is necessary to maintain a constant laminate thickness. As a result, the inner-contour coordinates will have the same slopes as the outer ellipse. In other words, the computed and PreComp inner contours are not ellipses. The difference in

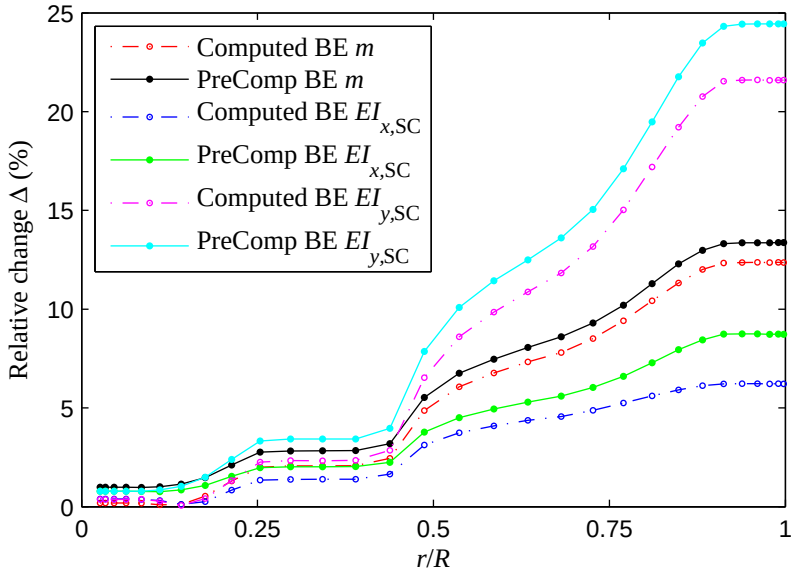

Figure 4.11: Relative change Δ, for linear mass m, and stiffness $EI_{x,\mathrm{SC}}$ and $EI_{y,\mathrm{SC}}$, of an arbitrary blade using double-ellipse model.

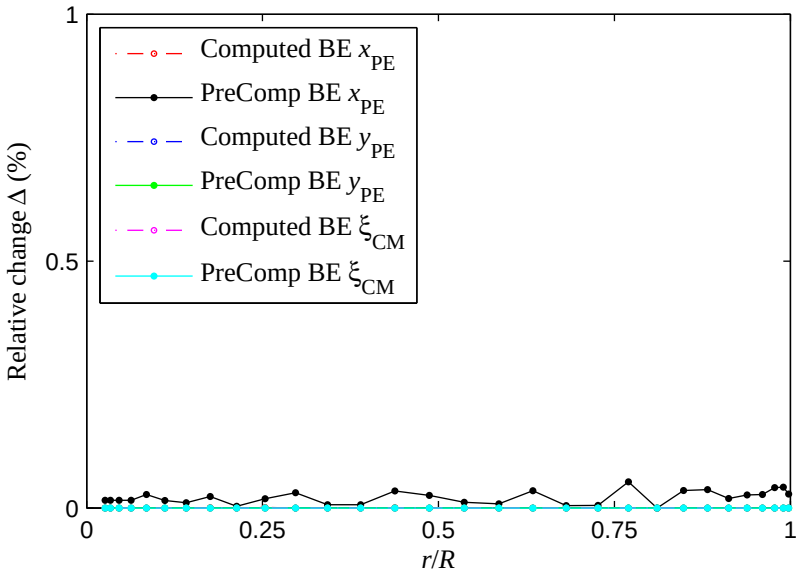

Figure 4.12: Relative change Δ, for PE coordinates x_{PE} and y_{PE}, and orientation of the principal inertia axes ξ_{CM}, of an arbitrary blade using double-ellipse model.

inner-contour shapes are shown in Figure 4.14 for the illustrative case of an outer ellipse with a relative thickness of 20% ($t/c = 0.2$) and $0.09c$ laminate thickness. Note that the magnitude of Δ_{slope} and Δ depends on (t/c) when compared to the laminate thickness, since an infinitesimally thin laminate will result in zero Δ_{slope} and Δ.

Clearly, the cross-sectional model and PreComp are calculating the cross-sectional properties as intended. When the circular root is considered alone, Δ is less than 1% for all cross-sectional properties as shown in Figures 4.11 and 4.12. The reason is because the slope of the inner and outer contours for a circular annulus are identical. Modifying the current model such that the inner-contour coordinates were identical to that of an ellipse resulted in Δ of less than 1.3% for all cross-sectional properties from root to tip of the blade.

4.2.6 Verification for Realistic Blade Cross-Section

The current section describes the verification results for a blade with airfoil and structural-layup geometries that vary along the blade span. The box-type layup as described in section 4.2.1 is implemented. Since this particular cross-section is more sophisticated than the double-ellipse model described in section 4.2.5, an analytical solution is not available. Figures 4.15 to 4.18 display the computed and PreComp results for an arbitrary blade. In contrast to the symmetrical double-ellipse, y_{PE} is not always zero for the more realistic blade cross-section (see Figure 4.17). The asymmetry can also be seen in ξ_{CM} from Figure 4.18, where ξ_{CM} is no longer equal to 0° as in Figure 4.10.

Both codes show good agreement for all properties except for slight discrepancies in the stiffness $EI_{y,\mathrm{SC}}$, the x-coordinate of the PE, and ξ_{CM}. Similarly as explained for the verification of the BEM code with WT_Perf in section 3.5.1, the different methodologies used and small numerical inconsistencies may be the source of discrepancy between the two codes. As mentioned in section 4.2.5, PreComp implements a modified classical laminate theory approach and has a limit on the number of airfoil coordinates used as input. In addition, PreComp does not assume a continuous piece of balsa between the shear web and

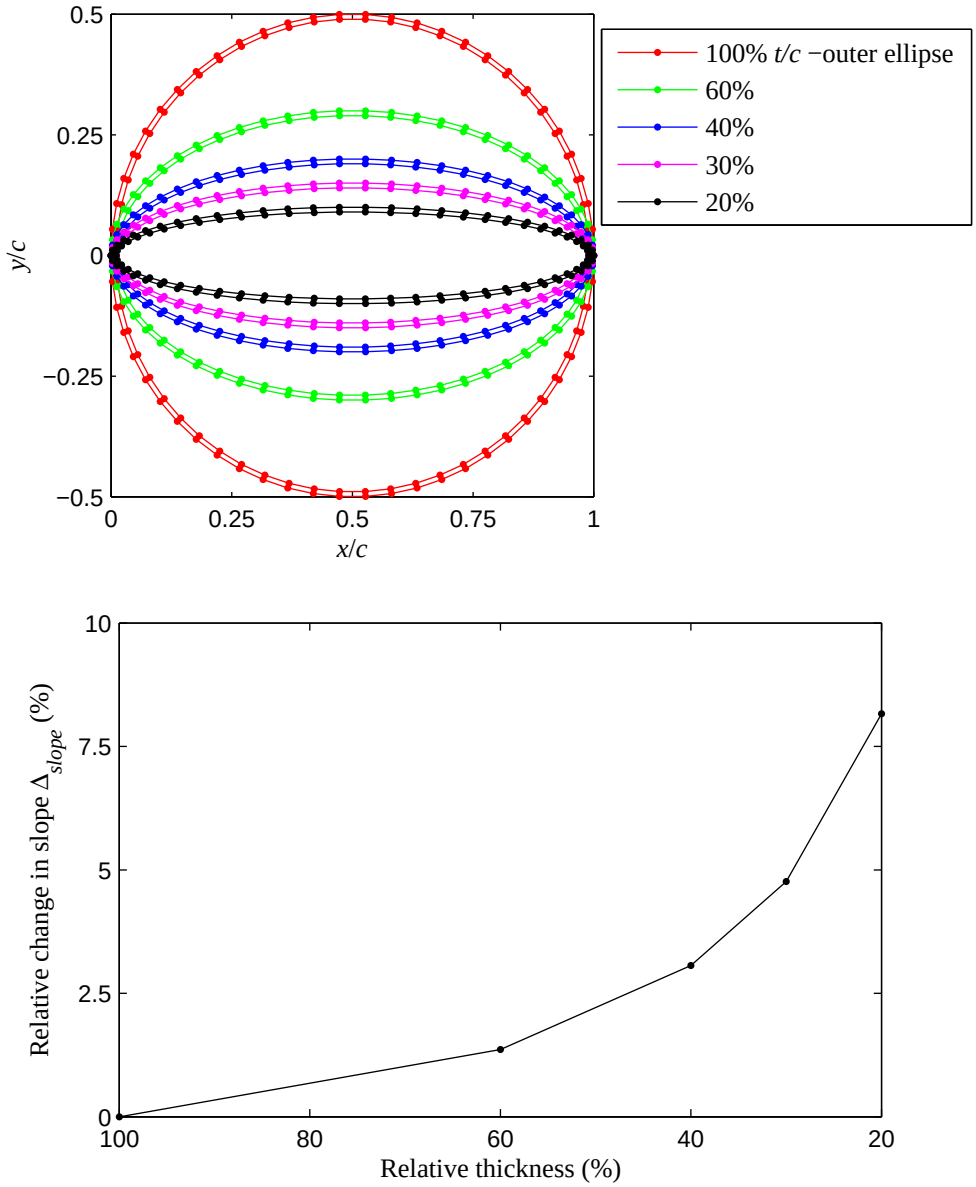

Figure 4.13: Relative change in slope Δ_{slope}, between outer and inner contours (bottom) for double-ellipse model at varying relative thickness (t/c) (top).

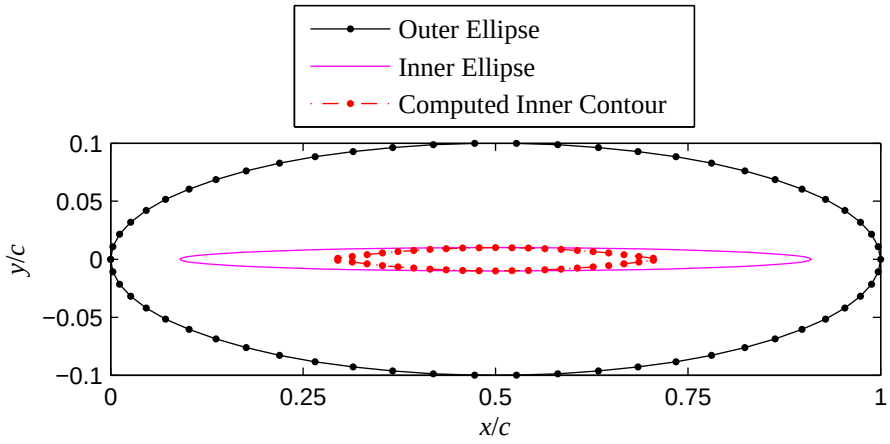

Figure 4.14: Comparison between inner contours from computed results and analytical solution. An outer ellipse with 20% relative thickness ($t/c = 0.2$) and $0.09c$ laminate thickness is shown.

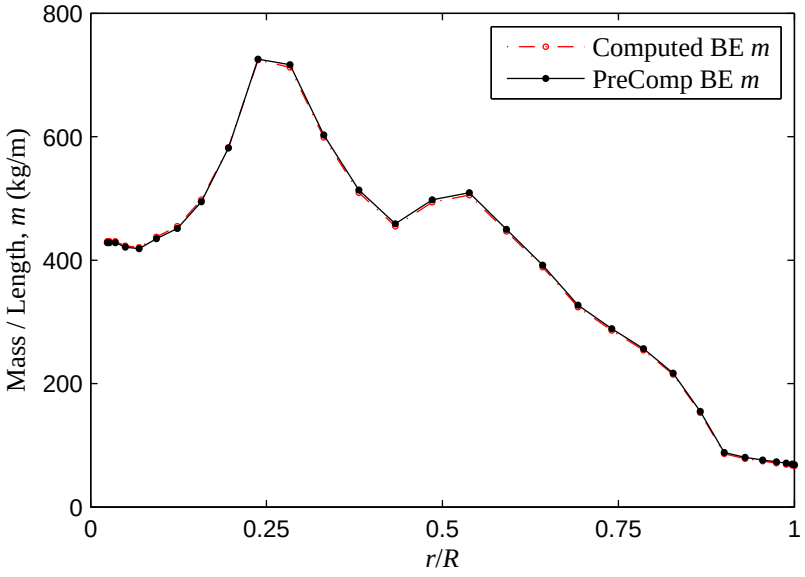

Figure 4.15: Comparison of computed and PreComp linear mass m, of an arbitrary blade for box-type layup.

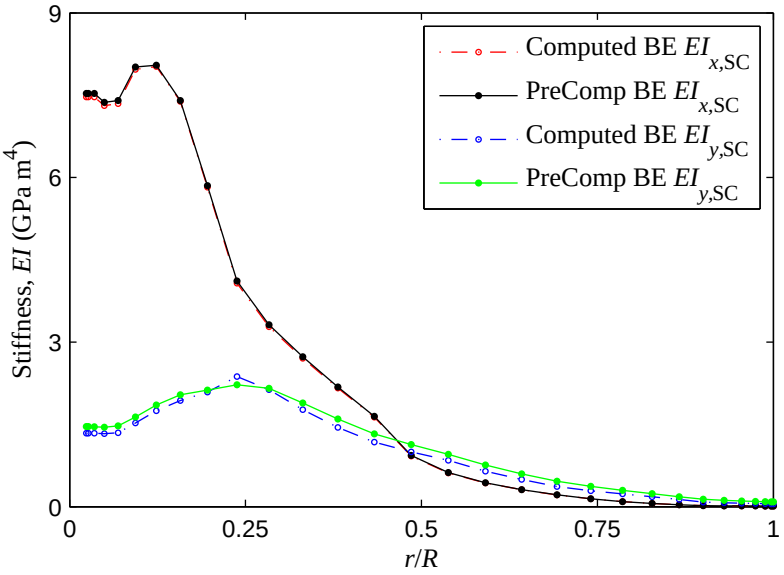

Figure 4.16: Comparison of computed and PreComp stiffness $EI_{x,\mathrm{SC}}$ and $EI_{y,\mathrm{SC}}$, of an arbitrary blade for box-type layup.

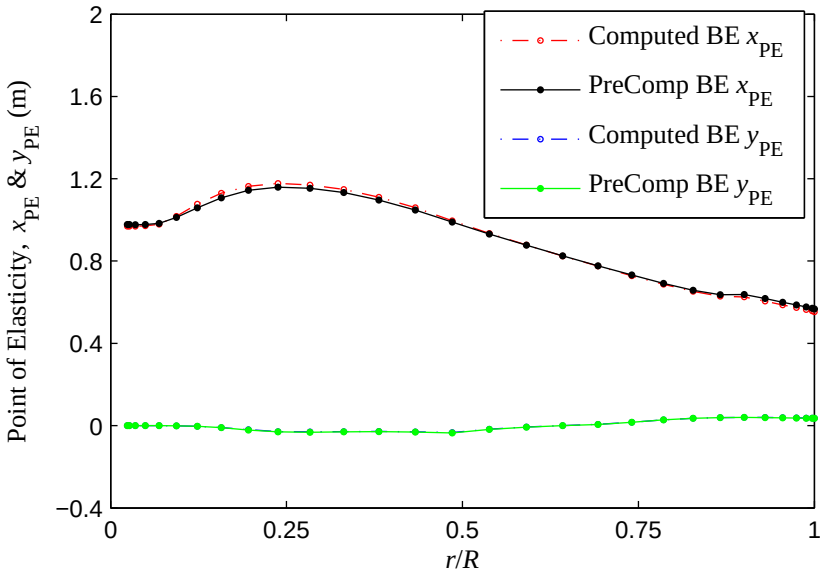

Figure 4.17: Comparison of computed and PreComp PE coordinates x_{PE} and y_{PE}, of an arbitrary blade for box-type layup.

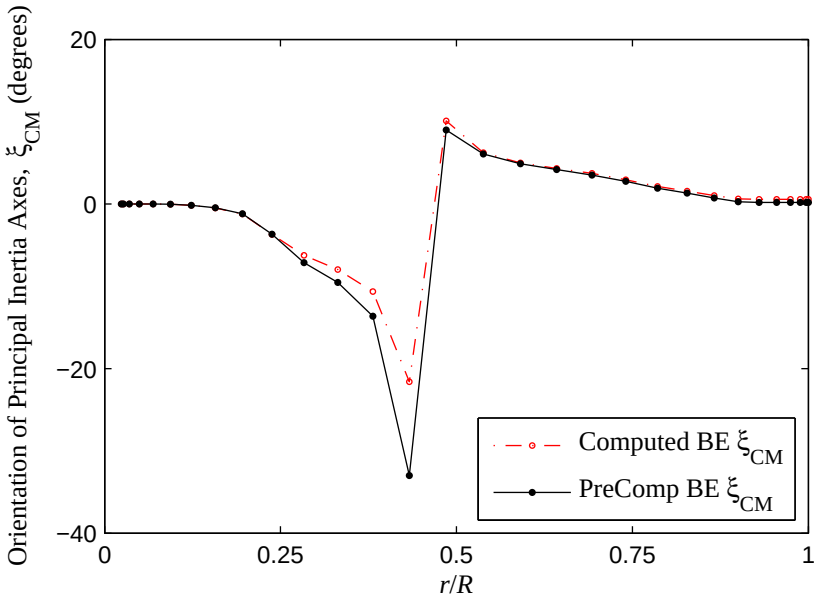

Figure 4.18: Comparison of computed and PreComp orientation of the principal inertia axes ξ_{CM}, of an arbitrary blade for box-type layup.

panel (see section 4.2.1) and positions the shear webs in a slightly different location than in the cross-sectional model described here. For the remainder of this thesis, it will be assumed that the developed cross-sectional model is sufficiently accurate, and for brevity, the relative change (Δ) between the cross-sectional model and PreComp will not be discussed.

4.3 Beam Model

4.3.1 Bending Moments and Deflections

Having computed the aerodynamic loads from BEM (section 3.3), and the blade structural properties from the cross-sectional model (section 4.2), it is now possible to calculate the bending moments and deflections as described by Hansen [8]. As explained in section 4.1 and illustrated in Figure 4.19, a wind-turbine blade can be modelled as a beam. Here, a prismatic cantilever beam with a rectangular cross-section is assumed. Hence, the cross-section from root to tip is uniform and EI is constant. In reality, the wind-turbine blade is tapered, twisted, and varies in EI from root to tip. However, the box formed by the spar caps –which

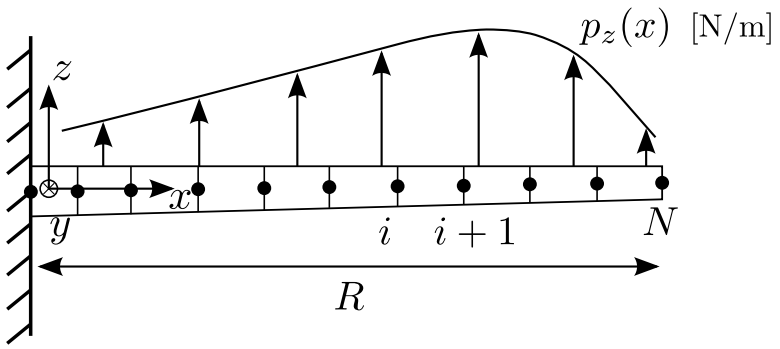

Figure 4.19: A wind-turbine blade modelled as a beam. Reproduced from [8].

mostly determines the blade stiffness– and shear webs, is nearly rectangular in shape as in a beam (see Figure 4.5)[1]. In the beam model, the blade is divided into N number of blade elements that coincide with the blade elements in BEM. First, the aerodynamic loads p_n and p_t are taken from the maximum thrust experienced between $V_{o,cut\text{-}in}$ and $V_{o,cut\text{-}out}$ as shown in Figure 3.10(b), and rotated by the corresponding pitch angle θ, to obtain p_z and p_y. The point of maximum thrust is when the aerodynamic loads reach their maximum possible values, and therefore the worst-case scenario for structural considerations. Then, the shear forces T_z and T_y, and bending moments M_y and M_z, are calculated for each blade element by numerically integrating equations (4.24) to (4.27):

$$\frac{dT_z}{dx} = -p_z(x), \tag{4.24}$$

$$\frac{dT_y}{dx} = -p_y(x), \tag{4.25}$$

$$\frac{dM_y}{dx} = T_z(x), \tag{4.26}$$

$$\frac{dM_z}{dx} = -T_y(x), \tag{4.27}$$

which are derived from a free body diagram of an infinitesimal piece of the beam (Figure 4.20). Only the static case is considered, and hence the inertia terms $m(x)\ddot{\delta}_z(x, t_s)$ and

[1]This is true along the outer portion of the blade, but at the cylindrical root, the spar caps and shear webs are somewhere in between a box and a cylinder [84].

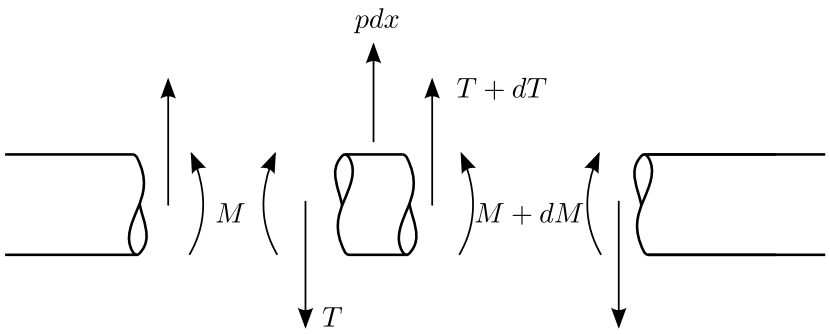

Figure 4.20: Free body diagram for an infinitesimal piece of the beam. Reproduced from [8].

$m(x)\ddot{\delta}_y(x,t_s)$, where δ is the deflection and t_s is time, in equations (4.24) and (4.25) have been neglected.

The bending moments about the principal axes are obtained using:

$$M_1 = M_y \cos(\beta+\xi) - M_z \sin(\beta+\xi), \tag{4.28}$$

$$M_2 = M_y \sin(\beta+\xi) + M_z \cos(\beta+\xi) \tag{4.29}$$

where β is the twist measured from the tip chord and ξ is the principal stiffness angle. The curvatures about the principal axes are calculated from Euler-Bernoulli beam theory:

$$\kappa_1 = \frac{M_1}{EI_1}, \tag{4.30}$$

$$\kappa_2 = \frac{M_2}{EI_2}, \tag{4.31}$$

which are rotated back to the y- and z-axes using:

$$\kappa_z = -\kappa_1 \sin(\beta+\xi) + \kappa_2 \cos(\beta+\xi), \tag{4.32}$$

$$\kappa_y = \kappa_1 \cos(\beta+\xi) + \kappa_2 \sin(\beta+\xi). \tag{4.33}$$

The slopes ψ_y and ψ_z, and deflections δ_z and δ_y, are obtained numerically from:

$$\frac{d\psi_y}{dx} = \kappa_y, \tag{4.34}$$

$$\frac{d\psi_z}{dx} = \kappa_z, \tag{4.35}$$

$$\frac{d\delta_z}{dx} = -\psi_y, \tag{4.36}$$

$$\frac{d\delta_y}{dx} = \psi_z \tag{4.37}$$

where δ_z and δ_y are rotated by θ to attain δ_n and δ_t. To solve the shear forces, bending moments, slopes, and deflections, the boundary conditions for a cantilever beam where $T_z^{(N)} = 0$, $T_y^{(N)} = 0$, $M_y^{(N)} = 0$, $M_z^{(N)} = 0$, $\psi_y^{(1)} = 0$, $\psi_z^{(1)} = 0$, $\delta_z^{(1)} = 0$, and $\delta_y^{(1)} = 0$ are applied when integrating equations (4.24) to (4.27) and equations (4.34) to (4.37) respectively. The superscripts (1) and (N) correspond to the blade root and tip respectively.

4.3.2 Verification of Bending Moment and Deflection Calculations

To verify the beam model calculations, the 2 MW Tjæreborg turbine test case from Hansen [8] is chosen. From this test case, it is possible to verify the aerodynamic loads computed from BEM and the bending moments from the beam model. To perform such a verification, the aerodynamic and structural data for the Tjæreborg turbine from Øye [85, 86] was used. Figure 4.21 displays the results from BEM and the digitized data from Hansen for the aerodynamic load about the first principal axis at $V_o = 10\,\mathrm{m/s}$. As shown in Figure 4.21, the aerodynamic load from BEM and Hansen are in good agreement, which is necessary for verification of the bending moment calculations through equations (4.24) to (4.29). The good agreement between the beam model and the digitized data from Hansen in Figure 4.22 confirms that the bending moments are computed correctly.

The 2 MW Tjæreborg turbine test case does not provide a verification of the deflection calculations (equations (4.34) to (4.37)) unless the effect of the centrifugal force on the deflected blades, known as *centrifugal stiffening*, is included in the beam model. Centrifugal stiffening reduces the flapwise bending moment from the blade root to tip (see Figure 4.22), and can be included in the beam model by adding the centrifugal load to the aerodynamic loads (see Hansen [8]). Since the extra loading from the centrifugal force depends on κ and ψ, which in turn depends on the aerodynamic loads, an iterative procedure is necessary

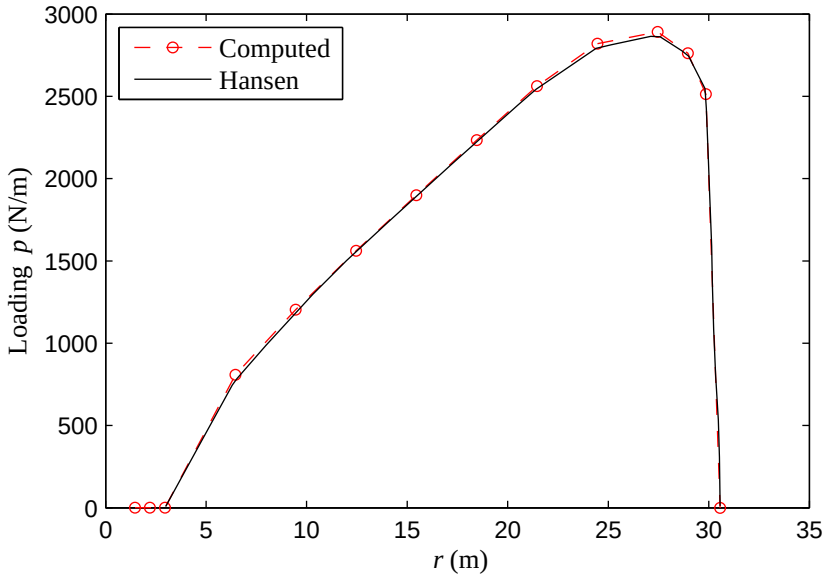

Figure 4.21: Computed aerodynamic load about the first principal axis vs. from Hansen [8] for 2 MW Tjæreborg turbine at $V_o = 10\,\mathrm{m/s}$.

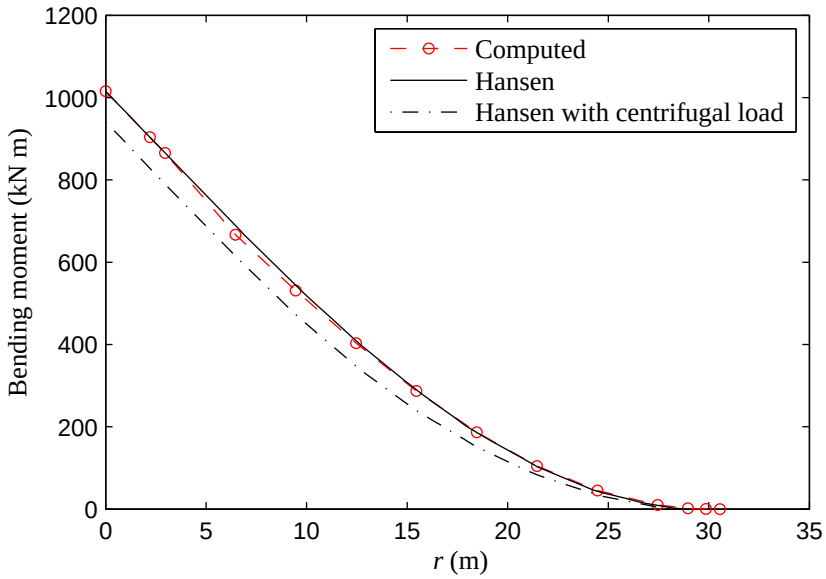

Figure 4.22: Computed bending moment about the first principal axis vs. from Hansen [8] for 2 MW Tjæreborg turbine at $V_o = 10\,\mathrm{m/s}$.

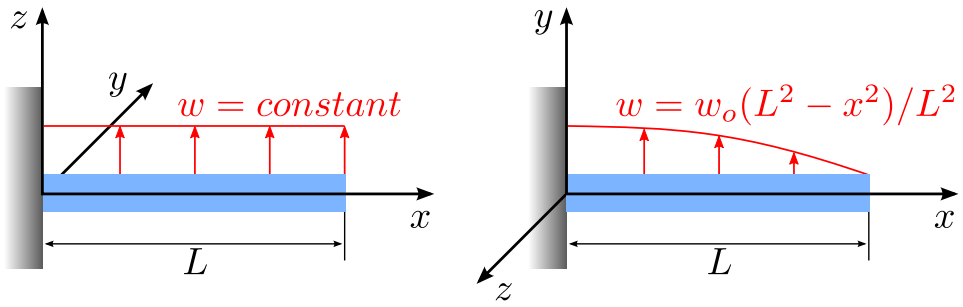

Figure 4.23: Simple distributed loads on a cantilever beam gives an analytical solution for the deflections.

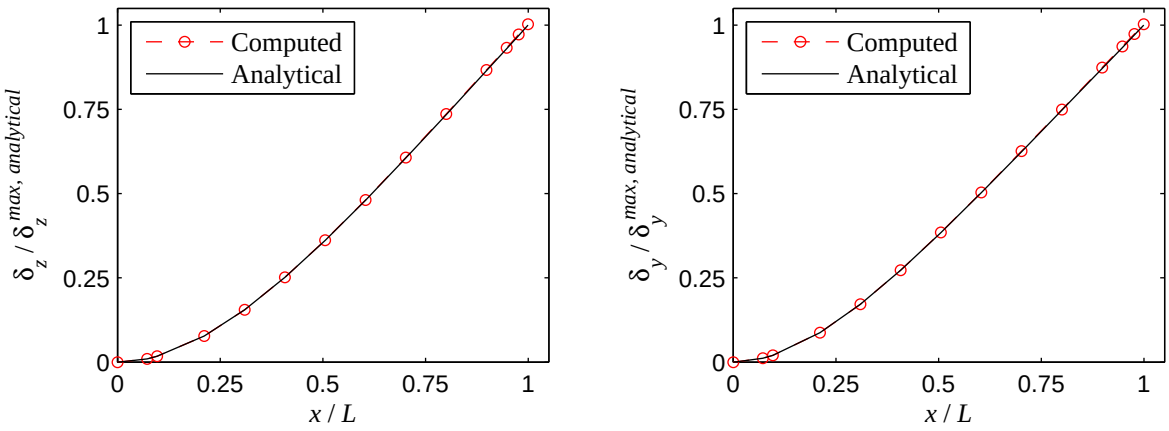

Figure 4.24: Computed normal (δ_z) and tangential (δ_y) deflections vs. analytical results.

to obtain the bending moments and deflections. The author has made several attempts to include centrifugal stiffening within the beam model, but did not manage to achieve a stationary solution. It is assumed that centrifugal stiffening has a negligible effect and to verify the calculation of the deflections, an analytical test case is used instead. The analytical test case is illustrated in Figure 4.23, and the computed and analytical results are shown in Figure 4.24. A relative change of less than 0.5% was achieved.

4.4 Structural Optimization and Constraints

As stated in section 4.2.1, the thickness distribution of the spar caps between the blade root and tip is an optimization variable (Figure 4.25(a)). The spar-cap thickness (SCT) is not

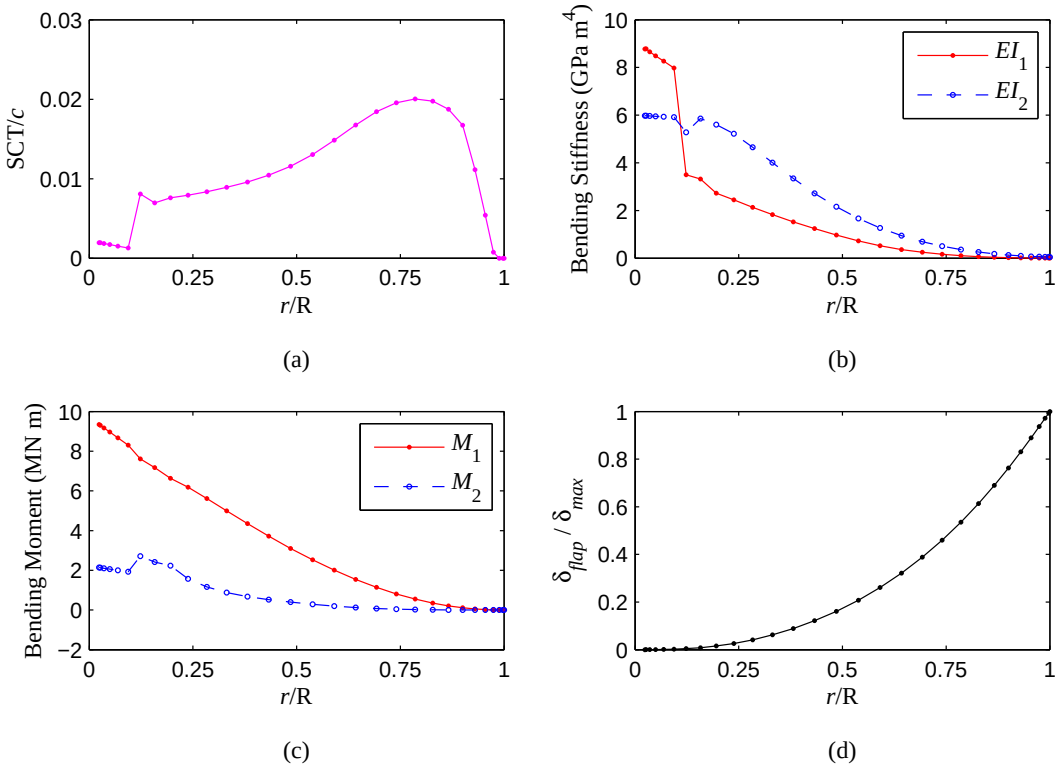

Figure 4.25: Blade element spar-cap thickness (SCT) (a), bending stiffness (b), bending moment (c), and flapwise deflection (d) distributions for an arbitrary blade. Retrieved from [3].

determined by the conventional or hybrid MOEA as described in Chapter 5, but through an optimization scheme internal to the code describing the structural model instead. The internal optimization minimizes the blade mass m_{blade}, while satisfying the strain and tip deflection constraints to be presented below. When a particular blade cannot satisfy the strain or tip deflection constraints, the optimization determines the SCT distribution such that the constraint violation is a minimum. Once the spar-cap thickness distribution is found, the element bending stiffness (EI_1 and EI_2) and bending moment (M_1 and M_2) distributions about the principal axes (Figures 4.25(b) and 4.25(c)) can be used to calculate the strain. From Euler-Bernoulli beam theory, the strain in the cross-section using the x'- and y'-coordinate frame (see Figure 4.26) is given by:

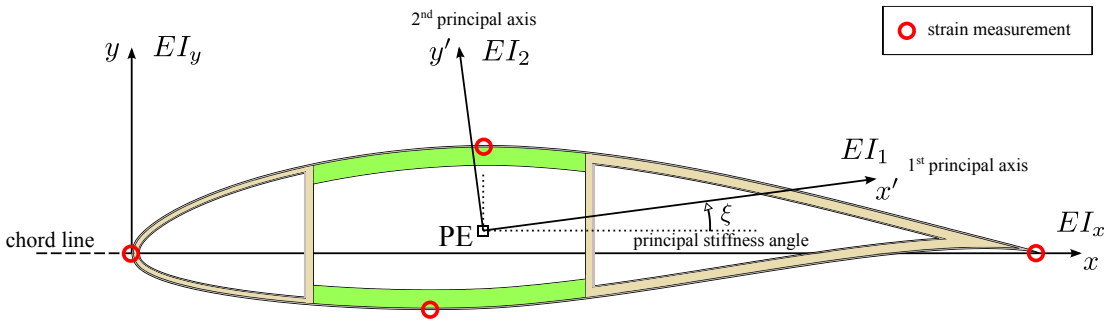

Figure 4.26: Cross-section showing structural properties and strain measurement locations (ξ enlarged for clarity). Retrieved from [3].

$$\varepsilon(x', y') = \frac{M_1}{EI_1} y' - \frac{M_2}{EI_2} x' + \frac{N_{z,norm}}{EA}. \tag{4.38}$$

Evaluating equation (4.38) for the entire cross-section is difficult, and hence assumptions are made for simplification. First, since the longitudinal stiffness EA, is large and the normal force $N_{z,norm}$, is small for large-scale wind-turbine blades, the third term in equation (4.38) is assumed negligible:

$$\varepsilon(x', y') = \frac{M_1}{EI_1} y' - \frac{M_2}{EI_2} x'. \tag{4.39}$$

The two terms in equation (4.39) represents two distinct strain components, which were aggregated based on the principle of superposition of Euler-Bernoulli beam theory to yield the total strain occurring on a blade element. Here, each strain component is treated separately as ε_1 and ε_2, and whether ε is in compression ($-$) or tension ($+$) is not considered, as shown by:

$$\varepsilon_1 = \left| \frac{M_1}{EI_1} \right| |y'|, \tag{4.40}$$

$$\varepsilon_2 = \left| \frac{M_2}{EI_2} \right| |x'|. \tag{4.41}$$

Clearly, the maximum strain occurs at y'_{max} or y'_{min} for ε_1, and x'_{max} or x'_{min} for ε_2:

$$\varepsilon_{1,max} = \left| \frac{M_1}{EI_1} \right| \max[|y'_{max}|, |y'_{min}|], \tag{4.42}$$

$$\varepsilon_{2,max} = \left| \frac{M_2}{EI_2} \right| \max[|x'_{max}|, |x'_{min}|]. \tag{4.43}$$

As a result, x'_{max}, x'_{min}, y'_{max} and y'_{min} become the strain monitoring locations as shown in Figure 4.2. The x'- and y'-coordinates referenced to the principal axes are obtained via transformation of x and y using:

$$\begin{bmatrix} x' \\ y' \end{bmatrix} = \begin{bmatrix} \cos\xi & \sin\xi \\ -\sin\xi & \cos\xi \end{bmatrix} \begin{bmatrix} (x - x_{\mathrm{PE}}) \\ (y - y_{\mathrm{PE}}) \end{bmatrix}. \tag{4.44}$$

Equations (4.42) and (4.43) can now be easily implemented with the optimization algorithm as a strain constraint given by:

$$(\max[\varepsilon_{1,max}, \varepsilon_{2,max}] - \varepsilon_{max})/\varepsilon_{max} \leq 0. \tag{4.45}$$

The maximum allowable strain (ε_{max}) in equation (4.45) is a value used typically in blade design and is not associated to specific material and safety factor choices. The value of ε_{max} is also constant from the blade root to tip.

The maximum tip deflection δ_{max}, in equation (4.46) is equal to 50% of the initial blade tip clearance, which is the allowable tip deflection under normal turbine operation for a quasi-static analysis in the Germanischer Lloyd regulations [87]:

$$(\delta^{tip}_{flap} - \delta_{max})/\delta_{max} \leq 0. \tag{4.46}$$

The flapwise tip deflection δ^{tip}_{flap}, is equal to δ_n (or δ_{flap}) at the blade tip. Figure 4.25(d) displays δ_n for an arbitrary wind-turbine blade.

Chapter 5

HYBRID MULTI-OBJECTIVE EVOLUTIONARY ALGORITHM

5.1 Multi-Objective Optimization Concepts

We consider a multi-objective optimization problem of the form:

$$\begin{aligned} &\text{minimize} && f_1(\mathbf{x}), f_2(\mathbf{x}), \ldots, f_q(\mathbf{x}) \\ &\text{subject to} && \mathbf{x} \in X \\ & && X = \{\mathbf{x} \in \mathbb{R}^n | \\ & && \quad g_d(\mathbf{x}) = 0, d = 1, \ldots, N_d | \\ & && \quad h_e(\mathbf{x}) \leq 0, e = 1, \ldots, N_e | \\ & && \quad x_k^L \leq x_k \leq x_k^U, k = 1, \ldots, n\} \end{aligned} \tag{5.1}$$

with $q \geq 2$ possibly conflicting objective functions. The vector of objectives $\mathbf{z} = \mathbf{f}(\mathbf{x}) = (f_1(\mathbf{x}), f_2(\mathbf{x}), \ldots, f_q(\mathbf{x}))$ is called an objective vector and the vector of decision variables $\mathbf{x} = (x_1, x_2, \ldots, x_n)$ a decision vector. The decision vector $\mathbf{x}$ is an element of the n-dimensional real numbers $\mathbf{x} \in \mathbb{R}^n$ that satisfy all constraints. The functions $g_d(\mathbf{x})$ and $h_e(\mathbf{x})$ are equality and inequality constraints respectively, and the decision variables x_k are bounded by upper (x_k^U) and lower (x_k^L) values. Altogether, $\mathbf{x}$ belongs to the feasible region X. Problem (5.1) may be expressed as a combination of maximization and minimization of $\mathbf{f}(\mathbf{x})$ as well. For this chapter, concepts will be explained treating problem (5.1) as minimization only (unless otherwise stated) and in Chapter 6 as a combination of minimization and maximization. Three definitions regarding optimality in multi-objective optimization follow:

Definition 1: The decision vector $\mathbf{x}^* \in X$ for problem (5.1) is called a Pareto-optimal solution if there does not exist another $\mathbf{x} \in X$ such that $f_i(\mathbf{x}) \leq f_i(\mathbf{x}^*)$ for all $i = 1, \ldots, q$ and

$f_j(\mathbf{x}) < f_j(\mathbf{x}^*)$ for at least one j where $j = 1, \ldots, q$. An objective vector is Pareto optimal if the corresponding decision vector is Pareto optimal as well. The set of all objective vectors that are Pareto optimal is known as the Pareto front.

Definition 2: The decision vector $\mathbf{x}^* \in X$ for problem (5.1) is called a weakly Pareto-optimal solution if there does not exist another $\mathbf{x} \in X$ such that $f_i(\mathbf{x}) < f_i(\mathbf{x}^*)$ for all $i = 1, \ldots, q$. An objective vector is weakly Pareto optimal if the corresponding decision vector is weakly Pareto optimal.

Definition 3 (from Geoffrion [88]): The decision vector $\mathbf{x}^* \in X$ for problem (5.1) is called a properly Pareto-optimal solution if it is Pareto optimal and if there is some real number $M > 0$ such that for each $f_i(\mathbf{x})$ and each $\mathbf{x} \in X$ satisfying $f_i(\mathbf{x}) < f_i(\mathbf{x}^*)$, there exists at least one $f_j(\mathbf{x})$ such that $f_j(\mathbf{x}^*) < f_j(\mathbf{x})$ and

$$\frac{f_i(\mathbf{x}^*) - f_i(\mathbf{x})}{f_j(\mathbf{x}) - f_j(\mathbf{x}^*)} \leq M. \tag{5.2}$$

An objective vector is properly Pareto optimal if the corresponding decision vector is properly Pareto optimal. In other words, a solution is properly Pareto optimal if there is at least one pair of objectives for which a finite decrement in one objective is possible only at the expense of some reasonable increment in the other objective [89]. The properly Pareto-optimal set represents bounded trade-offs within the Pareto-optimal set. Based on these three optimality definitions, the properly Pareto-optimal set is a subset of the Pareto-optimal set which is a subset of the weakly Pareto optimal set.

In the field of multiple criteria decision making (see e.g. Miettinen [90]), multi-objective optimization problems are treated in a single-objective sense by using scalarization functions. Among the numerous different scalarization functions available in the literature, an achievement scalarizing function (ASF) [90, 91] is commonly used and is given by:

$$\begin{aligned} &\text{minimize} \quad \max_{i=1}^{q} w_i(f_i(\mathbf{x}) - \bar{z}_i) + \rho_o \sum_{i=1}^{q} w_i(f_i(\mathbf{x}) - \bar{z}_i) \\ &\text{subject to} \quad \mathbf{x} \in X \end{aligned} \tag{5.3}$$

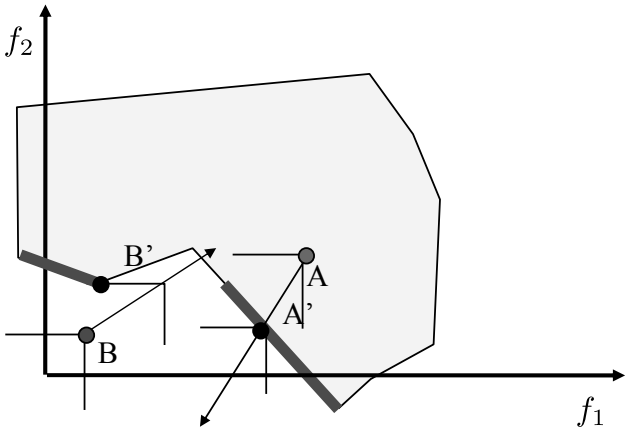

Figure 5.1: Illustrating the projection of a feasible (A) and infeasible (B) reference point onto the Pareto front (thick lines). Reproduced from [12]. ©2009 Massachusetts Institute of Technology.

where $w_i = 1/(z_i^{max} - z_i^{min})$ is a weight factor assigned to each objective function $f_i(\mathbf{x})$ and $\bar{z}_i$ is a reference point $\bar{\mathbf{z}} \in \mathbb{R}^q$. An augmentation term where ρ_o takes a small positive value (e.g. 10^{-6}) is added to produce properly Pareto-optimal solutions. Here, ρ_o is called an augmentation coefficient and provides a bound for desirable or acceptable trade-offs (see definition 3). If the augmentation term is removed, the solutions to problem (5.3) can be weakly Pareto optimal. That is, the augmentation term guarantees Pareto-optimal solutions independent of $\bar{\mathbf{z}}$. When the ASF is solved, the reference point $\bar{\mathbf{z}}$ is projected onto the Pareto front in a direction specified by the weight factor $\mathbf{w}$. In the context of hybrid MOEAs, the maximum and minimum values of each objective function in the current population are z_i^{max} and z_i^{min} respectively. Furthermore, the reference point $\bar{\mathbf{z}}$ is the objective vector of an individual selected for local search. Figure 5.1 illustrates the projection of a feasible (A) and infeasible (B) reference point onto the Pareto front (thick lines). The resulting Pareto-optimal solutions of A and B are A' and B' respectively. The cones (orthogonal lines on A, A', B and B') represent the indifference curves when $\rho_o = 0$ in the ASF and the last point where the cone intersects the feasible region (shaded area in Figure 5.1) is the solution obtained [12]. When $\rho_o > 0$, a broader cone is formed than the one shown in Figure 5.1.

Equation (5.3) has a non-differentiable objective function and hence gradient-based solvers

cannot be used. To apply a gradient-based solver, the ASF can be converted into a differentiable equivalent as discussed in [90].

5.2 Concurrent-Hybrid NSGA-II

The hybrid algorithm developed by the author is based on the concurrent-hybrid NSGA-II (hybrid NSGA-II) by Sindhya et al. [57]. The hybridization is composed of a non-gradient based MOEA and a gradient-based local search. In [57], the NSGA-II is chosen as the MOEA and the sequential quadratic programming (SQP) method for the gradient-based local search. The local search entails solving the differentiable version of equation (5.3) and is applied according to a predefined saw-tooth probability function P_l^{local}. In this work, an alternative MOEA could be used instead of the NSGA-II, however, the NSGA-II is selected for the same reasons as stated in [57]. For the gradient-based local search, the MATLAB R2011a *fminimax* command is used since it reformulates equation (5.3) into its differentiable form and applies the SQP method automatically [27]. The hybrid NSGA-II step-by-step procedure is given below:

1. Generate a random initial population P_o of size N_{pop} and set iteration count $l = 0$;

2. Sort population to different non-domination levels (fronts $i = 1, 2, \ldots$, etc.) and assign each individual a fitness equal to its non-dominated level ($i = 1$ is the best level);[1]

3. Create offspring population Q_l of size N_{pop} using binary tournament selection, crossover and mutation operators;

4. Perform non-dominated sorting to Q_l and identify different fronts $\mathcal{K}_i$, $i = 1, 2, \ldots$, etc.;

[1]This procedure is non-dominated sorting, see section 5.3.

5. Perform local search on some individuals chosen with a probability of P_l^{local} from the offspring population Q_l in front $\mathcal{K}_1$. Replace the chosen individuals from the offspring population with the improved individuals from the local search;

6. Combine the parent and offspring populations and create $R_l = P_l \cup Q_l$;

7. Perform non-dominated sorting to R_l and identify different fronts $\mathcal{F}_i, i = 1, 2, \ldots,$ etc.;

8. Set new population $P_{l+1} = \emptyset$. Set a count $i = 1$ and as long as $|P_{l+1}| + |\mathcal{F}_i| \leq N_{pop}$, perform $P_{l+1} = P_{l+1} \cup F_i$ and $i = i + 1$;

9. Include the most widely spread $(N_{pop} - |P_{l+1}|)$ members of $\mathcal{F}_i$ by clustering $\mathcal{F}_i$ into $(N_{pop} - |P_{l+1}|)$ clusters and choosing one representative individual from each cluster;

10. Check if the maximum number of objective-function evaluations has exceeded. If yes, terminate the algorithm, else set $l = l + 1$ and return to step 2.

The selection, crossover and mutation operators in step 3 are the main constituents of a GA and several different types exist for each. Binary tournament selection is an example of a selection operator and is used in the NSGA-II. The type of operators chosen for solving a particular optimization problem will have the most significant effect on the performance of a GA. In addition, each operator includes parameter settings that also influences the GA's performance. Detailed explanation of the three operators can be found in one of many available textbooks on the topic (e.g. Deb [13]). Binary tournament selection, crossover and mutation are briefly described in sections 5.6 to 5.8.

The algorithm described above differs from [57] in steps 4, 5, and 9. Step 4 is an additional step necessary for step 5, which allows only the best $(i = 1)$ offspring to be chosen for local

search. In step 9, the NSGA-II crowding routine [14] for including the most widely spread members of F_i is replaced by the clustering approach used in SPEA [92]. The clustering approach is shown in [93] to produce a better spread of solutions in comparison with the NSGA-II crowding routine for a number of three-objective test problems.

5.3 Non-dominated Sorting

The non-dominated sorting procedure is described in this section. The domination between two individuals (solutions) $\mathbf{x}^{(1)}$ and $\mathbf{x}^{(2)}$, is defined as follows [13]:

Individual $\mathbf{x}^{(1)}$ is said to dominate $\mathbf{x}^{(2)}$, if both the following conditions are true:

1. Individual $\mathbf{x}^{(1)}$ is no worse than $\mathbf{x}^{(2)}$ in all objectives. Thus, $\mathbf{x}^{(1)}$ and $\mathbf{x}^{(2)}$ are compared based on their objective-function values $\mathbf{f}(\mathbf{x}^{(1)})$ and $\mathbf{f}(\mathbf{x}^{(2)})$.

2. Individual $\mathbf{x}^{(1)}$ is strictly better than $\mathbf{x}^{(2)}$ in at least one objective.

For a given population (set of solutions), a pairwise comparison can be made using the above definition (Figure 5.2(a)). All individuals that are not dominated by any other are non-dominated, and their objective vectors constitute the first non-dominated front $\mathcal{F}_1$ (Figure 5.2(b)). To classify the entire population into different non-domination levels (or fronts $\mathcal{F}_i$), the procedure as previously described in section 2.4 is performed. Once the non-dominated individuals of level 1 ($\mathcal{F}_1$) are determined, they are temporarily disregarded from the population. Then, the non-dominated individuals of level 2 ($\mathcal{F}_2$) are determined from the non-dominated individuals of the remaining population. The procedure is repeated until the entire population is classified into a non-dominated level. Figure 5.3 illustrates the non-dominated fronts for a population of five individuals (i.e. $P = \{1, 2, 3, 4, 5\}$). Hence, the non-dominated fronts of P is as follows:

$$\mathcal{F}_1 = \{3, 5\}, \quad \mathcal{F}_2 = \{1, 4\}, \quad \mathcal{F}_3 = \{2\}.$$

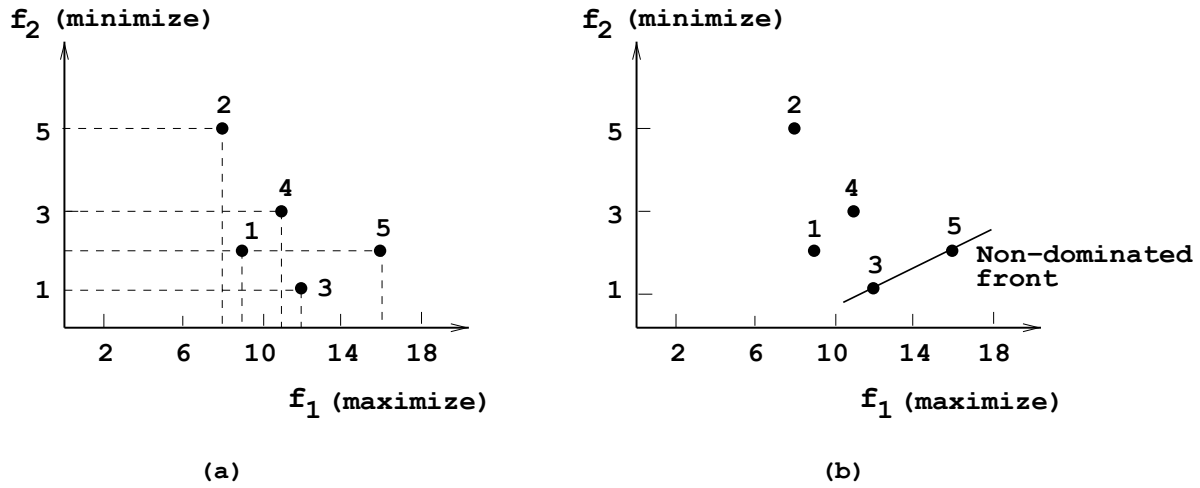

Figure 5.2: A set of individuals and the first non-dominated front are shown. Reproduced from [13]. ©2001 John Wiley & Sons Ltd.

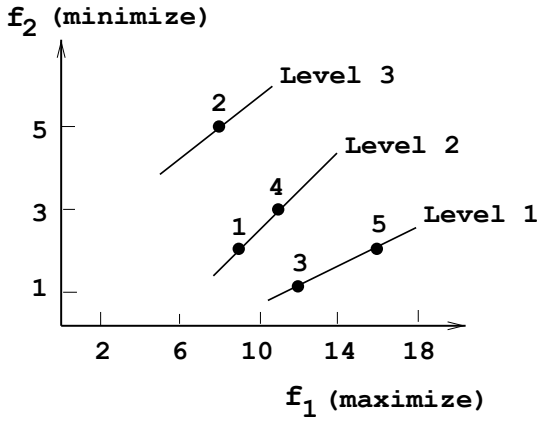

Figure 5.3: A set of individuals classified into different non-dominated levels (or fronts). Reproduced from [13]. ©2001 John Wiley & Sons Ltd.

Each individual in the population is assigned a ranking score RS, which is equal to the non-domination level to which they belong. The RS value is used in the crowded-comparison operator (section 5.6) to differentiate superior individuals from the inferior.

The definition of domination is reminiscent of definition 1 in section 5.1. In this case, the individuals in the first non-dominated level become Pareto optimal if they are not dominated by any other possible solutions in the objective space.

5.4 Constraint Handling

In terms of the hybrid NSGA-II, non-linear inequality constraint violation is minimized and removed by using the selection-based constraint-handling approach described in [14] and [33] for the NSGA-II, and the method in the *fminimax* SQP routine for the gradient-based local search. Since the wind-turbine blade optimization problem does not contain any equality constraints (see section 6.3), equality constraint handling is not considered. In the presence of constraints, the definition of domination in section 5.3 is modified as follows [14]:

Individual $\mathbf{x}^{(1)}$ is said to constrained-dominate $\mathbf{x}^{(2)}$, if any of the following conditions is true:

1. Individual $\mathbf{x}^{(1)}$ is feasible and $\mathbf{x}^{(2)}$ is not.
2. Individuals $\mathbf{x}^{(1)}$ and $\mathbf{x}^{(2)}$ are both unfeasible, but $\mathbf{x}^{(1)}$ has a smaller overall constraint violation.
3. Individuals $\mathbf{x}^{(1)}$ and $\mathbf{x}^{(2)}$ are feasible and $\mathbf{x}^{(1)}$ dominates $\mathbf{x}^{(2)}$.

An individual is feasible if it lies in the feasible region X, and unfeasible if it violates one or more constraints. Using the above definition, the non-dominated sorting procedure will assign any feasible individual a better ranking score than any unfeasible individual. When two individuals are unfeasible, the one with a smaller constraint violation has the better ranking score. Figure 5.4 illustrates the feasible individuals 4, 5, and 6 in the first

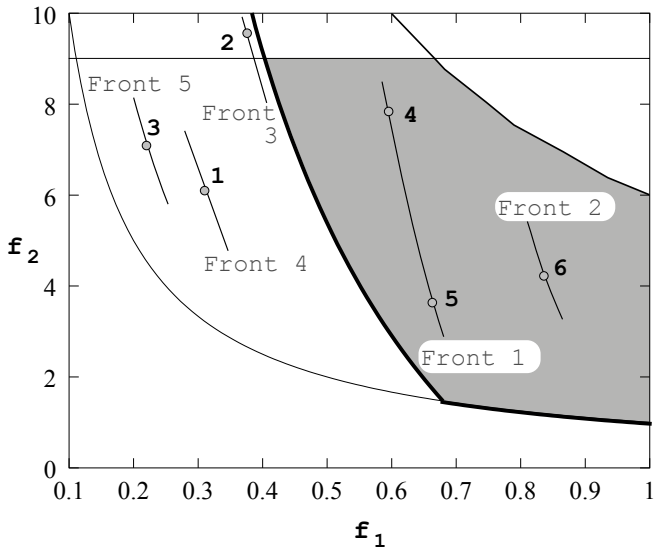

Figure 5.4: Constraint handling through selection in a bi-objective problem, where the shaded area represents the feasible region. Reproduced from [13]. ©2001 John Wiley & Sons Ltd.

and second fronts, while the unfeasible individuals in the lower fronts, for a constrained bi-objective problem.

In addition to applying the hybrid NSGA-II for analytical test functions (section 5.9) and the blade optimization (Chapter 6), the NSGA-II embedded in the MATLAB R2011a *gamultiobj* command [27] will also be used for comparison. However, *gamultiobj* does not include non-linear inequality constraint-handling capabilities needed for the blade optimization. The constraint handling in the *gamultiobj* routine consists of linear inequality and equality constraints, and boundary constraints only. Consequently, a simple penalty approach is used instead. Using the blade optimization problem as example, when a candidate blade design violates one or more non-linear inequality constraints, the penalty approach sets the objective vector $\mathbf{f}(\mathbf{x})$ to the worst possible values (i.e. AEP $= -10^{50}$ and $M_{flap,root} = m_{blade} = 10^{50}$ – see section 6.4.1). Using this method allows the algorithm within *gamultiobj* to discard unfeasible blade designs without having to modify the coding, which is necessary for the selection-based approach. The crossover and mutation operators in the NSGA-II and *gamultiobj* as well as the *fminimax* SQP routine always satisfy the boundary constraints. The

constraint handling procedure in the hybrid NSGA-II has been verified using constrained analytical test functions [14, 94, 95].

5.5 Crowding-Distance Measurement

The crowding distance (CD) measurement used in the crowded-comparison operator (section 5.6) is described here. Following the non-dominated sorting of R_l (step 7 – section 5.2), the individuals in each front ($\mathcal{F}_i$, where $i = 1, 2, \ldots,$ etc.) are sorted according to each objective function z_i, in ascending order of magnitude. The individuals with the smallest ($z_i^{\min}$) and largest ($z_i^{\max}$) objective-function values are then assigned an infinite CD. All intermediate individuals j, are assigned a CD equal to the absolute normalized difference in objective-function values of two adjacent individuals $(j+1)$ and $(j-1)$. This procedure is repeated for each z_i. The overall CD for each individual CD^j, is then obtained by aggregating the CD from all z_i. Equation (5.4) gives the CD calculation for intermediate individuals:

$$CD^j = \sum_{i=1}^{q} \left| \frac{z_i^{(j+1)} - z_i^{(j-1)}}{z_i^{\max} - z_i^{\min}} \right| \tag{5.4}$$

The CD computation is illustrated in Figure 5.5 for a bi-objective problem, where i is an intermediate individual (i.e. $i = j$). The individuals marked in filled circles belong to the same front, in this case $\mathcal{F}_1$. The boundary individuals $\mathcal{F}_1(0)$ and $\mathcal{F}_1(l)$, have an infinite CD, while intermediate individuals are assigned a CD according to equation 5.4. In Figure 5.5, the CD^j represents half of the perimeter of the cuboid formed by the neighbouring individuals $(j+1)$ and $(j-1)$.

5.6 Crowded-Comparison Operator

In the NSGA-II, the crowded-comparison operator is combined with binary tournament selection to guide the selection of individuals towards a uniformly spread Pareto-optimal

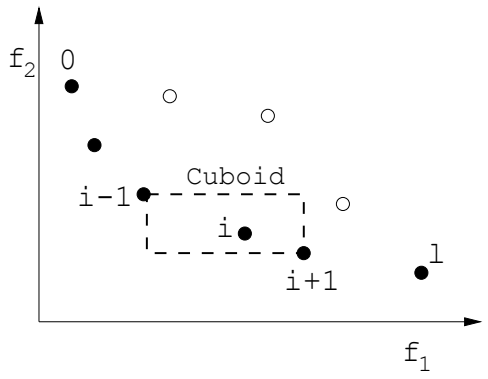

Figure 5.5: Crowding-distance calculation. Individuals marked in filled circles are on the same front. Reproduced from [14]. ©2002 IEEE.

set. Binary tournament selection as described in section 2.4.2, is when the best individual from a number (typically 2, hence binary) of randomly chosen distinct individuals from the population becomes a parent. Binary tournament selection is repeated until the number of parents returned is equal to the size of the mating pool, which is then subjected to crossover and mutation to create children for the generation. The crowding distance (CD) is used as a measure of diversity, described in section 5.5, when determining the best individual. Assume each individual i, in the population contains two quantities: 1) ranking score (RS^i) and 2) crowding distance (CD^i). The crowded-comparison operator ($\prec_n$) for two individuals i and j, is as follows:

$$
\begin{aligned}
& i \prec_n j, \\
& \text{if } RS^i < RS^j, \\
& \text{or } RS^i = RS^j \text{ and } CD^i > CD^j.
\end{aligned}
$$

In other words, between two individuals with different ranking scores, the individual with the lower ranking score is preferred (or the individual belonging to a better front). If the ranking score between the two individuals are the same, then the individual that is the least crowded (higher CD) is preferred.

5.7 Crossover

As explained in section 2.4, the crossover operator combines the decision vectors of two or more parents when creating children for the next generation. Among the many crossover operators available, only the intermediate and scattered crossover will be discussed in detail. A third crossover operator traditionally used in the NSGA-II is the simulated binary crossover (SBX) [36]. Of all the crossover operators in the *gamultiobj* routine and SBX, the SBX was able to produce the best spread of solutions for analytical test functions (see section 5.9). The crossover fraction (see Tables 5.1 and 6.3), is the probability that the two or more parents will crossover.

5.7.1 Intermediate Crossover

Intermediate crossover is the default crossover operator in the MATLAB R2011a *gamultiobj* routine. Given two parents $\mathbf{x}^{(1)}_{Parent}$ and $\mathbf{x}^{(2)}_{Parent}$, the operator creates children $\mathbf{x}^{(1)}_{Child}$ and $\mathbf{x}^{(2)}_{Child}$, using the following formula:

$$\mathbf{x}_{Child} = \mathbf{x}^{(1)}_{Parent} + u_o(\mathbf{x}^{(2)}_{Parent} - \mathbf{x}^{(1)}_{Parent}) \tag{5.5}$$

where u_o is a uniformly distributed pseudo-random number between 0 and 1. Figure 5.6 illustrates intermediate crossover for two arbitrary parents $\mathbf{x}^{(1)}_{Parent}$ and $\mathbf{x}^{(2)}_{Parent}$, where $u_o = 0.9$ and $u_o = 0.3$ produces $\mathbf{x}^{(1)}_{Child}$ and $\mathbf{x}^{(2)}_{Child}$ respectively.

$\mathbf{x}^{(1)}_{Parent} =$	0.5	0.2	0.9	0.1	0.7	$\mathbf{x}^{(1)}_{Child} =$	0.95	1.82	2.79	3.61	4.57
$\mathbf{x}^{(2)}_{Parent} =$	1	2	3	4	5	$\mathbf{x}^{(2)}_{Child} =$	0.65	0.74	1.53	1.27	1.99

Figure 5.6: Intermediate crossover for two arbitrary parents $\mathbf{x}^{(1)}_{Parent}$ and $\mathbf{x}^{(2)}_{Parent}$, where $u_o = 0.9$ and $u_o = 0.3$ produces two children $\mathbf{x}^{(1)}_{Child}$ and $\mathbf{x}^{(2)}_{Child}$, respectively.

5.7.2 Scattered Crossover

Scattered crossover, also known as uniform crossover, creates a random binary vector where the probability of each element in the vector being 0 or 1 is typically 50%. The decision variables in the decision vectors of two parents $\mathbf{x}^{(1)}_{Parent}$ and $\mathbf{x}^{(2)}_{Parent}$, are then exchanged according to the elements equal to 0 in the binary vector. The end result are two distinct children $\mathbf{x}^{(1)}_{Child}$ and $\mathbf{x}^{(2)}_{Child}$. Figure 5.7 displays scattered crossover for two arbitrary parents $\mathbf{x}^{(1)}_{Parent}$ and $\mathbf{x}^{(2)}_{Parent}$, producing $\mathbf{x}^{(1)}_{Child}$ and $\mathbf{x}^{(2)}_{Child}$.

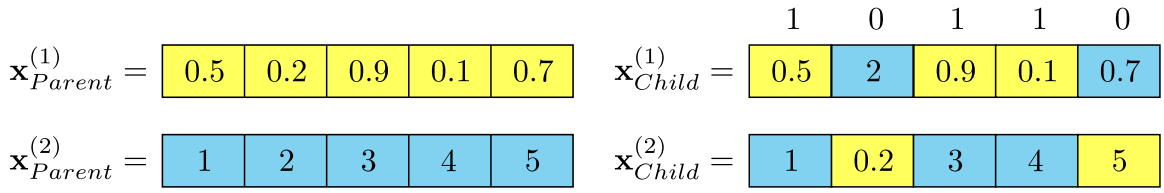

Figure 5.7: Scattered crossover for two arbitrary parents $\mathbf{x}^{(1)}_{Parent}$ and $\mathbf{x}^{(2)}_{Parent}$, producing two distinct children $\mathbf{x}^{(1)}_{Child}$ and $\mathbf{x}^{(2)}_{Child}$.

5.8 Mutation

Following crossover, the mutation operator ensures that each child is unique by slightly altering (or mutating) the child's decision vector. Depending on the degree, mutation maintains the diversity of the population. The polynomial mutation [37] operator using a variable mutation probability p_m, is described here. In this operator, a polynomial probability distribution is used to create the variable of a mutated child $x_{Mut.Child}$, in the vicinity of the original variable x_{Child}. The following procedure is implemented to determine $x_{k,Mut.Child}$ subject to upper (x^U_k) and lower (x^L_k) bounds for $k = 1, 2, \ldots, n$ [33]:

1. Create a random number u_o between 0 and 1.

2. Calculate the parameter $\bar{\zeta}$ using:

$$\bar{\zeta} = \begin{cases} [2u_o + (1-2u_o)(1-\zeta)^{\eta_m+1}]^{1/(\eta_m+1)} - 1, & \text{if } u_o \leq 0.5, \\ 1 - [2(1-u_o) + 2(u_o - 0.5)(1-\zeta)^{\eta_m+1}]^{1/(\eta_m+1)}, & \text{otherwise,} \end{cases}$$

where $\zeta = \min[(x_{k,Child} - x_k^L), (x_k^U - x_{k,Child})]/(x_k^U - x_k^L)$.

3. Calculate the mutated child using:

   $x_{k,Mut.Child} = x_{k,Child} + \bar{\zeta}(x_k^U - x_k^L)$.

The variance of the polynomial probability distribution (or mutation intensity) is a function of the distribution index η_m, which is a user-defined parameter that is strictly positive.

5.9 Verification using Analytical Test Function

Before applying the hybrid algorithm for wind-turbine blade optimization, its performance on analytical test functions from the ZDT [96] and DTLZ [95] test suites was investigated. For brevity, the results for only the DTLZ2 test function will be shown here. DTLZ2 is scalable in both the number of objectives and the number of variables, and does not contain any equality or inequality constraints. The number of objectives and variables chosen are $q = 3$ and $n = 20$ respectively, which matches comparatively to the wind-turbine blade optimization problem. The three-objective DTLZ2 is expressed by:

$$\begin{aligned} \text{minimize} \quad & f_1(\mathbf{x}) = \left(1 + \sum_{i=3}^{20}(x_i - 0.5)^2\right)\cos\left(\frac{\pi}{2}x_1\right)\cos\left(\frac{\pi}{2}x_2\right) \\ & f_2(\mathbf{x}) = \left(1 + \sum_{i=3}^{20}(x_i - 0.5)^2\right)\cos\left(\frac{\pi}{2}x_1\right)\sin\left(\frac{\pi}{2}x_2\right) \\ & f_3(\mathbf{x}) = \left(1 + \sum_{i=3}^{20}(x_i - 0.5)^2\right)\sin\left(\frac{\pi}{2}x_1\right) \end{aligned} \tag{5.6}$$

$$\begin{aligned} \text{subject to} \quad & \mathbf{x} \in X \\ & X = \{\mathbf{x} \in \mathbb{R}^{20} | \\ & \qquad 0 \leq x_k \leq 1, k = 1, \ldots, 20\} \end{aligned}$$

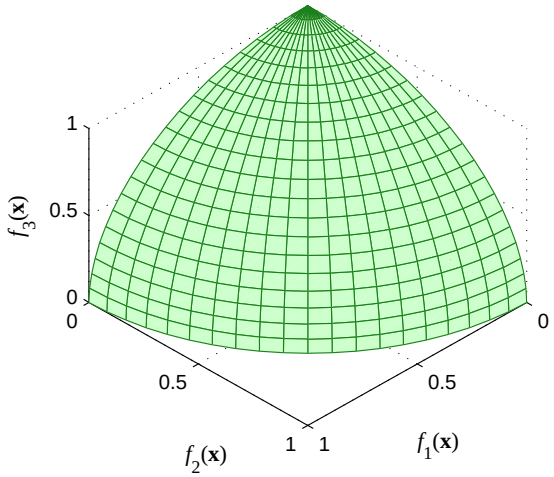

Figure 5.8: Three-objective DTLZ2 Pareto front ($|PF_{true}| = 441$ shown for clarity). Retrieved from [3].

and its Pareto front is shown in Figure 5.8.

In the current study, the performance of an algorithm for multi-objective optimization is focussed on convergence. Hence, the generational distance (GD) [97] metric is used to compare different algorithms. The GD metric measures the mean Euclidean distance in the objective space between each solution and its nearest Pareto-optimal solution in the true Pareto front (PF_{true}). The PF_{true} shown in Figure 5.8 was derived from 441 perfectly spread Pareto-optimal solutions. When the solutions from an algorithm lie exactly on the Pareto-optimal solutions of PF_{true}, the GD will have the optimal value of zero. This seldom occurs because the heuristics prevent a perfectly-spread and fully-converged set of solutions. As shown for two MOEAs in Figure 5.10, the solutions are randomly distributed and are situated at varying distances from PF_{true}. Therefore, the aim is to attain the minimum GD value in as few objective-function evaluations as possible rather than achieving GD = 0. When assessing the convergence, it is common practice to calculate the mean GD based on multiple runs to account for the heuristic effects. Furthermore, since the accuracy of the GD is dependent on the resolution of PF_{true}, a large number (i.e. $|PF_{true}| = 10,000$) should be used for GD calculations. The worst (max) and best (min) runs define a max-min interval,

which is used for assessing the range in possible GD.

The mean GD versus the number of objective-function evaluations from 10 runs is plotted for four algorithms in Figure 5.9. For illustrations of GD max-min intervals pertaining to the four algorithms, refer to Appendix B. Here, the evaluation of all objective-functions in the objective vector is considered as one objective-function evaluation. Two of the four algorithms consist of the NSGA-II as described in section 5.2 with and without the gradient-based local search. The *gamultiobj* command with improved and default parameter settings comprises the remaining two algorithms. Attempts were made to determine the parameters (such as the crossover and mutation operators) that resulted in the best possible convergence for *gamultiobj*. Accordingly, identical parameters were used for the hybrid and non-hybrid NSGA-II whenever possible for a fair comparison. A summary of the algorithms and parameter settings are given in Table 5.1.

Figure 5.9 clearly shows that the hybrid NSGA-II outperforms all other algorithms with respect to the GD metric. The inclusion of gradient-based local search has successfully reduced the number objective-function evaluations needed to reach the minimum GD value by more than 50% in comparison to the regular NSGA-II. Figure 5.10 displays the objective vectors obtained from the hybrid and non-hybrid NSGA-II at 10,000 objective-function evaluations. Although the hybrid produces solutions closer to PF_{true}, the difference in the GD values between the two algorithms is small. It is observed from Figure 5.10 that the reduction in objective-function evaluations is attributed to the fine-tuning capabilities of gradient-based local search that the regular NSGA-II lacks. For this particular test function, executing *gamultiobj* using its default settings yields poor convergence. Similar results for the four algorithms have been obtained for other ZDT and DTLZ test functions. Based on these results, it is in the authors' interest to achieve the same reduction in objective-function evaluations for the wind-turbine blade optimization problem as well.

Table 5.1: Summary of algorithms and parameter settings for DTLZ2 test function. Retrieved from [3].

	hybrid NSGA-II	NSGA-II	*gamultiobj*	*gamultiobj* (default)
Population size (N_{pop})	200	200	200	200
Selection	binary tournament	binary tournament	binary tournament	binary tournament
Crossover	scattered[a]	scattered[a]	scattered[a]	intermediate
Crossover fraction	0.9[b]	0.9	0.9	0.8
Mutation	polynomial	polynomial	adaptive feasible	adaptive feasible
Mutation probability	0.001[b]	0.001	–	–
Mutation index	20[b]	20	–	–
Pareto fraction[c]	1	1	1	0.35
Spread maintenance	clustering approach	clustering approach	crowding routine	crowding routine

[a]Also known as uniform.
[b]As suggested by Sindhya et al. [57].
[c]Controls elitism, see section 2.4.1.

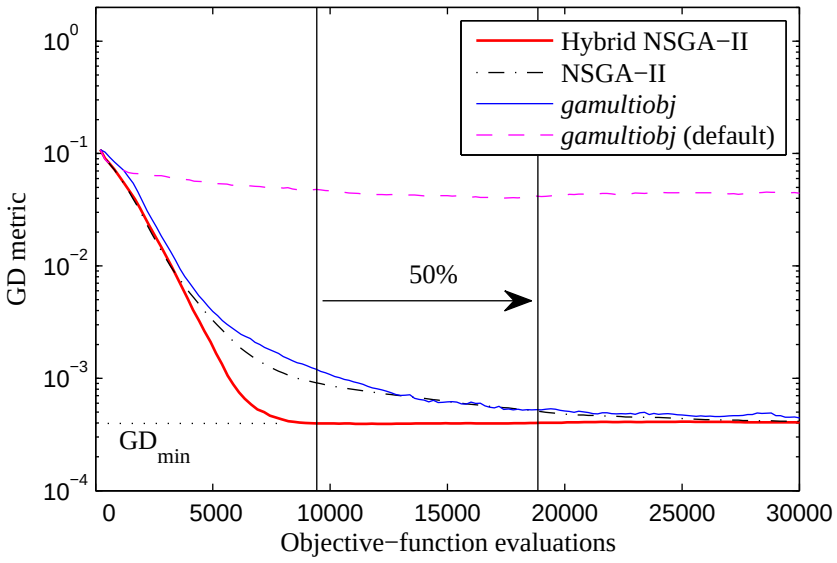

Figure 5.9: Algorithm convergence for the three-objective DTLZ2 test function using $|PF_{true}| = 10,000$ and 10 runs for GD calculation. Retrieved from [3].

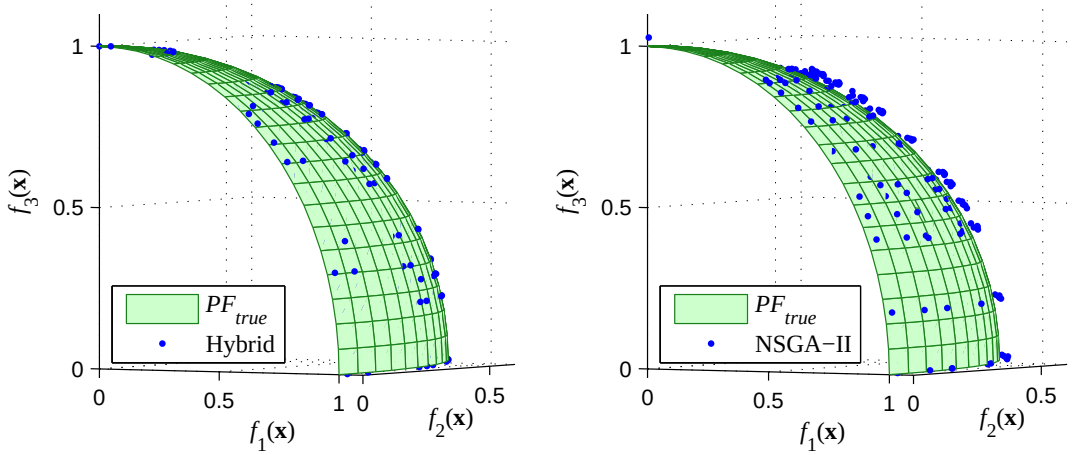

Figure 5.10: Comparison of computed results between hybrid (left) and non-hybrid (right) NSGA-II at 10,000 objective-function evaluations ($|PF_{true}| = 441$ shown for clarity). Retrieved from [3].

Chapter 6

MULTI-OBJECTIVE OPTIMIZATION OF NREL 5 MW TURBINE

6.1 Variables

Before presenting the objective functions determined by the aerodynamic and structural models, the variables involved in the optimization are described briefly. Bézier curves that are manipulated by control points (CPs) define the blade twist and chord (c) distributions (Figure 6.1(a)–(b)), and the non-dimensional radial locations (r/R) of the master airfoils ($\gamma_{airfoil}$) for the relative thickness (t/c) distribution (Figure 6.1(c)). The master airfoils are a set of key airfoils used to interpolate the lift and drag coefficients, and profile coordinates for the entire blade. The master airfoils for the illustrative case of the NREL 5 MW blade optimization are given in Table 6.1 and plotted in Figures C.1 to C.3. In Figure 6.1(b), the root chord is iterated such that a monotonically-decreasing dimensional thickness is obtained, as shown in Figure 6.1(d). The dimensional thickness is the product of the relative thickness and the chord. The CPs and distributions are shown in Figure 6.1 for an arbitrary blade.

The methodology used to define the blade shape follows that of Sale's HARP_Opt code [98] closely with two main exceptions: 1) the number of CPs for the twist and chord distributions outboard of the maximum chord position is adjustable, and 2) a piecewise cubic hermite interpolating polynomial is used to interpolate the relative thickness across the master airfoils between the root and tip. Exception 1) provides the user a choice of the number of CPs used and 2) is a simpler approach. For exception 2), HARP_Opt involves a linkage between a cubic polynomial fit and a piecewise-linear distribution subject to slope requirements at the endpoints. The reader is referred to [98] for a detailed description of the

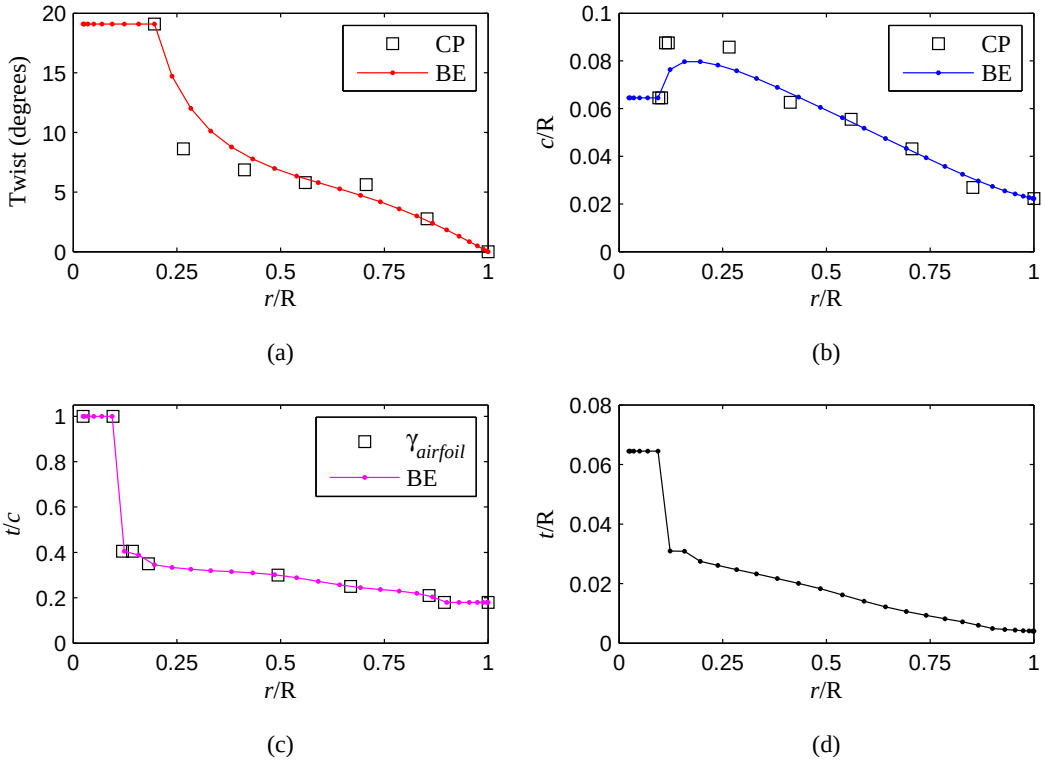

Figure 6.1: Control points (CPs) and $\gamma_{airfoil}$ determine the blade element (BE) values for twist (a), chord (b), and thickness distributions (c)–(d). Retrieved from [3].

optimization variables.

The decision vector $\mathbf{x}$ is given by:

$$\begin{aligned}\mathbf{x} = (&\mathrm{CP}_{1,twist}, \mathrm{CP}_{2,twist}, \ldots, \mathrm{CP}_{N_u,twist},\\ &\mathrm{CP}_{1,chord}, \mathrm{CP}_{2,chord}, \ldots, \mathrm{CP}_{N_v,chord},\\ &\gamma_{1,airfoil}, \gamma_{2,airfoil}, \ldots, \gamma_{N_w,airfoil})\end{aligned} \tag{6.1}$$

where the number of CPs for the twist and chord are N_u and N_v respectively, and N_w is the number of master airfoils plus one.

6.2 Objective Functions

A total of three objective functions are simultaneous optimized to achieve the Pareto-optimal set of blade designs. Two objective functions are obtained from the aerodynamic model (Chapter 3) which are:

$$\text{maximize} \quad \mathrm{AEP} = 8760 \int_{V_{o,cut\text{-}in}}^{V_{o,cut\text{-}out}} P(V_o, \theta, \lambda) f(V_o)\, dV_o, \tag{6.2}$$

$$\text{minimize} \quad M_{flap,root} = \int_{r_{hub}}^{R} r p_n(r)\, dr. \tag{6.3}$$

Equation (6.2) is the equivalent of equation (1.4), and as already explained in section 1.4, 8760 is the number of turbine operating hours per year, $P(V_o, \theta, \lambda)$ is the rotor power obtained from the power curve (Figure 3.10(a)), and $f(V_o)$ is the wind speed probability, the Rayleigh probability density function. Here, a maximization of the AEP is performed by minimizing the negative value of its objective function. The second objective function (equation (6.3)) is to minimize the peak flapwise root-bending moment $M_{flap,root}$, obtained from the thrust curve (Figure 3.10(b)) and is expected to improve the blade fatigue life. This objective is similar to the constraint imposed on the aero-elastic (time-dependent) computations in Fuglsang [22], where the mean $M_{flap,root}$ at the wind speed corresponding to maximum power was not allowed to exceed a specified value. From Fuglsang's work, fatigue loads were shown

to vary linearly with the mean $M_{flap,root}$. In this thesis however, only static (or steady) computations are performed. It is assumed here that minimizing $M_{flap,root}$ in the static sense is the equivalent of minimizing the mean $M_{flap,root}$ in the aero-elastic case.

The third objective function is calculated from the structural model (Chapter 4) given by:

$$\text{minimize} \quad m_{blade} = \int_{r_{hub}}^{R} m \, dr. \tag{6.4}$$

where m is the linear mass of a blade element and m_{blade} is the blade's total mass.

6.3 Constraints

There are two types of constraints involved in the optimization of the wind-turbine blade. The first type are non-linear inequality constraints and the second are boundary constraints. The inequality constraints are equations (4.45) and (4.46), and equations (6.7) to (6.9). The strain and tip deflection constraints given by equations (4.45) and (4.46) are reiterated as follows:

$$(\max[\varepsilon_{1,max}, \varepsilon_{2,max}] - \varepsilon_{max})/\varepsilon_{max} \leq 0, \tag{6.5}$$

$$(\delta^{tip}_{flap} - \delta_{max})/\delta_{max} \leq 0. \tag{6.6}$$

During the optimization, the chord has a tendency to approach very large values to maximize the AEP. To prevent this from occurring, equation (6.7) is included that forces candidate blades to have a planform area (A) less than or equal to that of the original blade design (A_o):

$$(A_o - A)/A_o \leq 0. \tag{6.7}$$

Equation (6.7) may be unnecessary for two reasons: 1) more restricted boundary limits on the chord (see equation (6.11)) can be used to achieve the same purpose and 2) the increase in chord is counteracted by the m_{blade} minimization. Here, the planform area constraint is added as an additional precaution to ensure that the optimal blades have feasible geometries

and are comparable to each other [99]. The remaining set of inequality constraints given by:

$$(f_{i,min}(\mathbf{x}) - f_i(\mathbf{x}))/f_{i,min}(\mathbf{x}) \leq 0, \tag{6.8}$$

$$(f_i(\mathbf{x}) - f_{i,max}(\mathbf{x}))/f_{i,max}(\mathbf{x}) \leq 0 \tag{6.9}$$

prevents a multi-objective optimization algorithm from searching an excessively large region of the objective space. In other words, we are only interested in blade designs that are in the vicinity of the original. For the blade optimization considered here, AEP, $M_{flap,root}$, and m_{blade} are constrained to be within $\pm 5\%$, $\pm 40\%$ and $\pm 40\%$ from the original respectively. All inequality constraints (equations (6.5)to (6.9)) are normalized to prevent bias from any particular constraint.

The second type, the boundary constraints expressed by equations (6.10) to (6.12), involve limiting the CPs for the twist and chord, and $\gamma_{airfoil}$:

$$\mathrm{CP}^L_{u,twist} \leq \mathrm{CP}_{u,twist} \leq \mathrm{CP}^U_{u,twist}, \tag{6.10}$$

$$\mathrm{CP}^L_{v,chord} \leq \mathrm{CP}_{v,chord} \leq \mathrm{CP}^U_{v,chord}, \tag{6.11}$$

$$\gamma^L_{w,airfoil} < \gamma_{w,airfoil} < \gamma^U_{w,airfoil} \tag{6.12}$$

where $u = 1, \ldots, N_u$, $v = 1, \ldots, N_v$, and $w = 1, \ldots, N_w$. In practice, the limits are derived from the transportability and manufacturing requirements. For example, a blade cannot be transported on a truck if it exceeds a maximum chord length. Such requirements are not considered here and as a result, a wide range of boundary values to ensure a variety of blade designs is implemented instead.

In addition to the constraints discussed above, limits are imposed in the control and regulation strategy (section 3.4). For example, excessive turbine-generated noise is avoided by including a limit on the tip speed (ωR) and the power is constrained to be less than or equal to P_{rated}. These constraints are treated by selecting the appropriate value of C_P for each V_o in the aerodynamic model, and not by the constraint handling techniques discussed in section 5.4.

6.4 Wind-Turbine Blade Optimization

6.4.1 Optimization Problem

We restate problem (5.1) in terms of the wind-turbine blade optimization problem. Following the suggestions in [100], equations (6.2), (6.3) and (6.4) are used in the objective vector $\mathbf{f}(\mathbf{x})$. The decision vector is given by equation (6.1), and the inequality and boundary constraints in the feasible region X are equations (6.5) to (6.9), and equations (6.10) to (6.12) respectively. Since the competitiveness of wind energy against other energy sources depends mostly on cost, minimizing the cost (or COE) has typically been considered as an objective function (e.g. [22, 23, 26, 34, 43]). However, the cost of a turbine is difficult to calculate and assumptions are often made for simplification. In [23, 26] and [43], the cost depends on the blade (or rotor) only. When determining the blade cost, mass is used as a parameter ([26, 43]). Here, m_{blade} is assumed to be well correlated to cost. Detailed cost models can be found in [22] and [34], which consider several components including rotor, tower, gearbox and generator, as well as other costs such as operation and maintenance.

The NREL offshore 5 MW baseline wind-turbine blade is selected as an initial design for optimization and its basic properties are shown in Table 6.1 [4]. The structural layup and material properties are not provided in [4], thus the structural layup and material properties described in section 4.2.1 are applied instead. The twist, chord and thickness distributions for the NREL 5 MW blade are displayed in Figure 6.5. For the results given in the following section, 30 blade elements ($N = 30$) and 21 design variables ($N_u = 6$, $N_v = 7$ and $N_w = 8$) were used. Constraint values set in the blade optimization are summarized in Table 6.2.

6.4.2 Results and Discussion

In contrast to test functions such as those discussed in section 5.9, PF_{true} cannot be derived for the wind-turbine blade optimization problem. As a result, before determining the convergence of the algorithms, an approximation of PF_{true} is necessary to calculate the GD

Table 6.1: Basic NREL 5 MW wind-turbine properties. Retrieved from [4].

Rating (MW)	5
Number of blades	3
R (m)	63
$V_{cut\text{-}in}$ (m/s)	3
$V_{cut\text{-}out}$ (m/s)	25
Rated tip speed (m/s)	80
Master airfoils	Cylinder (1.0),
(t/c in parentheses)	DU40 (0.405), DU35 (0.35),
	DU30 (0.30), DU25 (0.25),
	DU21 (0.21), NACA64 (0.18)

Table 6.2: Summary of constraint values used in NREL 5 MW blade optimization.

Property	Value	Property	Value	Property	Value
ε_{max}	$2580\,\mu\varepsilon$	$f_{1,min}(\mathbf{x})$	$0.95\text{AEP}^{\text{NREL}}$	$\text{CP}^{L}_{u,twist}, u = 1,\ldots,N_u$	$0°$
δ_{max}	5.272 m	$f_{2,min}(\mathbf{x})$	$0.60M^{\text{NREL}}_{flap,root}$	$\text{CP}^{U}_{u,twist}, u = 1,\ldots,N_u$	$20°$
A_o	$213.9\,\text{m}^2$	$f_{3,min}(\mathbf{x})$	$0.60m_{blade}$	$\text{CP}^{L}_{v,chord}, v = 1,\ldots,N_v$	0.002
		$f_{1,max}(\mathbf{x})$	$1.05\text{AEP}^{\text{NREL}}$	$\text{CP}^{U}_{v,chord}, v = 1,\ldots,N_v$	0.111
		$f_{2,max}(\mathbf{x})$	$1.40M^{\text{NREL}}_{flap,root}$	$\gamma^{L}_{w,airfoil}, w = 1,\ldots,N_w$	0
		$f_{3,max}(\mathbf{x})$	$1.40m_{blade}$	$\gamma^{U}_{w,airfoil}, w = 1,\ldots,N_w$	0.85/1[a]

[a] A combination of 0.85 and 1 used for $\gamma^{U}_{w,airfoil}$.

metric. This can be achieved by executing a multi-objective optimization that results in a well-spread and fully-converged Pareto-optimal set. An accurate GD calculation also requires that the size of the Pareto-optimal set is large. In an attempt to meet these requirements using the computational resources available, PF_{true} is approximated by executing the algorithm described in section 5.2, without the gradient-based local search, for as many ($l = 110$) iterations as possible and with a large population size ($N_{pop} = 1000$). The result of the approximation is shown in Figure 6.2. In Figure 6.2, a Pareto-optimal solution (PO–star) with the same m_{blade} as the NREL 5 MW blade (circle) is also plotted. The PO has a 1.8% increase in AEP and 4.7% decrease in $M_{flap,root}$ with respect to the NREL 5 MW turbine. Consequently, not only has the algorithm successfully optimized the initial design for more than one objective, but it has also provided a complete set of optimal trade-off solutions as illustrated

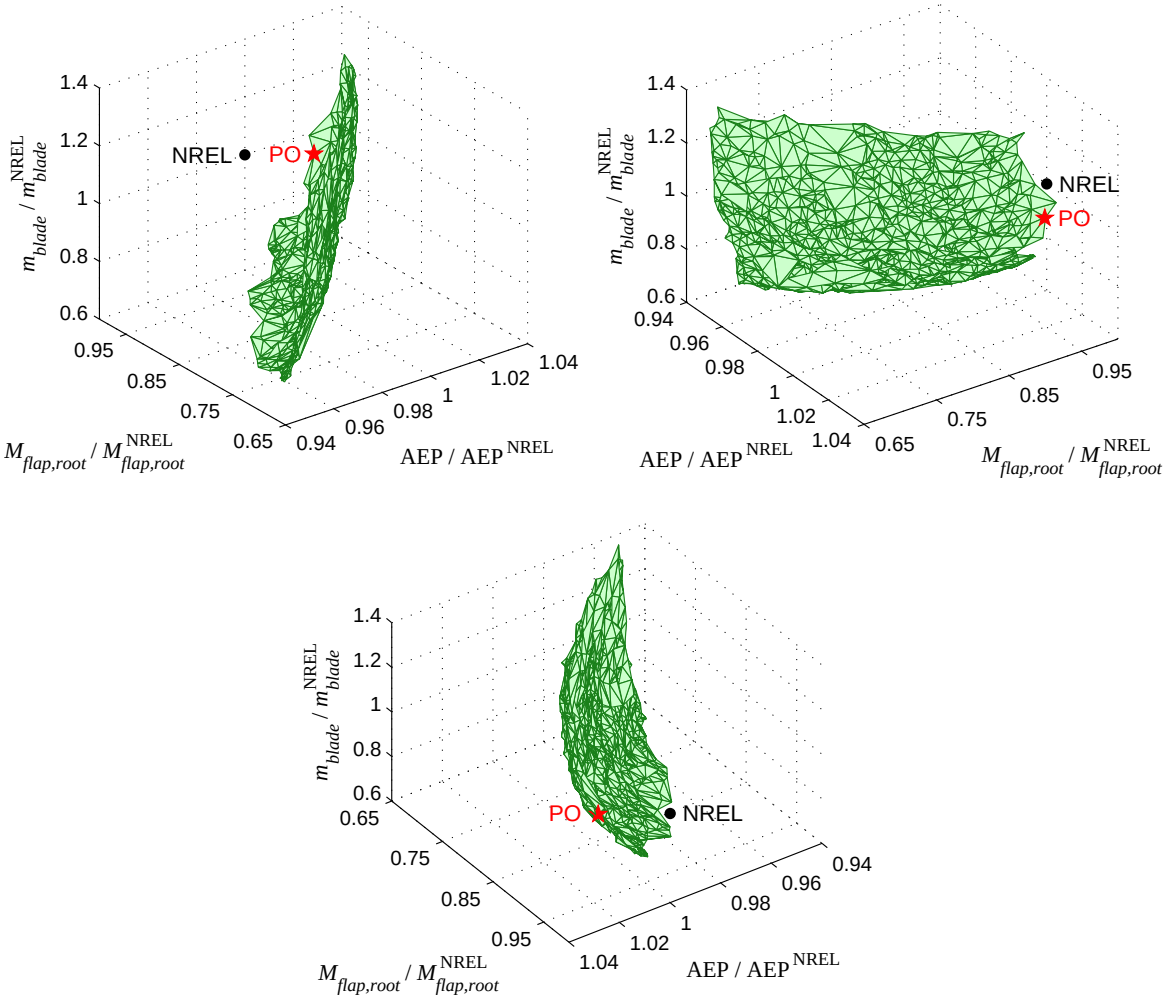

Figure 6.2: Rotated views of the Pareto front for the NREL 5 MW blade optimization including NREL 5 MW blade (circle) and a Pareto-optimal solution (PO–star). Retrieved from [3].

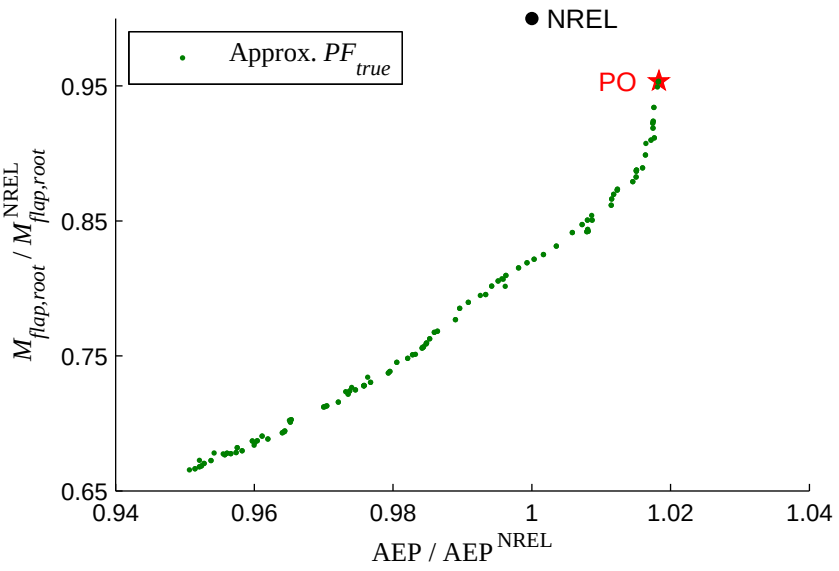

Figure 6.3: 2D slice in AEP/AEP$^{\text{NREL}}$–$M_{flap,root}/M_{flap,root}^{\text{NREL}}$ plane where $m_{blade}/m_{blade}^{\text{NREL}} = 1$ for NREL 5 MW blade optimization including NREL 5 MW blade (circle) and a Pareto-optimal solution (PO–star).

by the surface in Figure 6.2. As discussed in section 6.3, the Pareto-optimal set is, however, bounded by the inequality constraints on the objective space (equations (6.8) and (6.9)). Figures 6.3 and 6.4 display the NREL blade on the AEP/AEP$^{\text{NREL}}$–$M_{flap,root}/M_{flap,root}^{\text{NREL}}$ and $M_{flap,root}/M_{flap,root}^{\text{NREL}}$–$m_{blade}/m_{blade}^{\text{NREL}}$ planes where $m_{blade}/m_{blade}^{\text{NREL}} = 1$ and AEP/AEP$^{\text{NREL}} = 1$ respectively. Pareto-optimal solutions on the AEP/AEP$^{\text{NREL}}$–$m_{blade}/m_{blade}^{\text{NREL}}$ plane where $M_{flap,root}/M_{flap,root}^{\text{NREL}} = 1$ do not exist, and hence is not shown.

A comparison of the twist, chord and thickness distributions for PO and the NREL 5 MW blade are shown in Figure 6.5. It is observed that the twist (Figure 6.5(a)) and chord (Figure 6.5(b)) near the root section for PO both reach their maximum allowable values set by the boundary constraints in equations (6.10) and (6.11). Conversely, there is a decrease in thickness (Figure 6.5(c)–(d)) near the root but an increase at about $r/R = 0.7$ instead. A decrease in chord also occurs between the mid-span and blade tip. The step in relative thickness from $t/c = 0.25$ (DU25) to $t/c = 0.18$ (NACA64) at about $r/R = 0.85$ in Figure 6.8(c) is because of an upper boundary constraint $\gamma_{w,airfoil}^{U}$, imposed on the DU

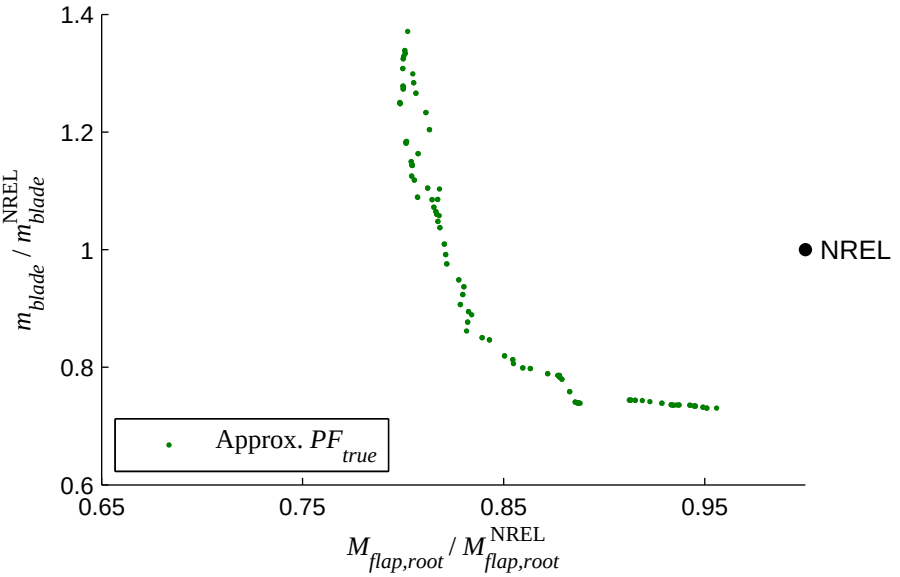

Figure 6.4: 2D slice in $M_{flap,root}/M_{flap,root}^{\mathrm{NREL}}$–$m_{blade}/m_{blade}^{\mathrm{NREL}}$ plane where $\mathrm{AEP}/\mathrm{AEP}^{\mathrm{NREL}} = 1$ for NREL 5 MW blade optimization including NREL 5 MW blade (circle).

master airfoils, which was set to 0.85 in the blade optimization. Figures 6.6 and 6.7 depict the blade geometries in different views for the NREL 5 MW and PO respectively.

Figure 6.8 displays the power and thrust curves, as well as the pitch and RPM schedules for the NREL 5 MW blade and PO. Although barely noticeable, the increase in AEP for PO is shown in Figure 6.8(a), where PO produces more power for all wind speeds up to V_{rated}. The increase in power is attributed to PO's improved value of $C_{P,opt} = 0.5022$ in comparison to $C_{P,opt} = 0.4841$ of the NREL 5 MW blade at the variable-speed region (i.e. region I in Figure 3.10). This translates to an improvement of 3.73% in $C_{P,opt}$. The decrease in $M_{flap,root}$ for PO is demonstrated in Figure 6.8(b), where the peak thrust is lower than the NREL 5 MW blade. In Figure 6.8(c) for PO, $C_{P,opt}$ corresponds to a lower pitch angle ($\theta_{opt} = -1.4°$), and the maximum allowable tip speed ($\omega R = 80\,\mathrm{m/s}$) is reached at a lower wind speed ($V_o = 9.8\,\mathrm{m/s}$). For the NREL 5 MW blade, $\theta_{opt} = 0°$ and $V_o = 10.4\,\mathrm{m/s}$ when $\omega R = 80\,\mathrm{m/s}$ (Figure 6.8(d)).

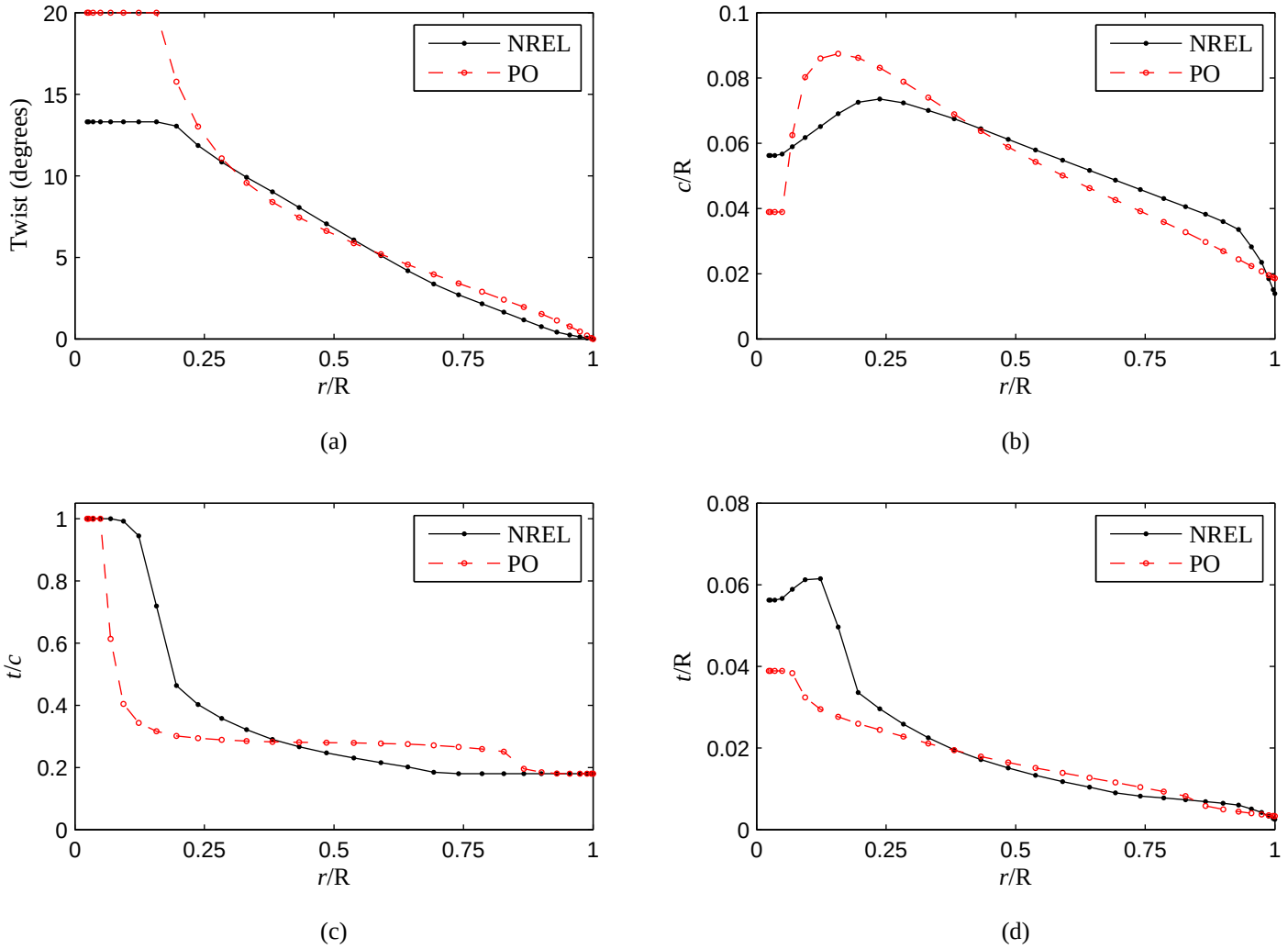

Figure 6.5: Blade element twist (a), chord (b), and thickness (c)–(d) distributions for the NREL 5 MW blade and a Pareto-optimal (PO) solution. Retrieved from [3].

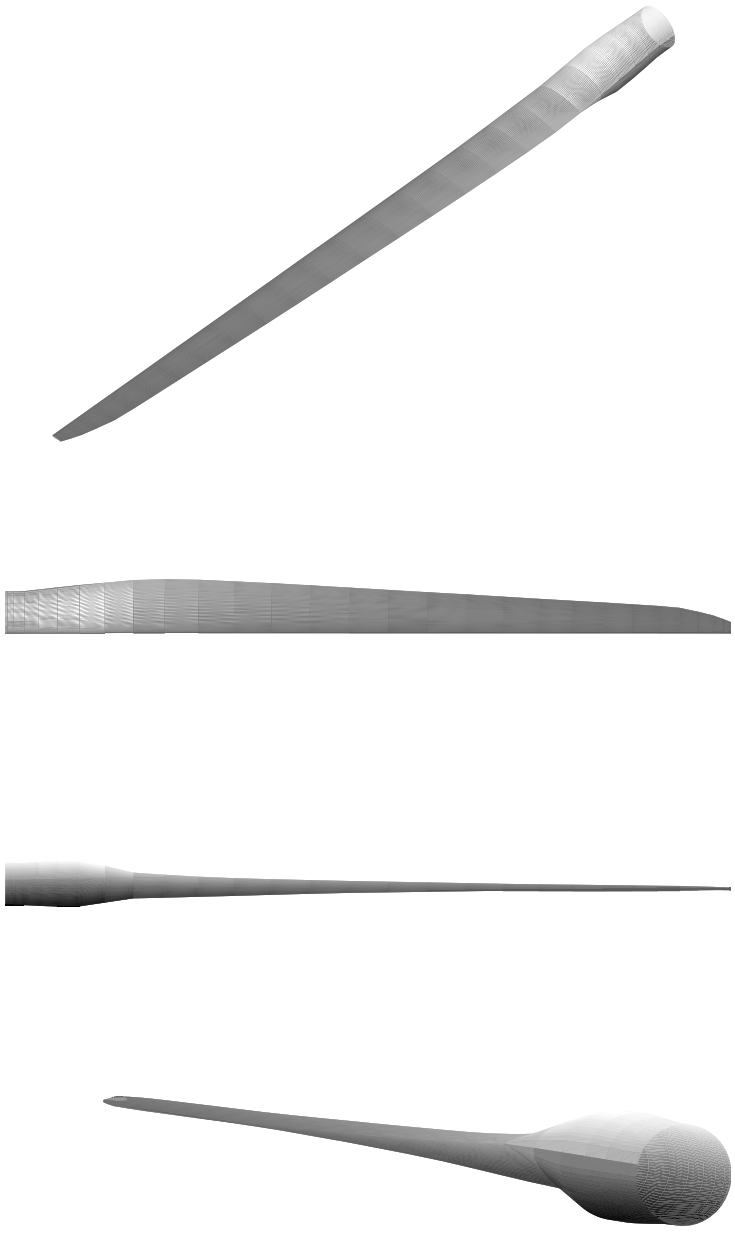

Figure 6.6: Blade geometry views of NREL 5 MW.

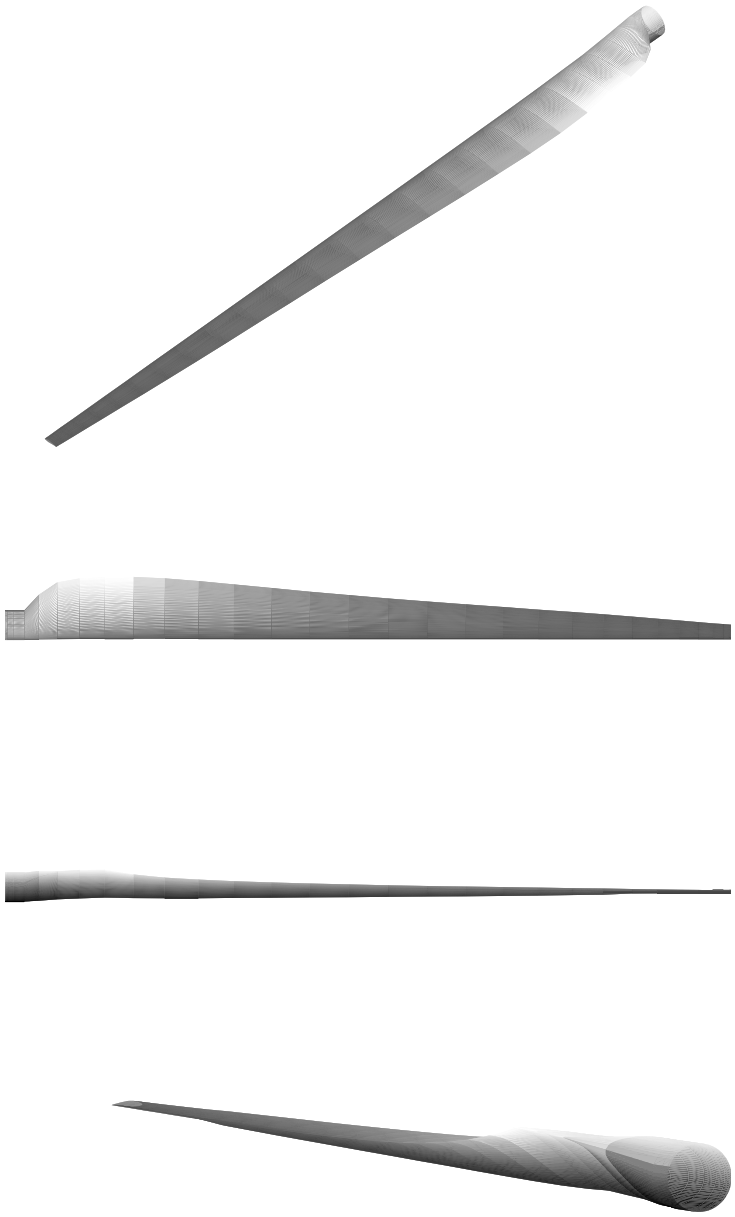

Figure 6.7: Blade geometry views of a Pareto-optimal solution.

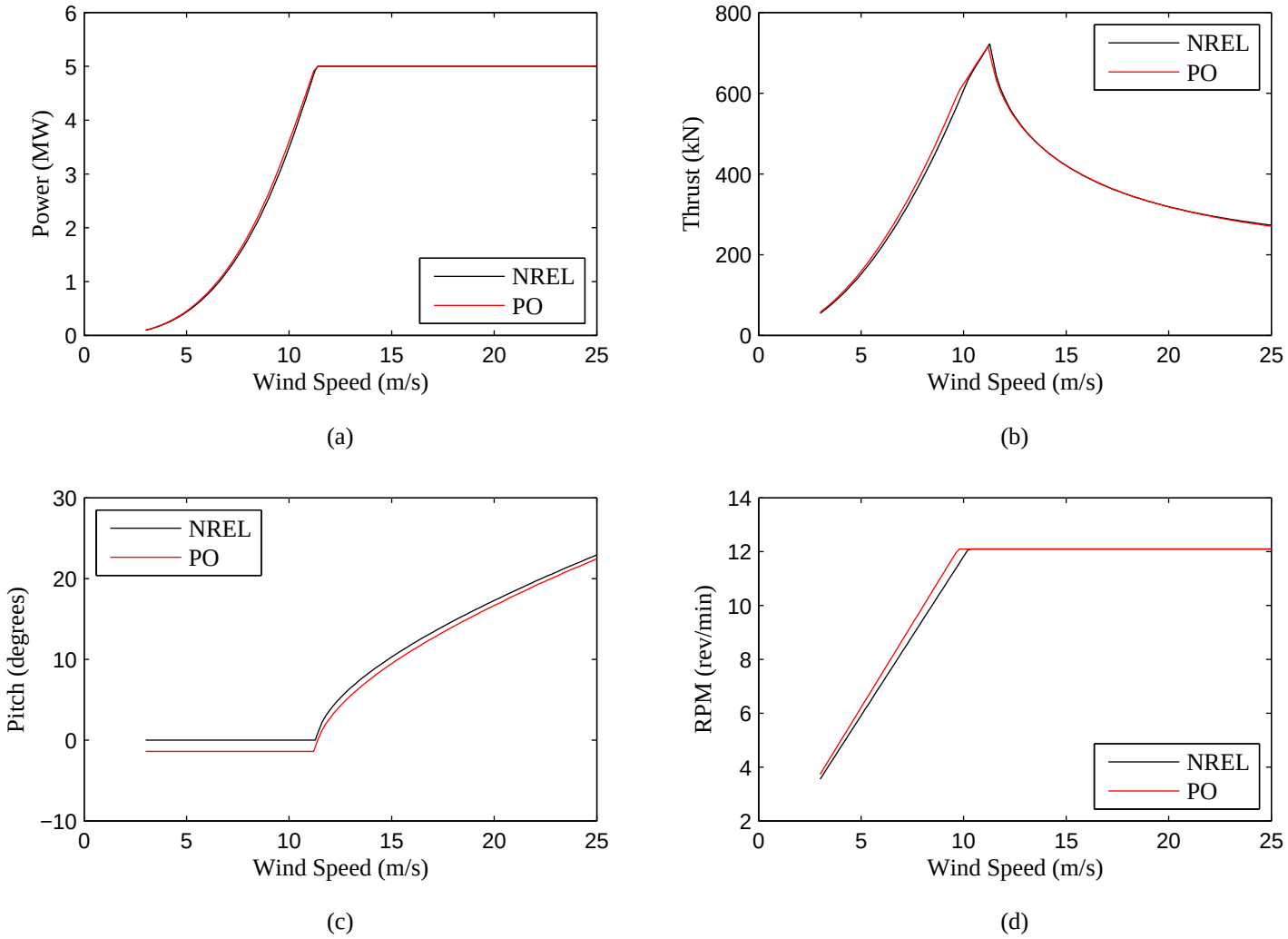

Figure 6.8: Power (a) and thrust (b) curves, and pitch (c) and RPM (d) schedules for the NREL 5 MW blade and a Pareto-optimal (PO) solution.

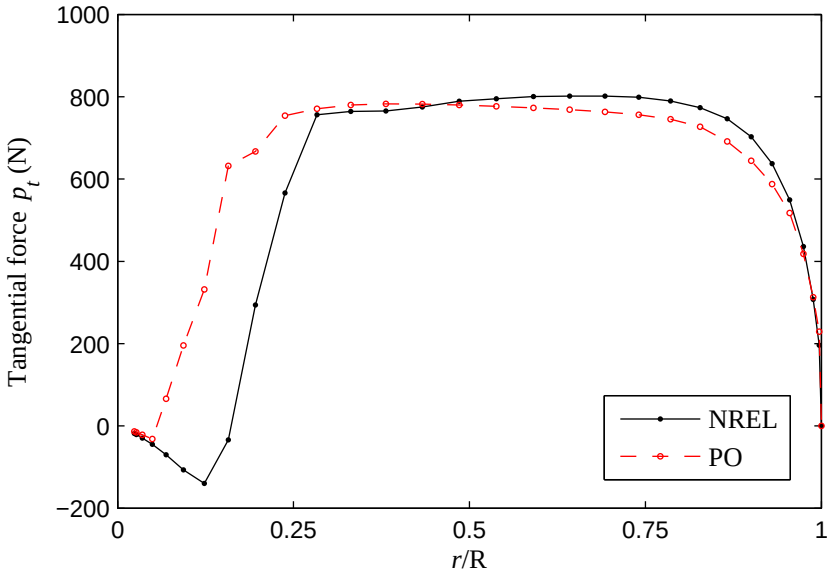

Figure 6.9: Blade element tangential aerodynamic force p_t, at the wind speed where $M_{flap,root}$ is a maximum for the NREL 5 MW blade and a Pareto-optimal (PO) solution.

To further understand why PO is superior to the NREL 5 MW blade, the tangential and normal aerodynamic forces versus r/R at peak $M_{flap,root}$ are plotted in Figures 6.9 and 6.10 respectively. Observing Figure 6.9, the increase in power is credited to the rise in p_t towards the root of the blade, since $dP = \omega dQ$ and $dQ = rBp_t dr$ (equations (3.27) and (3.18)). The rise in p_t is the result of the increase in lift, achieved by replacing the cylindrical ($t/c = 1.0$) portion of the NREL 5 MW blade with an airfoil shape ($t/c \approx 0.4$), and increasing the twist and chord (see Figure 6.5(a)–(c)). With the increase in lift involves higher p_n as shown in Figure 6.10. Although an adverse effect, this has minimal impact on $M_{flap,root}$ because $M_{flap,root} = \int_{r_{hub}}^{R} r p_n(r)\, dr$ and r is small near the root. Examining Figure 6.10, the decrease in $M_{flap,root}$ is driven by the reduction in p_n towards the tip of the blade (where r is large), achieved by using thicker airfoils and decreasing the chord (see Figure 6.5(b)–(c)). Reducing p_n however, consequently lowers p_t and also the power. The loss in power at $r/R > 0.5$ for this particular blade is compensated by the increase in power from altering the blade at $r/R < 0.5$. At the variable-speed region, the differential power coefficient dC_P for PO is much larger than the NREL 5 MW blade near the root, as shown in Figure 6.11.

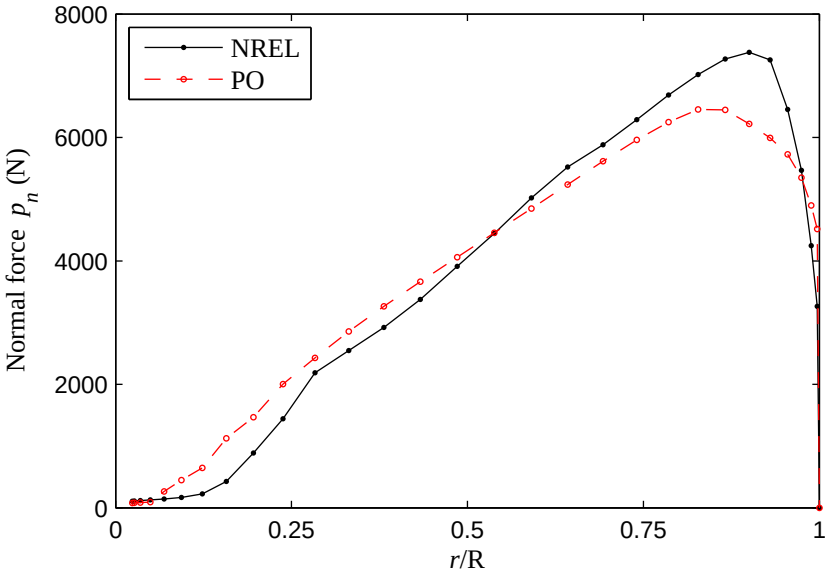

Figure 6.10: Blade element normal aerodynamic force p_n, at the wind speed where $M_{flap,root}$ is a maximum for the NREL 5 MW blade and a Pareto-optimal (PO) solution.

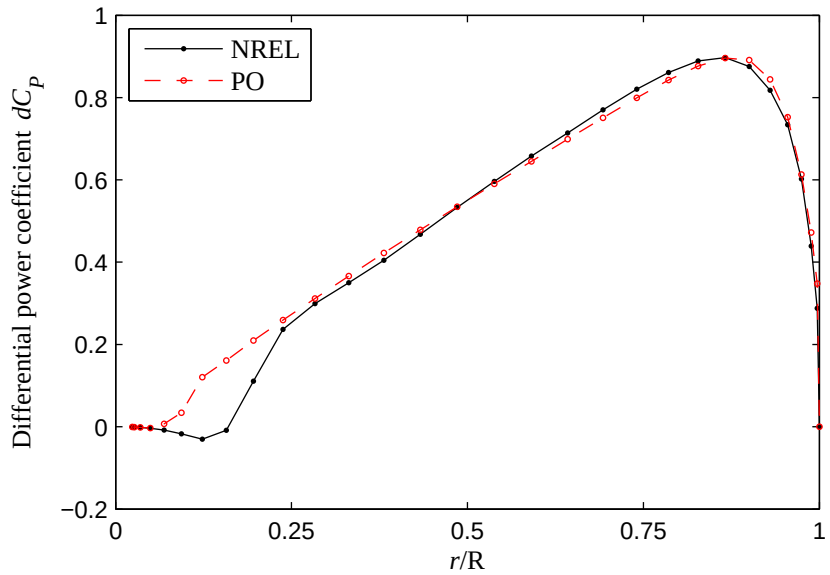

Figure 6.11: Differential power coefficient dC_P, for the NREL 5 MW blade and a Pareto-optimal (PO) solution at the variable-speed region.

Figure 6.12 compares the structural properties between the NREL 5 MW blade and PO. In Figure 6.12(a), there is an increase in spar-cap thickness (SCT) both at the root and tip. The increase in SCT at the root is the result of replacing the stiffer cylindrical part of the blade with an airfoil that is less stiff in EI_1. This is shown in Figure 6.12(b) where despite the increase in SCT, $EI_{1,\mathrm{NREL}}$ is still much larger than $EI_{1,\mathrm{PO}}$ at $r/R < 0.25$. Because of the loss in stiffness in $EI_{1,\mathrm{PO}}$, the flapwise deflection δ_{flap}, for PO becomes larger between $r/R = 0$ and $r/R = 0.75$ as shown in Figure 6.12(d). To satisfy the tip deflection constraint, SCT is added towards the tip region, specifically between $r/R = 0.75$ and $r/R = 1$. Consequently, δ_{flap} begins to converge towards the deflection profile of the NREL 5 MW blade at $r/R = 0.75$. Since EI_2 is well correlated with chord, the increase in chord at $r/R < 0.5$ yielded an increase in EI_2 as well. Figure 6.12(c) displays the bending moments about the principal axes for the NREL 5 MW blade and PO. The reduction in $M_{flap,root}$ for PO is clearly illustrated by the lower $M_{1,\mathrm{PO}}$ distribution compared to $M_{1,\mathrm{NREL}}$. The increase in $M_{2,\mathrm{PO}}$ at $r/R < 0.25$ is because of the higher p_t generated by the airfoil in comparison to the cylinder.

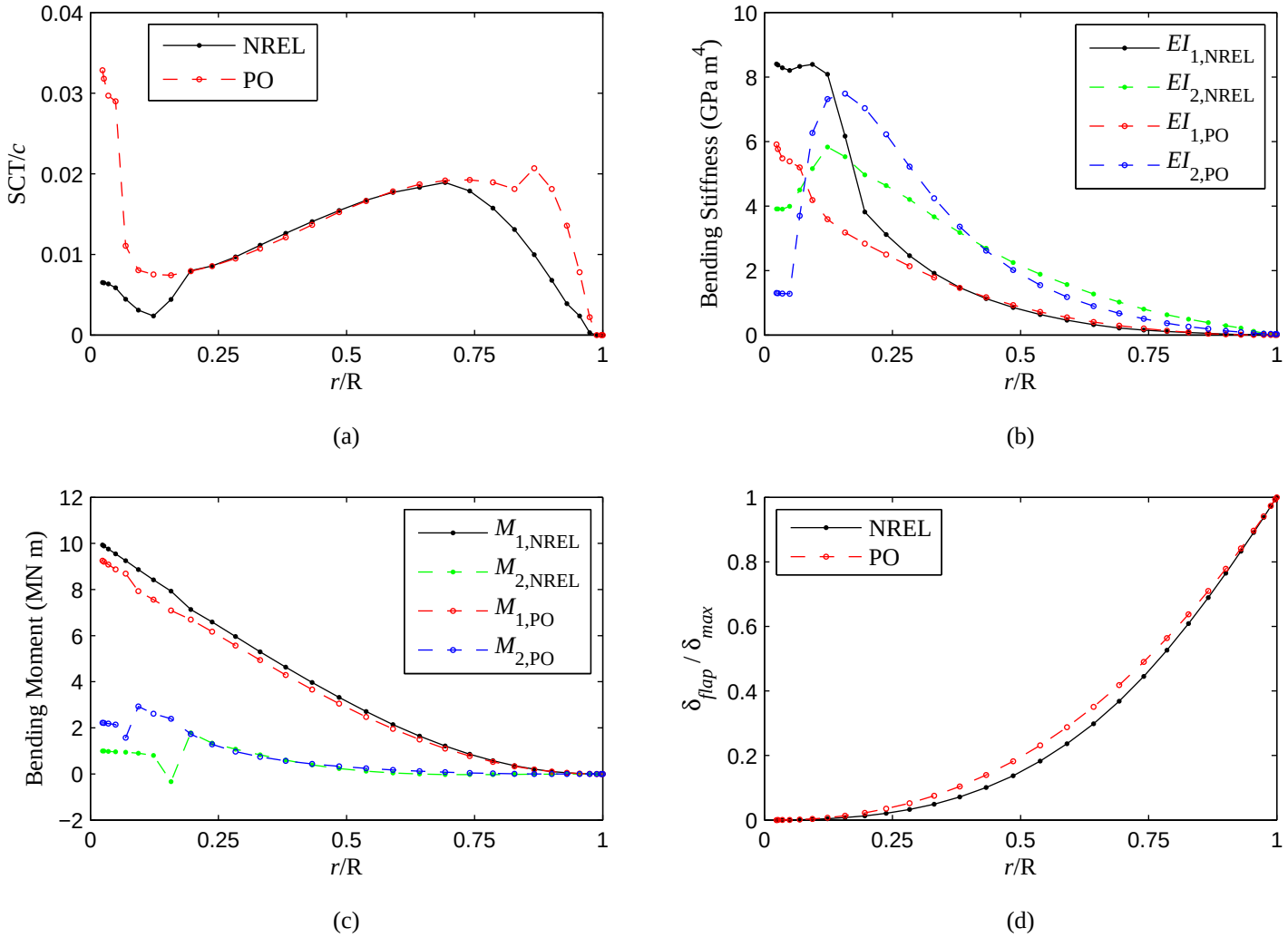

Figure 6.12: Blade element spar-cap thickness (SCT) (a), bending stiffness (b), bending moment (c), and flapwise deflection (d) distributions for the NREL 5 MW blade and a Pareto-optimal (PO) solution.

Having computed a well-defined Pareto-optimal set that approximates PF_{true}, it is now possible to apply the algorithms and measure their convergence. Table 6.3 summarizes the parameter settings used for three algorithms, which are based on the studies performed on the ZDT and DTLZ test functions. As shown on the last row of Table 6.3, the wind-turbine blade optimization problem differs from the DTLZ2 test case in the addition of constraint handling. The three algorithms used are the hybrid and non-hybrid NSGA-II, and *gamultiobj*. Figure 6.13 displays the GD results for the three algorithms. Due to the high computational cost involved in the wind-turbine blade optimization, each algorithm is executed once only (as opposed to 10 runs for DTLZ2) for calculating the mean GD. Consequently, the GD results in Figure 6.13 may be subjected to uncertainties for the same reason as described in section 5.9. Furthermore, the max-min interval cannot be estimated. Note that the max-min interval from a test function study (e.g DTLZ2 in section 5.9) cannot be transferred onto the wind-turbine blade optimization problem, since the nature of the objective functions (or objective spaces) between the two problems are fundamentally different. Additional uncertainty in the GD calculation will also be introduced because of the approximation of PF_{true}. The effect of the approximation is demonstrated by the slightly scattered Pareto-optimal solutions in Figures 6.3 and 6.4.

As shown in Figure 6.13, the hybrid fails to provide the significant reduction in objective-function evaluations anticipated from the ZDT and DTLZ test-function studies. For the first 6000 objective-function evaluations, the NSGA-II results in the best convergence while the hybrid and *gamultiobj* perform less efficiently. The effect of the penalty constraint-handling approach in *gamultiobj* is seen by the GD values that exceeds the upper limit of the y-axis on the plot. As discussed in section 5.4, this occurs because the objective vector is set to the worst possible values for unfeasible blade designs, which are abundant during the early stages of the optimization. After 1200 objective-function evaluations, the convergence for *gamultiobj* almost matches that of the other two algorithms.

Table 6.3: Summary of algorithms and parameter settings for the three-objective NREL 5 MW blade optimization. Retrieved from [3].

	hybrid NSGA-II	NSGA-II	*gamultiobj*
Population size	200	200	200
Selection	binary tournament	binary tournament	binary tournament
Crossover	scattered	scattered	scattered
Crossover fraction	0.9	0.9	0.9
Mutation	polynomial	polynomial	adaptive feasible
Mutation probability	1/21[a]	1/21[a]	–
Mutation index	20	20	–
Pareto fraction	1	1	1
Spread maintenance	clustering approach	clustering approach	crowding routine
Constraint handling	selection based	selection based	penalty based

[a]A commonly used heuristic $(1/n)$ [57].

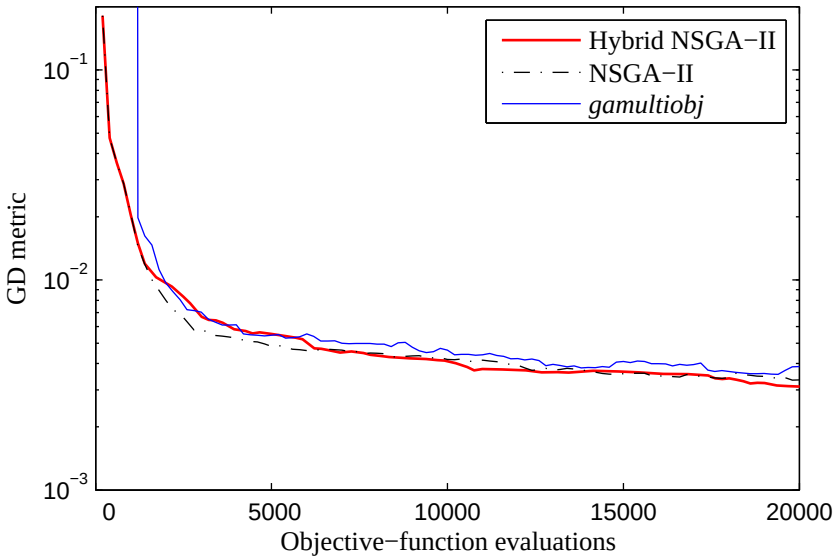

Figure 6.13: Algorithm convergence for the three-objective NREL 5 MW blade optimization. Retrieved from [3].

There are a few potential factors that might explain the hampered performance of the hybrid NSGA-II on the wind-turbine blade optimization problem. The most significant and likely one is due to the substantial increase in complexity of the objective functions in comparison to the simple analytical ZDT and DTLZ test cases. Like all other gradient-based methods, *fminimax* requires that the objective and constraint functions are continuous and are sensitive to small changes to the decision vector. If the objective functions are calculated from numerical models involving discretizations and interpolations such as BEM and the structural model used here, then a distorted gradient and alteration to the decision vector results. For illustration, the values of the ASF from a local search performed on an individual from the DTLZ2 and wind-turbine blade optimization problems are shown in Figure 6.14. When the value of the ASF decreases monotonically as the number of objective-function evaluations increases, then the objective vector of the individual chosen for local search is being minimized (or improved) as expected by the dominant first term in equation (5.3). This is shown clearly for the DTLZ2 on the left of Figure 6.14 but is not the case for the wind-turbine blade optimization. The magnified view on the right of Figure 6.14 displays noisy behaviour that is representative of the nature of the objective functions. The term *noisy* used here is not associated to the random process of a physical nature (such as turbulence) but the systematic numerical noise inherent to the non-smoothness of the objective functions. This noise prevents the gradient-based local search in minimizing the objective vector and hence the value of the ASF barely deviates from zero.

There are a few potential solutions to the improvement of the gradient-based local search in the hybrid NSGA-II for the presented three-objective optimization of wind-turbine blades. The first is to reduce the discretization by decreasing the number of blade elements or CPs. This will allow perturbations in the decision vector to have a more significant impact on the objective vector, which a gradient-based solver can detect more easily. This has been verified in the early stages of an optimization executed soon after using 10 blade elements,

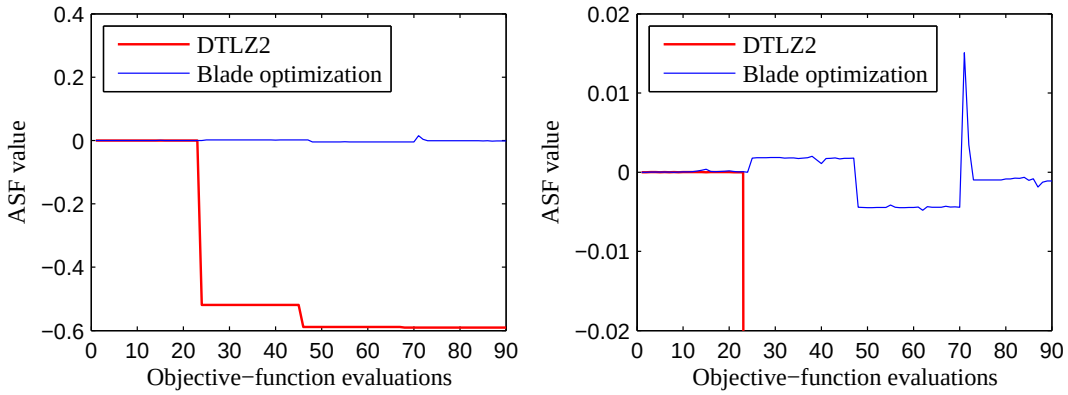

Figure 6.14: Value of the achievement scalarizing function (ASF) for DTLZ2 and blade optimization problems. Regular y-axis scale (left) and magnified (right). Retrieved from [3].

but was never completed. Secondly, increasing the gradient's step-size while still capturing the derivatives of the objective functions may also give a similar effect. Besides the discretization, the interpolation of the lift and drag coefficients as well as the airfoil-profile coordinates from the master-airfoil data (see section 6.1) may also introduce noise in the objective functions. To mitigate this potential source of noise, the master-airfoil data must be sufficiently refined. Finally, replacing the objective functions with analytical expressions (similar to DTLZ2) whenever possible will ensure accurate gradient calculations. For example, the blade cross-sectional shape can be approximated by the analytical double-ellipse model (see section 4.2.5). The double ellipse does not require interpolations or numerical integration, hence will be sensitive to changes in the decision vector and provide exact values for m_{blade}, δ_{flap}, and ε. Although better for gradient calculations, the double ellipse is not a realistic model of a wind-turbine blade. For a detailed discussion on gradient-quality analysis see [100]. As an alternative to gradient-based local search, non-gradient based approaches should also be attempted since they are more robust in noisy environments. Direct-search methods such as pattern search [101] and the complex method (section 2.5.2) are the ideal candidates.

Chapter 7

CONCLUSIONS

7.1 Conclusions

The purpose of this thesis was to develop an efficient multi-dimensional optimization framework for the preliminary design of large wind-turbine blades. The framework combines objective functions for aerodynamic performance as energy output, and structural performance as root-bending moment and blade mass. The optimization is performed by maximizing or minimizing the objective-function values while also satisfying constraints. Constraints include strain, blade tip deflection, and restrictions in the blade shape. An efficient optimization algorithm is developed into the framework that searches for the optimum blade designs. Since basic data for commercially-produced large blades is not available, the optimization was focussed on the National Renewable Energy Laboratory's (NREL) 5 MW blade designed for offshore applications. The codes implementing each objective function were developed and extensively tested against appropriate benchmarks to give confidence in the accuracy of the final optimization.

For many years, gradient and non-gradient based methods were implemented by researchers in optimizing wind-turbine blades. Following an extensive literature review, the author believes that an optimization algorithm based on a hybrid multi-objective evolutionary algorithm (MOEA) has never been applied for wind-turbine blade optimization. Furthermore, all multi-objective optimization studies on large-scale wind-turbine blades have been restricted to a bi-objective problem resulting in a two-dimensional trade-off curve. Hybrid MOEAs are known to have superior convergence properties than conventional MOEAs, requiring fewer objective-function evaluations to attain the optimum solutions. In the current study, the execution of all codes implementing each objective function requires a consider-

able amount of computing time and consequently, it is critical to reduce the total number of objective-function evaluations as much as possible. The overall efficiency of the optimization framework therefore depends strongly on the optimization algorithm implemented. For these reasons, the project was focussed in developing and applying a hybrid MOEA for a three-objective wind-turbine blade optimization problem where a three-dimensional trade-off surface is the end result.

Among the several hybrid MOEAs available, the one developed is based on the concurrent-hybrid non-dominated sorting genetic algorithm II (hybrid NSGA-II), and is comprised of a hybridized gradient and non-gradient based MOEA. The hybrid NSGA-II has been developed and applied for the simultaneous optimization of three objective functions: 1) annual energy production (AEP), 2) flapwise root-bending moment $M_{flap,root}$, and 3) mass m_{blade}, of the NREL 5 MW wind-turbine blade. The codes implementing each objective function consist of blade element momentum (BEM) and beam models, which were validated by comparing their outputs with those from the National Wind Technology Center's WT_Perf and PreComp codes, the NREL Unsteady Aerodynamics Experiment Phase VI measurements, analytical cases, and results from the literature.

In the hybrid NSGA-II, the non-gradient based component is a MOEA, whereas the gradient component involves solving a differentiable version of the achievement scalarizing function (ASF). The MOEA is the NSGA-II, and the sequential programming method is used to solve the ASF. To compare the rate of convergence between the hybrid and non-hybrid NSGA-II, the generational distance (GD) metric is used. The GD metric requires prior knowledge of the true Pareto front PF_{true}, which is unknown for the blade optimization. Hence, a computationally intensive case requiring 110,000 objective-function evaluations using the non-hybrid NSGA-II was performed to approximate PF_{true}.

From this approximation, a 1.8% increase in AEP and 4.7% decrease in $M_{flap,root}$ with the same m_{blade} as the NREL 5 MW blade was achieved. Comparing the optimized blade with

the original NREL 5 MW reveals an increase in twist and chord near the root, but a decrease in chord between the mid-span and blade tip. A decrease in thickness at the root is also observed. Although these design trends yield improved performance, they should be used with caution. Assumptions were made to simplify the aerodynamic and structural models (see Appendix A or sections 3.1–3.3.2, 4.1–4.2.1, and 4.3–4.4), suggesting that the results are only as accurate as the models themselves. Therefore, further and more accurate modelling is important for finalizing the design. Computational fluid dynamics (CFD) and finite element software, as well as scaled model testing could be used to validate the blade performance. Despite the promising results obtained for the hybrid NSGA-II on analytical test functions, no significant improvement in convergence was observed for the three-objective wind-turbine blade optimization problem. The numerical noise inherent to BEM and the structural model prevent a suitable gradient from being calculated.

7.2 Recommendations

Although the optimization framework developed has successfully improved the NREL 5 MW blade design, its efficiency has not reached its full potential. The author recommends the following steps (in order of decreasing importance – 1. being the most important) to reduce the numerical noise and hence improve the gradient-based local search:

1. Reduce the number of blade elements or control points. This will allow perturbations in the decision vector to have a more significant impact on the objective vector, which a gradient-based solver can detect more easily. Using 10 blade elements, the author observed an improvement in the ASF value during the early stages of a separate optimization run. This optimization run was never completed and an in-depth analysis on convergence was not performed. Conversely, by reducing the number of blade elements, the accuracy of the span-wise distributions (aerodynamic loads, structural properties, etc.) will

also be reduced. Determining the best compromise between the number of blade elements used (modelling accuracy) and the performance of the gradient calculations (computational cost) may be necessary.

2. Adjust the gradient step-size while still capturing the derivatives of the objective functions. If the noise is trivial in comparison to the gradient step-size, then an improvement in the ASF value should be attained. The author has made several attempts but did not manage to achieve any improvements.

3. Increase the resolution of the master-airfoil data. If the lift and drag coefficients and airfoil-profile coordinates are coarse, then numerical instabilities will arise when they are interpolated. The lift and drag data used consisted of approximately 142 points, while airfoil-profile coordinates consisted of approximately 400. The author has revised the master-airfoil data and recommends further refinement only if a sufficient improvement in the ASF value has not been achieved after completing steps 1 and 2 above.

4. Replace the objective functions with analytical expressions. Objective functions that consist of analytical equations rather than numerical approximations will ensure accurate gradient calculations. For example, the cross-sectional properties of the wind-turbine blade can be estimated using an elliptical model, which has a readily available analytical solution. Analytical equations do not exhibit any noise, but generally involve assumptions, limitations and decreased accuracies in modelling.

As an alternative to the recommendations provided above, a non-gradient based approach for local search should also be attempted since they are less influenced by noisy objective functions. Direct-search methods such as pattern search and the complex method are the ideal candidates.

7.3 Future Work

In addition to the continued investigation of hybrid MOEAs for the benefit of convergence, other capabilities of the optimization framework may be improved with further research. For example, additional objective functions, variables, and constraints may be included. An objective function together with the maximization of AEP, and minimization of $M_{flap,root}$ and m_{blade} could be noise minimization, resulting in a four-dimensional optimization problem. An effective treatment of four objective functions will likely require adjustments to the NSGA-II or a different method of optimization. It has been reported in the literature that the performance of MOEAs based on the non-dominance concept, such as the NSGA-II, deteriorates rapidly with increasing number of objective functions [102]. Wagner, Beume, and Naujoks [103] show that indicator-based MOEAs such as the $\mathcal{S}$ metric selection evolutionary multi-objective algorithm (SMS-EMOA) [104] perform very well in problems with more than three objective functions. Additional variables may include control points that determine the airfoil shape of each blade element in the aerodynamic model, and the chord-wise position of the shear webs and spar caps of each blade element in the structural. To compute the lift and drag coefficients of an arbitrary airfoil shape, simulators such as XFOIL and CFD codes can be employed.

When optimizing wind-turbine blades, minimizing the cost of energy (COE) is typically used as an objective function. This allows the cost of wind energy to be compared with the cost of other energy sources. In this thesis, it was assumed that m_{blade} was well correlated to cost. In the future, a detailed cost model including turbine components such as rotor, tower, gearbox, and generator, and other costs such as foundation and operation and maintenance, should be developed and implemented.

Lastly, higher fidelity models such as FAST (Fatigue, Aerodynamics, Structures, and Turbulence) [105] and VABS (Variational Asymptotic Beam Sectional Analysis) [106] tools could be incorporated to compute the objective functions. FAST is a comprehensive wind

turbine aero-hydro-servo-elastic tool that combines a rotor aerodynamics module (aero), a platform hydrodynamics module for offshore applications (hydro), a control system dynamics module (servo), and a structural dynamics module (elastic) to allow coupled aero-hydro-servo-elastic analysis in the time domain [107]. VABS is a finite-element based cross-sectional analysis tool capable of modelling anisotropic blades with arbitrary sectional topology and material constructions [108]. Instead of VABS, PreComp could also be used. PreComp however, possesses more limitations than VABS. Implementing FAST and VABS into the optimization framework will substantially increase the modelling accuracy, but will increase the computing time per objective-function evaluation. FAST and VABS may also introduce additional difficulties when evaluating the gradients for a hybrid MOEA.

Bibliography

[1] Hand MM, Simms DA, Fingersh LJ, Jager DW, Cotrell JR, Schreck S, Larwood SM. Unsteady aerodynamics experiment phase VI: Wind tunnel test configurations and available data campaigns. *Technical Report NREL/TP-500-29955*, National Renewable Energy Laboratory, Golden, CO December 2001.

[2] Griffin DA. WindPACT turbine design scaling studies technical area 1–composite blades for 80- to 120-meter rotor; March 21, 2000 - March 15, 2001. *Technical Report NREL/SR-500-29492*, National Renewable Energy Laboratory, Golden, CO March 2001.

[3] Sessarego M, Dixon KR, Rival DE, Wood DH. A hybrid multi-objective evolutionary algorithm for wind-turbine blade optimization. *Wind Energy* 2013; (under review).

[4] Jonkman J, Butterfield S, Musial W, Scott G. Definition of a 5-MW reference wind turbine for offshore system development. *Technical Report NREL/TP-500-38060*, National Renewable Energy Laboratory, Golden, CO February 2009.

[5] Global Wind Energy Council. Global wind report: Annual market update 2011. URL `http://gwec.net/wp-content/uploads/2012/06/Annual_report_2011_lowres.pdf`, accessed Nov. 1, 2012.

[6] Burton T, Sharpe D, Jenkins N, Bossanyi E. *Wind Energy Handbook*. John Wiley & Sons, Ltd, 2002.

[7] European Wind Energy Association. *Upwind: Design limits and solutions for very large wind turbines.* March 2011.

[8] Hansen MOL. *Aerodynamics of Wind Turbines*. 2 edn., Earthscan: London, 2008.

[9] Blind Comparison Participants. *Participant's Documentation* 2000. URL `http://wind.nrel.gov/amestest/DocumentationSummary.pdf`, accessed Oct. 10, 2011.

[10] Buhl ML. A new empirical relationship between thrust coefficient and induction factor for the turbulent windmill state. *Technical Report NREL/TP-500-36834*, National Renewable Energy Laboratory, Golden, CO August 2005.

[11] Simms D, Schreck S, Hand M, Fingersh LJ. NREL unsteady aerodynamics experiment in the NASA-Ames wind tunnel: A comparison of predictions to measurements. *Technical Report NREL/TP-500-29494*, National Renewable Energy Laboratory, Golden, CO June 2001.

[12] Thiele L, Miettinen K, Korhonen PJ, Molina J. A preference-based evolutionary algorithm for multi-objective optimization. *Evolutionary Computation* Sep 2009; **17**(3):411–436, doi:10.1162/evco.2009.17.3.411. URL `http://dx.doi.org/10.1162/evco.2009.17.3.411`.

[13] Deb K. *Multi-Objective Optimization using Evolutionary Algorithms*. Wiley: Chichester, 2001.

[14] Deb K, Pratap A, Agarwal S, Meyarivan T. A fast and elitist multiobjective genetic algorithm: NSGA-II. *IEEE Transactions on Evolutionary Computation* Apr 2002; **6**(2):182 –197, doi:10.1109/4235.996017. URL `http://dx.doi.org/10.1109/4235.996017`.

[15] Timmer N. DOWEC-NREL 5MW blade airfoil data. March 2011. URL `https://wind.nrel.gov/forum/wind/viewtopic.php?f=2&t=440`, accessed April 29, 2013.

[16] Global Wind Energy Council. Wind and climate change. URL `http://gwec.net/wp-content/uploads/2012/06/Wind-climate-fact-sheet-low-res.pdf`, accessed Nov. 1, 2012.

[17] Okulov VL, van Kuik GA. The Betz–Joukowsky limit: on the contribution to rotor aerodynamics by the British, German and Russian scientific schools. *Wind Energy* 2012; **15**(2):335–344, doi:10.1002/we.464. URL `http://dx.doi.org/10.1002/we.464`.

[18] Boyle G. *Renewable Energy: Power for a Sustainable Future*. 2 edn., Oxford University Press, 2004.

[19] Wilson RE, Lissaman PBS. *Applied aerodynamics of wind power machines*. Dept. Mechanical Engineering, Oregon State University: Corvallis, 1974.

[20] Luke S. *Essentials of Metaheuristics*. Lulu, 2009. URL `http://cs.gmu.edu/$\sim$sean/book/metaheuristics/`, accessed Nov. 4, 2012.

[21] Fuglsang PL, Madsen HA. *A design study of a 1 MW stall regulated rotor*. Risø-R-799(EN), Risø National Laboratory: Roskilde, Denmark, 1995.

[22] Fuglsang P, Bak C, Schepers JG, Bulder B, Cockerill TT, Claiden P, Olesen A, van Rossen R. Site-specific design optimization of wind turbines. *Wind Energy* 2002; **5**(4):261–279, doi:10.1002/we.61. URL `http://dx.doi.org/10.1002/we.61`.

[23] Lee KH, Kim KH, Lee DH, Lee KT, Park JP. Two-step optimization for wind turbine blade with probability approach. *Journal of Solar Energy Engineering* 2010; **132**(3):034503, doi:10.1115/1.4001671. URL `http://link.aip.org/link/?SLE/132/034503/1`.

[24] Kenway G, Martins J. Aerostructural shape optimization of wind turbine blades considering site-specific winds. *Multidisciplinary Analysis Optimization Conferences*. American Institute of Aeronautics and Astronautics, 2008, doi:10.2514/6.2008-6025. URL `http://dx.doi.org/10.2514/6.2008-6025`.

[25] Drela M. XFOIL: An analysis and design system for low Reynolds number airfoils. *Conference on Low Reynolds Number Airfoil Aerodynamics*, University of Notre Dame, 1989.

[26] Xudong W, Shen WZ, Zhu WJ, Sørensen JN, Jin C. Shape optimization of wind turbine blades. *Wind Energy* 2009; **12**(8):781–803, doi:10.1002/we.335. URL `http://dx.doi.org/10.1002/we.335`.

[27] The MathWorks, Inc. URL `http://www.mathworks.com`, accessed Nov. 16, 2012.

[28] Bottasso C, Campagnolo F, Croce A. Multi-disciplinary constrained optimization of wind turbines. *Multibody System Dynamics* 2012; **27**:21–53, doi:10.1007/s11044-011-9271-x. URL `http://dx.doi.org/10.1007/s11044-011-9271-x`.

[29] Goldberg DE. *Genetic Algorithms in Search, Optimization and Machine Learning*. Addison-Wesley: Reading, 1989.

[30] Selig MS, Coverstone-Carroll VL. Application of a genetic algorithm to wind turbine design. *Journal of Energy Resources Technology* 1996; **118**(1):22–28, doi:10.1115/1.2792688. URL `http://link.aip.org/link/?JRG/118/22/1`.

[31] Selig MS, Tangler JL. Development and application of a multipoint inverse design method for horizontal axis wind turbines. *Wind Engineering* 1995; **19**(2):91–105.

[32] Wilson RE, Walker SN. *A Fortran Program for the Determination of Performance, Load and Stability Derivatives of Wind Mills*. Dept. of Mechanical Engineering, Oregon State University: Corvallis, 1974.

[33] Deb K. An efficient constraint handling method for genetic algorithms. *Computer Methods in Applied Mechanics and Engineering* 2000; **186**(2–4):311–338, doi:10.1016/S0045-7825(99)00389-8. URL `http://www.sciencedirect.com/science/article/pii/S0045782599003898`.

[34] Giguere P, Selig MS. Blade geometry optimization for the design of wind turbine rotors. *Proceedings of AIAA/ASME Wind Energy Symposium. Reno, Nevada*, 2000.

[35] Srinivas N, Deb K. Muiltiobjective optimization using nondominated sorting in genetic algorithms. *Evolutionary Computation* Sep 1994; **2**(3):221–248, doi:10.1162/evco.1994.2.3.221. URL `http://dx.doi.org/10.1162/evco.1994.2.3.221`.

[36] Deb K, Agrawal RB. Simulated binary crossover for continuous search space. *Complex Systems* 1995; **9**(2):115–148.

[37] Deb K, Goyal M. A combined genetic adaptive search (GeneAS) for engineering design. *Computer Science and Informatics* 1996; **26**(4):30–45.

[38] Wang L, Wang Tg, Luo Y. Improved non-dominated sorting genetic algorithm (NSGA)-II in multi-objective optimization studies of wind turbine blades. *Applied Mathematics and Mechanics* 2011; **32**:739–748, doi:10.1007/s10483-011-1453-x. URL `http://dx.doi.org/10.1007/s10483-011-1453-x`.

[39] Deb K, Goel T. Controlled elitist non-dominated sorting genetic algorithms for better convergence. *Evolutionary Multi-Criterion Optimization*, *Lecture Notes in Computer Science*, vol. 1993, Zitzler E, Thiele L, Deb K, Coello Coello CA, Corne D (eds.). Springer Berlin Heidelberg, 2001; 67–81, doi:10.1007/3-540-44719-9_5. URL http://dx.doi.org/10.1007/3-540-44719-9_5.

[40] Luo B, Zheng J, Xie J, Wu J. Dynamic crowding distance – a new diversity maintenance strategy for MOEAs. *Fourth International Conference on Natural Computation, 2008. ICNC '08.*, vol. 1, 2008; 580 –585, doi:10.1109/ICNC.2008.532. URL http://dx.doi.org/10.1109/ICNC.2008.532.

[41] Iaccarino G, Petrone G, Witteveen J, Quagliarella D, de Nicola C, Axerio-Cilies J. Wind turbine optimization under uncertainty with high performance computing. *Fluid Dynamics and Co-located Conferences*. American Institute of Aeronautics and Astronautics, 2011, doi:10.2514/6.2011-3806. URL http://dx.doi.org/10.2514/6.2011-3806.

[42] Rechenberg I. *Evolutionsstrategie: Optimierungtechnischer Systeme nach Prinzipien der biologischen Evolution*. Fromman-Holzboog Verlag: Stuttgart, 1973.

[43] Benini E, Toffolo A. Optimal design of horizontal-axis wind turbines using blade-element theory and evolutionary computation. *Journal of Solar Energy Engineering* 2002; **124**(4):357–363, doi:10.1115/1.1510868. URL http://link.aip.org/link/?SLE/124/357/1.

[44] Storn R, Price K. Differential evolution – a simple and efficient heuristic for global optimization over continuous spaces. *Journal of Global Optimization* 1997; **11**(4):341–359, doi:10.1023/A:1008202821328. URL http://dx.doi.org/10.1023/A%3A1008202821328.

[45] Wood DH. Dual purpose design of small wind turbine blades. *Wind Engineering* Sep 2004; **28**(5):511–527. URL http://dx.doi.org/10.1260/0309524043028037.

[46] Clifton-Smith MJ. Aerodynamic noise reduction for small wind turbine rotors. *Wind Engineering* Jun 2010; **34**(4):403–420. URL http://dx.doi.org/10.1260/0309-524X.3.4.403.

[47] Leloudas G, Zhu WJ, Sørensen JN, Shen WZ, Hjort S. Prediction and reduction of noise from a 2.3 MW wind turbine. *Journal of Physics: Conference Series* 2007; **75**(1):012 083. URL http://stacks.iop.org/1742-6596/75/i=1/a=012083.

[48] Kennedy J, Eberhart R. Particle swarm optimization. *Proceedings of the IEEE International Conference on Neural Networks, 1995.*, vol. 4, 1995; 1942 –1948, doi:10.1109/ICNN.1995.488968. URL http://dx.doi.org/10.1109/ICNN.1995.488968.

[49] Shi Y, Eberhart R. A modified particle swarm optimizer. *Proceedings of the IEEE International Conference on Evolutionary Computation, 1998. IEEE World Congress on Computational Intelligence.*, 1998; 69–73, doi:10.1109/ICEC.1998.699146. URL http://dx.doi.org/10.1109/ICEC.1998.699146.

[50] Liao C, Zhao X, Xu J. Blade layers optimization of wind turbines using FAST and improved PSO algorithm. *Renewable Energy* Jun 2012; **42**:227–233, doi:10.1016/j.renene.2011.08.011. URL http://www.sciencedirect.com/science/article/pii/S096014811100454X, International Symposium on Low Carbon and Renewable Energy Technology 2010 (ISLCT 2010).

[51] Yang C, Lv X, Tong G, Song X. Aerodynamic optimization design and calculation of a 2MW horizontal axial wind turbine rotor based on blade theory and particle swarm optimization. *Power and Energy Engineering Conference (APPEEC), 2011 Asia-Pacific*, 2011; 1–4, doi:10.1109/APPEEC.2011.5748648. URL http://dx.doi.org/10.1109/APPEEC.2011.5748648.

[52] Zhiquan Y, Xiong L, Yan C. Global optimum design method and software for the rotor blades of horizontal axis wind turbines. *Wind Engineering* Jul 2002; **26**(4):257–269. URL http://dx.doi.org/10.1260/030952402321039449.

[53] Weisstein EW. Vertex. URL http://mathworld.wolfram.com/Vertex.html, from MathWorld–A Wolfram Web Resource, accessed Jan. 9, 2013.

[54] Nelder JA, Mead R. A simplex method for function minimization. *The Computer Journal* 1965; **7**(4):308–313, doi:10.1093/comjnl/7.4.308. URL http://comjnl.oxfordjournals.org/content/7/4/308.abstract.

[55] Box MJ. A new method of constrained optimization and a comparison with other methods. *The Computer Journal* 1965; **8**(1):42–52, doi:10.1093/comjnl/8.1.42. URL http://comjnl.oxfordjournals.org/content/8/1/42.abstract.

[56] Hu X, Huang Z, Wang Z. Hybridization of the multi-objective evolutionary algorithms and the gradient-based algorithms. *The 2003 Congress on Evolutionary Computation, 2003. CEC '03.*, vol. 2; 870–877, doi:10.1109/CEC.2003.1299758. URL http://dx.doi.org/10.1109/CEC.2003.1299758.

[57] Sindhya K, Deb K, Miettinen K. Improving convergence of evolutionary multi-objective optimization with local search: a concurrent-hybrid algorithm. *Natural Computing* 2011; **10**:1407–1430, doi:10.1007/s11047-011-9250-4. URL http://dx.doi.org/10.1007/s11047-011-9250-4.

[58] Rankine WJM. On the mechanical principles of the action of propellers. *Transactions of the Institution of Naval Architects of Naval Architects* 1865; **6**:13–30.

[59] Froude RE. On the part played in propulsion by differences of fluid pressure. *Transactions of the Institute of Naval Architects* 1889; **30**:390–405.

[60] Joukowsky NE. Windmill of the NEJ type. *Transactions of the Central Institute for Aero-Hydrodynamics of Moscow* 1920; Also in *Collected Papers Vol. VI. The Joukowsky Institute for Aero-Hydrodynamics, Moscow* 1937; vol. VI: 405–409.

[61] Froude W. On the elementary relation between pitch, slip and propulsive efficiency. *Transactions of the Institution of Naval Architects* 1878; **19**:47–57.

[62] Drzewiecki S. *Méthode pour la détermination des éléments mécaniques des propulseurs hélicoidaux*, vol. N° 3. 1892.

[63] Drzewiecki S. *Théorie Générale de l'Hélice: hélices aériennes et hélices marines*. Gauthier-Villars et cie.: Paris, 1920.

[64] Wilson RE, Lissaman PBS, Walker SN. *Aerodynamic Performance of Wind Turbines*. Dept. Mechanical Engineering, Oregon State University: Corvallis, 1976.

[65] Leishman J. *Principles of helicopter aerodynamics*. 2 edn., Cambridge University Press: New York, 2006.

[66] Lanchester FW. A contribution to the theory of propulsion and the screw propeller. *Transactions of the Institution of Naval Architects* 1915; **57**:98–116.

[67] Glauert H. *Airplane Propellers* in Division L of *Aerodynamic Theory*, Durand WF (ed.), vol. 4. Julius Springer: Berlin, 1935.

[68] Goldstein S. On the vortex theory of screw propellers. *Proceedings of the Royal Society of London. Series A* 1929; **123**(792):440–465, doi:10.1098/rspa.1929.0078. URL `http://rspa.royalsocietypublishing.org/content/123/792/440.short`.

[69] Shen WZ, Mikkelsen R, Sørensen JN, Bak C. Tip loss corrections for wind turbine computations. *Wind Energy* 2005; **8**(4):457–475, doi:10.1002/we.153. URL `http://dx.doi.org/10.1002/we.153`.

[70] Clifton-Smith MJ. Wind turbine blade optimisation with tip loss corrections. *Wind Engineering* Oct 2009; **33**(5):477–496. URL `http://dx.doi.org/10.1260/030952409790291226`.

[71] Lock CNH, Bateman H, Townend HCH. An extension of the vortex theory of airscrews with applications to airscrews of small pitch, including experimental results. *Aeronautical Research Committee Reports & Memoranda*. No. 1014, Her Majesty's Stationery Office: London, 1926.

[72] Bottasso CL, Croce A, Nam Y, Riboldi CED. Power curve tracking in the presence of a tip speed constraint. *Renewable Energy* 2012; **40**(1):1–12, doi:10.1016/j.renene.2011.07.045. URL `http://www.sciencedirect.com/science/article/pii/S0960148111004411`.

[73] Wagner HJ, Mathur J. *Introduction to Wind Energy Systems: Basics, Technology and Operation*. Springer, 2009.

[74] Buhl ML. NWTC design codes: WT_Perf. Last modified 06-July-2012; accessed 06-July-2012. URL `http://wind.nrel.gov/designcodes/simulators/wtperf/`.

[75] McWilliam M, Crawford C. The behavior of fixed point iteration and Newton-Raphson methods in solving the blade element momentum equations. *Wind Engineering* Feb 2011; **35**(1):17–32. URL `http://dx.doi.org/10.1260/0309-524X.35.1.17`.

[76] Chaviaropoulos PK, Hansen MOL. Investigating three-dimensional and rotational effects on wind turbine blades by means of a quasi-3D Navier-Stokes solver. *Journal of Fluids Engineering* 2000; **122**(2):330–336, doi:10.1115/1.483261. URL `http://link.aip.org/link/?JFG/122/330/1`.

[77] Breton SP, Coton FN, Moe G. A study on rotational effects and different stall delay models using a prescribed wake vortex scheme and NREL phase VI experiment data. *Wind Energy* 2008; **11**(5):459–482, doi:10.1002/we.269. URL `http://dx.doi.org/10.1002/we.269`.

[78] Bauchau OA, Craig JI. *Structural Analysis: With Applications to Aerospace Structures*. Springer, 2009.

[79] National Wind Technology Center. Up to Wind Speed. December 2010. URL `http://www.nrel.gov/wind/pdfs/up_to_wind_speed_2010-12.pdf`, accessed Feb. 8, 2013.

[80] TPI Composites Inc. Parametric study for large wind turbine blades: WindPACT blade system design studies. *Technical Report SAND2002-2519*, Sandia National Laboratories, Albuquerque, NM August 2002.

[81] Ashuri T, van Bussel GJW, Zaayer MB, van Kuik GAM. An analytical model to extract wind turbine blade structural properties for optimization and up-scaling studies. *Proceedings of the 3rd EWEA Conference - Torque 2010: The Science of Making Torque from Wind*, European Wind Energy Association: Heraklion, Crete, Greece, June 28–30, 2010.

[82] Damiani R. NWTC design codes: PreComp. Last modified 19-November-2012; accessed 19-November-2012. URL `http://wind.nrel.gov/designcodes/preprocessors/precomp/`.

[83] Gunjit SB. *Users Guide to PreComp (Pre-Processor for Computing Composite Blade Properties)*. National Renewable Energy Laboratory, Golden, CO. September 2005.

[84] Merz KO. Conceptual design of a stall-regulated rotor for a deepwater offshore wind turbine. PhD Thesis, Norwegian University of Science and Technology, June 2011.

[85] Øye S. *Tjæreborg Wind Turbine (Esbjerg) Geometric and Operational Data*. VK – 184, Dept. of Fluid Mechanics, Technical University of Denmark: Lyngby, 1990. URL `http://130.226.17.201/extra/web_docs/tjare/VK-184-901130.pdf`.

[86] Øye S. *Tjæreborg Wind Turbine (Esbjerg) Structural Dynamics Data*. VK – 186, Dept. of Fluid Mechanics, Technical University of Denmark: Lyngby, 1991. URL `http://130.226.17.201/extra/web_docs/tjare/VK-186-910411.pdf`.

[87] Griffin DA. Blade system design studies volume II: Preliminary blade designs and recommended test matrix. *Technical Report SAND2004-0073*, Sandia National Laboratories, Albuquerque, NM 2004.

[88] Geoffrion AM. Proper efficiency and the theory of vector maximization. *Journal of Mathematical Analysis and Applications* 1968; **22**(3):618–630.

[89] Branke J, Deb K, Miettinen K, Slowinski R. *Multiobjective optimization: Interactive and evolutionary approaches*, *Lecture Notes in Computer Science*, vol. 5252. Springer, 2008.

[90] Miettinen K. *Nonlinear Multiobjective Optimization*. Kluwer: Boston, 1999.

[91] Wierzbicki AP. On the completeness and constructiveness of parametric characterizations to vector optimization problems. *OR Spectrum* 1986; **8**:73–87. URL `http://dx.doi.org/10.1007/BF01719738`, 10.1007/BF01719738.

[92] Zitzler E, Thiele L. Multiobjective evolutionary algorithms: A comparative case study and the strength pareto approach. *IEEE Transactions on Evolutionary Computation* Nov 1999; **3**(4):257 –271, doi:10.1109/4235.797969. URL `http://dx.doi.org/10.1109/4235.797969`.

[93] Deb K, Mohan M, Mishra S. Towards a quick computation of well-spread Pareto-optimal solutions. *Evolutionary Multi-Criterion Optimization*, *Lecture Notes in Computer Science*, vol. 2632, Fonseca C, Fleming P, Zitzler E, Thiele L, Deb K (eds.). Springer Berlin / Heidelberg, 2003; 68–68. URL `http://dx.doi.org/10.1007/3-540-36970-8_16`, 10.1007/3-540-36970-8_16.

[94] Deb K, Pratap A, Meyarivan T. Constrained test problems for multi-objective evolutionary optimization. *Evolutionary Multi-Criterion Optimization*, *Lecture Notes in Computer Science*, vol. 1993, Zitzler E, Thiele L, Deb K, Coello Coello C, Corne D (eds.). Springer Berlin Heidelberg, 2001; 284–298, doi:10.1007/3-540-44719-9_20. URL `http://dx.doi.org/10.1007/3-540-44719-9_20`.

[95] Deb K, Thiele L, Laumanns M, Zitzler E. Scalable test problems for evolutionary multiobjective optimization. *Evolutionary Multiobjective Optimization*, Abraham A, Jain L, Goldberg R (eds.). Advanced Information and Knowledge Processing, Springer London, 2005; 105–145, doi:10.1007/1-84628-137-7_6. URL `http://dx.doi.org/10.1007/1-84628-137-7_6`.

[96] Zitzler E, Deb K, Thiele L. Comparison of multiobjective evolutionary algorithms: Empirical results. *Evolutionary Computation* Jun 2000; **8**(2):173–195, doi:10.1162/106365600568202. URL `http://dx.doi.org/10.1162/106365600568202`.

[97] Van Veldhuizen D, Lamont G. On measuring multiobjective evolutionary algorithm performance. *Proceedings of the 2000 Congress on Evolutionary Computation, 2000.*, vol. 1, 2000; 204 –211, doi:10.1109/CEC.2000.870296. URL `http://dx.doi.org/10.1109/CEC.2000.870296`.

[98] Sale D. NWTC design codes: HARP_Opt. Last modified 27-July-2010; accessed 27-July-2010. URL `http://wind.nrel.gov/designcodes/simulators/HARP_Opt/`.

[99] Ceyhan Ö. Aerodynamic design and optimization of horizontal axis wind turbines by using BEM theory and genetic algorithm. Master's Thesis, Middle East Technical University, September 2008.

[100] Hjort S, Dixon K, Gineste M, Olsen A. Fast prototype blade design. *Wind Engineering* Jun 2009; **33**(4):321–333. URL http://dx.doi.org/10.1260/030952409789685726.

[101] Hooke R, Jeeves TA. "Direct search" solution of numerical and statistical problems. *J. ACM* Apr 1961; **8**(2):212–229, doi:10.1145/321062.321069. URL http://doi.acm.org/10.1145/321062.321069.

[102] Saxena DK, Ray T, Deb K, Tiwari A. Constrained many-objective optimization: A way forward. *IEEE Congress on Evolutionary Computation, 2009. CEC '09.*, May; 545–552, doi:10.1109/CEC.2009.4982993. URL http://dx.doi.org/10.1109/CEC.2009.4982993.

[103] Wagner T, Beume N, Naujoks B. Pareto-, aggregation-, and indicator-based methods in many-objective optimization. *Evolutionary Multi-Criterion Optimization*, *Lecture Notes in Computer Science*, vol. 4403, Obayashi S, Deb K, Poloni C, Hiroyasu T, Murata T (eds.). Springer Berlin Heidelberg, 2007; 742–756, doi:10.1007/978-3-540-70928-2_56. URL http://dx.doi.org/10.1007/978-3-540-70928-2_56.

[104] Beume N, Naujoks B, Emmerich M. SMS-EMOA: Multiobjective selection based on dominated hypervolume. *European Journal of Operational Research* 2007; **181**(3):1653–1669, doi:10.1016/j.ejor.2006.08.008. URL http://www.sciencedirect.com/science/article/pii/S0377221706005443.

[105] Jonkman J. NWTC design codes: FAST. Last modified 27-February-2013; accessed 23-March-2013. URL http://wind.nrel.gov/designcodes/simulators/fast/.

[106] Yu W, Hodges DH, Ho JC. Variational asymptotic beam sectional analysis – an updated version. *International Journal of Engineering Science* 2012; **59**:40–64, doi:10.1016/j.ijengsci.2012.03.006. URL http://www.sciencedirect.com/science/article/pii/S0020722512000493.

[107] Jonkman J. The new modularization framework for the FAST wind turbine CAE tool. *Aerospace Sciences Meetings*. American Institute of Aeronautics and Astronautics, 2013, doi:10.2514/6.2013-202. URL http://dx.doi.org/10.2514/6.2013-202.

[108] Chen H, Yu W, Capellaro M. A critical assessment of computer tools for calculating composite wind turbine blade properties. *Wind Energy* 2010; **13**(6):497–516, doi:10.1002/we.372. URL http://dx.doi.org/10.1002/we.372.

[109] Døssing M, Madsen HA, Bak C. Aerodynamic optimization of wind turbine rotors using a blade element momentum method with corrections for wake rotation and expansion. *Wind Energy* 2012; **15**(4):563–574, doi:10.1002/we.487. URL http://dx.doi.org/10.1002/we.487.

Appendix A

Assumptions in Aerodynamic and Structural Models

A.1 Aerodynamic Model

The aerodynamic model is based on the blade element momentum method, which includes the following assumptions:

1. Each blade element acts independently and the circular streamtubes are non-interacting;
2. The flow is steady;
3. The flow acts in the axial direction normal to the rotor plane (i.e. no yaw);
4. Reynolds numbers are sufficiently high, such that the lift and drag coefficients can be interpolated regardless of the Reynolds number;
5. Prandtl's tip-loss factor is sufficient to correct the tip-loss effects;
6. Wake rotation and wake expansion effects are negligible, although corrections are available; see Døssing, Madsen and Bak [109];
7. The effects of blade pre-bending and coning are negligible.

A.2 Structural Model

The structural model consists of a cross-sectional model and beam theory, which includes the following assumptions:

1. All materials in the cross-section behave isotropically;

2. The balsa between the shear web and panel is a continuous piece;

3. Blade deformations are sufficiently small in comparison with the blade length, such that Euler-Bernoulli assumptions apply;

4. The blade can be treated as a prismatic cantilever beam with a rectangular cross-section;

5. The effect of centrifugal stiffening is negligible;

6. Each strain component can be treated separately and the strain in the longitudinal direction is negligible;

7. Strain due to compression ($-$) and tension ($+$) can be treated identically.

Appendix B

Generational Distance for DTLZ2 Test Function

The generational distance (GD) metric is used to measure the convergence of four algorithms for the DTLZ2 test function. This section displays the set of results from 10 runs, which is separate from the one described in section 5.9, but with the same parameters as shown in Table 5.1. In Figures B.1 and B.2, the maximum, minimum, and mean values of GD are plotted for each algorithm in the DTLZ2 test function problem.

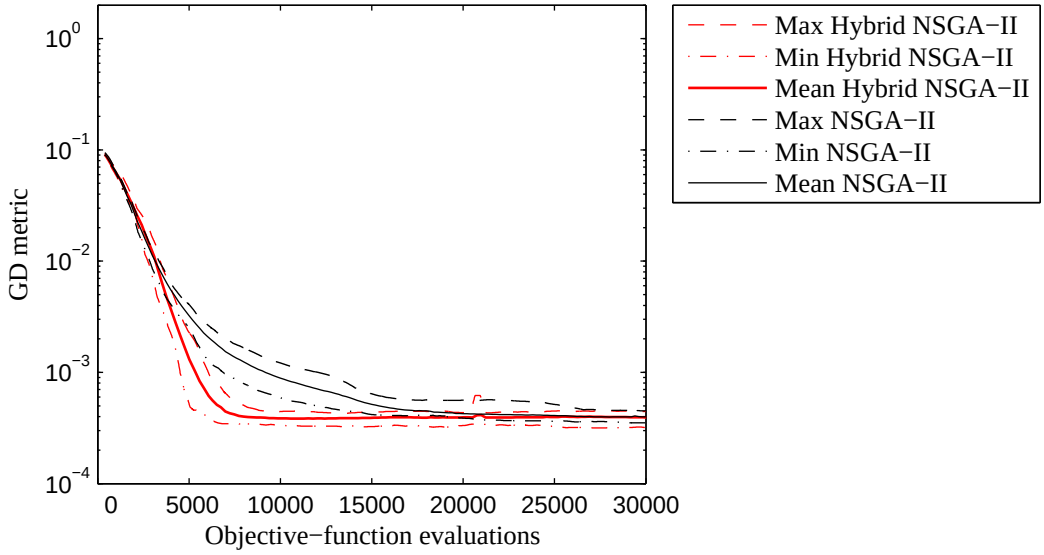

Figure B.1: Maximum, minimum, and mean GD for the three-objective DTLZ2 test function using $|PF_{true}| = 10,000$ and 10 runs for GD calculation. Hybrid NSGA-II versus NSGA-II.

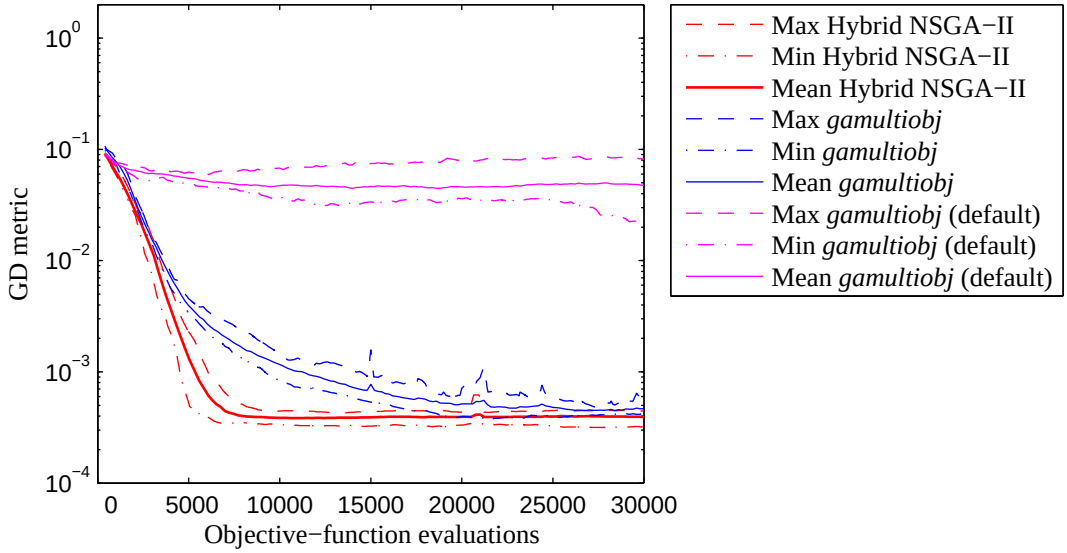

Figure B.2: Maximum, minimum, and mean GD for the three-objective DTLZ2 test function using $|PF_{true}| = 10,000$ and 10 runs for GD calculation. Hybrid NSGA-II versus *gamultiobj*.

Appendix C

NREL 5 MW Blade Master-Airfoil Data

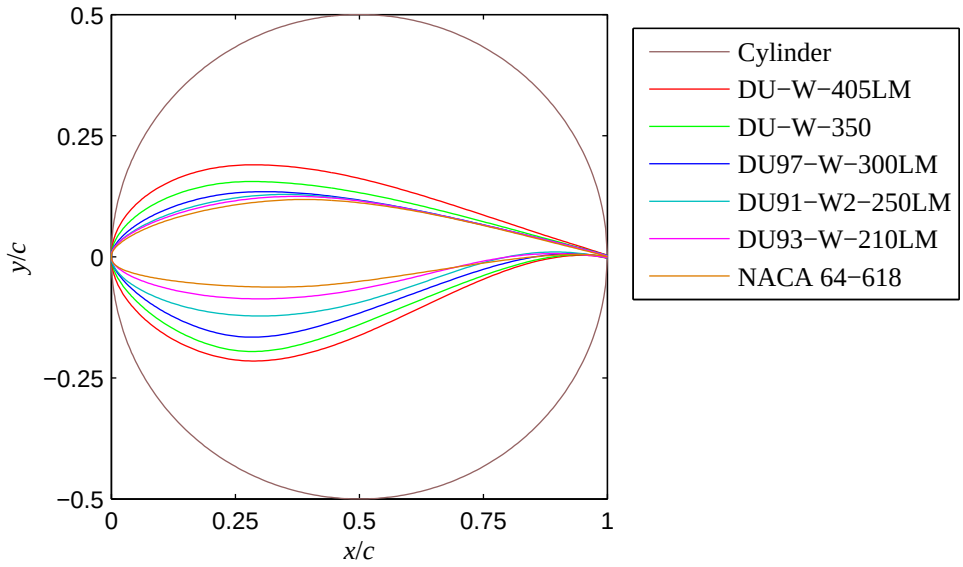

Figure C.1: NREL 5 MW airfoil profiles. Retrieved from [15].

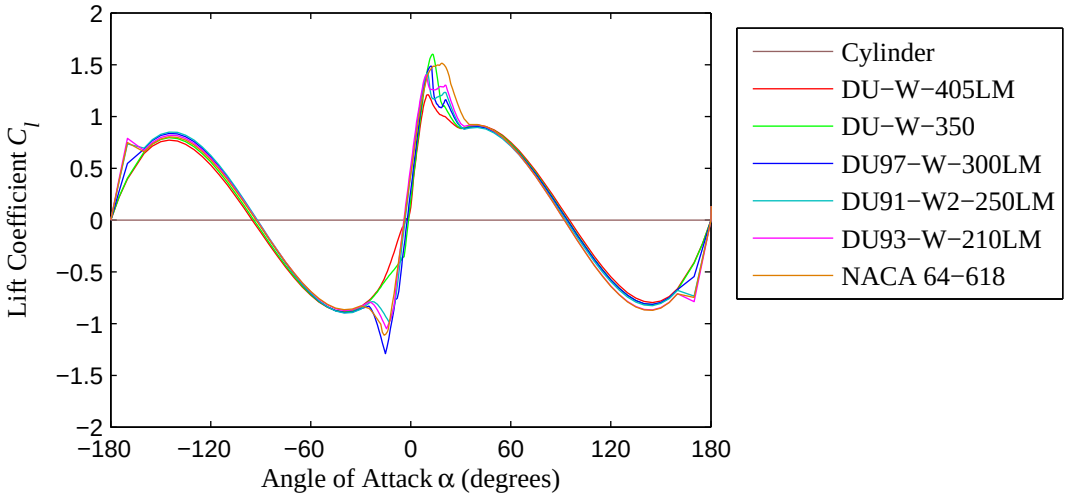

Figure C.2: NREL 5 MW airfoil lift coefficients for Reynolds number of 6-7 million. Retrieved from [15].

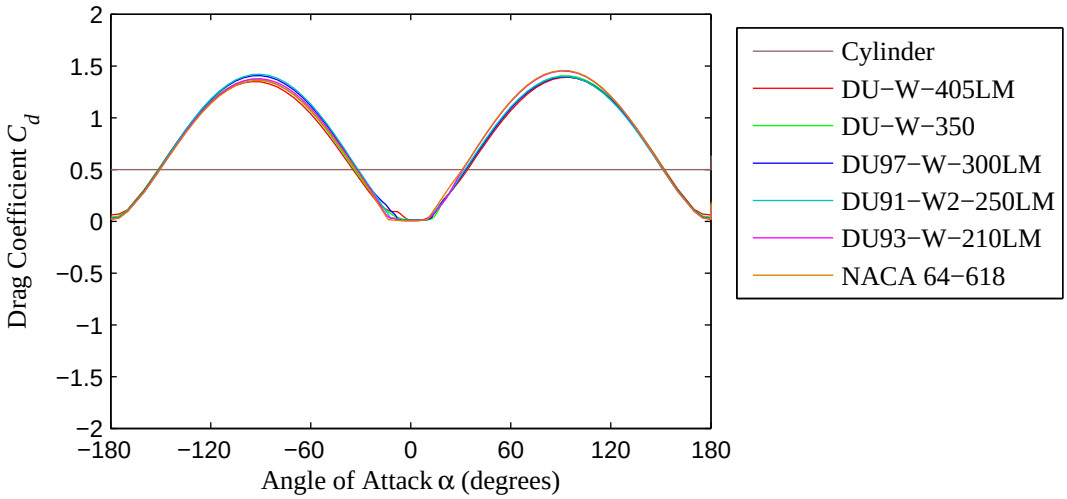

Figure C.3: NREL 5 MW airfoil drag coefficients for Reynolds number of 6-7 million. Retrieved from [15].